PolyPublie
Polytechnique Montréal

POLYTECHNIQUE MONTRÉAL
UNIVERSITÉ D'INGÉNIERIE

Titre: Title:	Intra-Operative Needle Tracking Using Optical Shape Sensing Technology
Auteur: Author:	Koushik Kanti Mandal
Date:	2016
Type:	Mémoire ou thèse / Dissertation or Thesis
Référence: Citation:	Mandal, K. K. (2016). Intra-Operative Needle Tracking Using Optical Shape Sensing Technology [Mémoire de maîtrise, École Polytechnique de Montréal]. PolyPublie. https://publications.polymtl.ca/2090/

Document en libre accès dans PolyPublie
Open Access document in PolyPublie

URL de PolyPublie: PolyPublie URL:	https://publications.polymtl.ca/2090/
Directeurs de recherche: Advisors:	Samuel Kadoury, & Sylvain Martel
Programme: Program:	Génie informatique

Ce fichier a été téléchargé à partir de PolyPublie, le dépôt institutionnel de Polytechnique Montréal
This file has been downloaded from PolyPublie, the institutional repository of Polytechnique Montréal

https://publications.polymtl.ca

UNIVERSITÉ DE MONTRÉAL

INTRA-OPERATIVE NEEDLE TRACKING USING OPTICAL SHAPE SENSING TECHNOLOGY

KOUSHIK KANTI MANDAL

DÉPARTEMENT DE GÉNIE INFORMATIQUE ET GÉNIE LOGICIEL

ÉCOLE POLYTECHNIQUE DE MONTRÉAL

MÉMOIRE PRÉSENTÉ EN VUE DE L'OBTENTION

DU DIPLÔME DE MAÎTRISE ÈS SCIENCES APPLIQUÉES

(GÉNIE INFORMATIQUE)

MARS 2016

© Koushik Kanti Mandal, 2016.

UNIVERSITÉ DE MONTRÉAL

ÉCOLE POLYTECHNIQUE DE MONTRÉAL

Ce mémoire intitulé:

INTRA-OPERATIVE NEEDLE TRACKING USING OPTICAL SHAPE SENSING TECHNOLOGY

présenté par : MANDAL Koushik Kanti
en vue de l'obtention du diplôme de : Maîtrise ès sciences appliquées
a été dûment acepté par le jury d'examen constitué de :

M. LANGLOIS J. M. Pierre, Ph. D., président

M. KADOURY Samuel, Ph. D., membre et directeur de recherche

M. MARTEL Sylvain, Ph. D., membre et codirecteur de recherche

M. LEBLOND Frédéric, Ph. D., membre

ACKNOWLEDGEMENTS

First and foremost, I would like to express my deepest appreciation to my supervisor, Professor Samuel Kadoury, for his guidance, encouragement and the pieces of advice during my graduate studies.

I would like to thank my co-supervisor Professor Sylvain Martel sincerely for giving me the opportunity to work and share the resources in his lab.

I wish to thank Professor Raman Kashyap for sharing his expertise on fiber Bragg gratins in this project.

I would like to say a big "thank-you" to all my colleagues at the “MEDICAL Lab”, “APCL Lab” and "NANOROBOTICS Lab" who shared knowledge, wisdom and joy with me. Special thanks go to François Parent for the fiber fabrication and Eric Hideki Watanabe Fernandes for helping me in taking measurements during the experiments.

I wish to thank the jury members: Professor Pierre Langlois and Professor Frédéric Leblond for their valuable time and interest in reading this thesis.

Last but not the least, I am deeply grateful to my parents, for their unconditional love and support.

RÉSUMÉ

Contexte : Les métastases hépatiques colorectales sont la principale cause de décès liée au cancer du foie dans le monde. Au cours de la dernière décennie, il a été démontré que l'ablation par radiofréquence (RFA, pour *radiofrequency ablation*) est une méthode de traitement percutané très efficace contre ce type de métastases. Cela dit, un positionnement précis de l'embout de l'aiguille utilisé en RFA est essentiel afin de se départir adéquatement de la totalité des cellules cancéreuses. Une technologie prometteuse pour obtenir la forme et la position de l'aiguille en temps réel est basée sur l'utilisation de réseaux de Bragg (FBG, pour *fiber Bragg grating*) à titre de senseur de contrainte. En effet, ce type de senseurs a une vitesse d'acquisition allant jusqu'à 20 kHz, ce qui est suffisamment rapide pour permettre des applications de guidage en temps réel.

Méthode : Les travaux présentés au sein de ce mémoire décrivent le développement d'une technologie, compatible aux systèmes d'imageries par résonance magnétique (IRM), permettant d'effectuer le suivi de la forme de l'aiguille utilisée en RFA. Premièrement, trois fibres contenant une série de réseaux de Bragg ont été collées dans une géométrie spécifique et intégrées à l'intérieur d'une aiguille 20G-150 mm. Ensuite, un algorithme de reconstruction de forme tridimensionnelle a été développé, basé sur les mesures de translation spectrales des FBGs acquises en temps réel durant le guidage de l'aiguille. La position du bout de l'aiguille ainsi que la forme tridimensionnelle complète de celle-ci ont été représentées et comparées à la position de la zone ciblée à la suite d'une simple méthode de calibration. Finalement, nous avons validé notre système de navigation en effectuant une série d'expériences *in vitro*. La précision du système de reconstruction tridimensionnelle de la forme et de l'orientation de l'aiguille a été évaluée en utilisant deux caméras positionnées perpendiculairement de manière à connaitre la position de l'aiguille dans le système d'axes du laboratoire. L'évaluation de la précision au bout de l'aiguille a quant à elle été faite en utilisant des fantômes précisément conçus à cet effet. Finalement, des interventions guidées en IRM ont été testées et comparées au système de navigation électromagnétique NDI Aurora (EMTS, pour *Electromagnétic tracking system*) par le biais du FRE (*fiducial registration error*) et du TRE (*target registration error*).

Résultats: Lors de nos premières expériences in vitro, la précision obtenue quant à la position du bout de l'aiguille était de 0,96 mm pour une déflexion allant jusqu'à ±10,68 mm. À titre comparatif, le système d'Aurora a une précision de 0.84 mm dans des circonstances similaires.

Les résultats obtenus lors de nos seconds tests ont démontré que l'erreur entre la position réelle du bout de l'aiguille et la position fournie par notre système de reconstruction de forme est de 1,04 mm, alors qu'elle est de 0,82 mm pour le EMTS d'Aurora. Pour ce qui est de notre dispositif, cette erreur est proportionnelle à l'amplitude de déflexion de l'aiguille, contrairement à l'EMTS pour qui l'erreur demeure relativement constante. La dernière expérience a été effectuée à l'aide d'un fantôme en gélatine, pour laquelle nous avons obtenu un TRE de 1,19 mm pour notre système basé sur les FBG et de 1.06 mm pour le système de navigation par senseurs électromagnétiques (EMTS). Les résultats démontrent que l'évaluation du FRE est similaire pour les deux approches. De plus, l'information fournie par les caméras permet d'estimer la précision de notre dispositif en tout point le long de l'aiguille.

Conclusion : En analysant et en interprétant les résultats obtenus lors de nos expériences in vitro, nous pouvons conclure que la précision de notre système de navigation basé sur les FBG est bien adaptée pour l'évaluation de la position du bout et la forme de l'aiguille lors d'interventions RFA des tumeurs du foie. La précision de notre système de navigation est fortement comparable avec celle du système basé sur des senseurs électromagnétiques commercialisé par Aurora. L'erreur obtenue par notre système est attribuable à un mauvais alignement des réseaux de Bragg par rapport au plan associé à la région sensorielle et aussi à la différence entre le diamètre des fibres et celui de la paroi interne de l'aiguille.

ABSTRACT

Background: Colorectal liver metastasis is the leading cause of liver cancer death in the world. In the past decade, radiofrequency ablation (RFA) has proven to be an effective percutaneous treatment modality for the treatment of metastatic hepatic cancer. Accurate needle tip placement is essential for RFA of liver tumors. A promising technology to obtain the real-time information of the shape of the needle is by using fiber Bragg grating (FBG) sensors at high frequencies (up to 20 kHz).

Methods: In this thesis work, we developed an MR-compatible needle tracking technology designed for RFA procedures in liver cancer. At first, three fibers each containing a series of FBGs were glued together and integrated inside a 20G-150 mm needle. Then a three-dimensional needle shape reconstruction algorithm was developed, based on the FBG measurements collected in real-time during needle guidance. The tip position and shape of the reconstructed 3D needle model were represented with respect to the target defined in the image space by performing a fiducial-based registration. Finally, we validated our FBG-based needle navigation by doing a series of in-vitro experiments. The shape of the 3D reconstructed needle was compared to measurements obtained from camera images. In addition, the needle tip accuracy was assessed on the ground-truth phantoms. Finally, MRI guided intervention was tested and compared to an NDI Aurora EM tracking system (EMTS) in terms of fiducial registration error (FRE) and target registration error (TRE).

Results: In our first in-vitro experiment, the tip tracking accuracy of our FBG tracking system was of 0.96 mm for the maximum tip deflection of up to ±10.68 mm, while the tip tracking accuracy of the Aurora system for the similar test was 0.84 mm. Results obtained from the second in-vitro experiment demonstrated tip tracking accuracy of 1.04 mm and 0.82 mm for our FBG tracking system and Aurora EMTS, respectively for the maximum tip deflection of up to ±16.83 mm. The tip tracking error in the developed FBG-based system reduced linearly with decreasing tip deflection, while the error was similar but randomly varying for the EMTS. The last experiment was done with a gel phantom, yielding a TRE of 1.19 mm and 1.06 mm for the FBG and EM tracking, respectively. Results showed that across all experiments, the computed FRE of both tracking systems was similar. Moreover, actual shape information obtained from the camera images ensured the shape accuracy of our FBG-based needle shape model.

Conclusion: By analyzing and interpreting the results obtained from the in-vitro experiments, we conclude that the accuracy of our FBG-based tracking system is suitable for needle tip detection in RFA of liver tumors. The accuracy of our tracking system is nearly comparable to that of the Aurora EMTS. The error given by our tracking system is attributed to the misalignment of the FBG sensors in a single axial plane and also to the gap between the needle's inner wall and the fibers inside.

TABLE OF CONTENTS

ACKNOWLEDGEMENTS III

RÉSUMÉ IV

ABSTRACT VI

TABLE OF CONTENTS VIII

LIST OF TABLES XII

LIST OF FIGURES XIII

LIST OF SYMBOLS AND ABBREVIATIONS XIX

CHAPTER 1 INTRODUCTION 1

1.1 Malignancy of the liver 1

1.2 Percutaneous liver cancer treatments 2

1.3 Research objectives 3

1.4 Thesis structure 4

CHAPTER 2 BACKGROUND 6

2.1 Liver anatomy 6

2.2 Liver cancer 7

2.2.1 Hepatocellular carcinoma 7

2.2.2 Metastatic liver cancer 8

2.3 Treatment of liver cancer 8

2.3.1 Resection operation 9

2.3.2 Nonsurgical treatment 9

2.3.2.1 Ablation therapy 10

2.3.2.2 Percutaneous intratumoral injection 10

2.3.2.3 Microwave ablation (MWA) 10

2.3.2.4 Cryoablation 11
2.3.2.5 Radiofrequency ablation 11
2.4 Summary 12
CHAPTER 3 LITERATURE REVIEW 14
3.1 Image-guided interventions in liver tumors 14
3.1.1 Optical tracking system (OTS) 15
3.1.1.1 Working principle of OTS 15
3.1.1.2 Classification of OTS 16
3.1.1.3 Procedural steps with OTS in IGLI 17
3.1.1.4 Studies of OTS in IGLI 18
3.1.1.5 Advantages of OTS 21
3.1.1.6 Disadvantages of OTS 21
3.1.2 Electromagnetic tracking system (EMTS) 21
3.1.2.1 Working principle of EMTS 22
3.1.2.2 Classification of EMTS 23
3.1.2.3 Procedural steps in image guided intervention using EMTS 23
3.1.2.4 Studies related to EMTS in IGLI 25
3.1.2.5 Advantages of EMTS 26
3.1.2.6 Disadvantages of EMTS 27
3.2 MRI guided interventional procedure 28
3.2.1 MRI guided needle interventions 28
3.3 Optical sensing technology 31
3.3.1 Fiber Bragg Gratings 32
3.3.2 Application of FBG sensors in the medical field 33

3.3.3 Shape sensing 33
3.4 Summary 38
CHAPTER 4 METHODOLOGY 39
4.1 Experimental setup 39
4.2 Needle fabrication 40
4.3 Acquiring sensor data from the Deminsys© interrogator 42
4.4 Calibration procedure 44
4.5 Needle shape reconstruction 46
4.6 Navigation software 47
4.6.1 Real-time visualization of needle profile 47
4.6.2 3D Model generation 48
4.6.2.1 Planar phantoms 48
4.6.2.2 Anatomical gel phantom 49
4.6.3 Robotic system for needle translation 50
4.6.4 Point-based registration 53
4.7 Validation methodology 57
4.8 Summary 58
CHAPTER 5 RESULTS 59
5.1 Needle shape representation in Slicer 59
5.2 Connecting NDI Aurora EMTS with Slicer 61
5.3 In-vitro experiment with planar phantom-1 64
5.4 In-vitro experiment with planar phantom-2 74
5.5 In-vitro experiment with gel phantom 77
5.6 Summary 79

CHAPTER 6 DISCUSSION 81
6.1 Comparing FBG-based tracking with Aurora EMTS 82
6.2 Comparison with other shape sensing methods 85
6.3 MRI compatibility 86
6.4 Maximum curvature supported by our fiber system 88
6.5 Limitations 90
6.6 Summary 90
CHAPTER 7 CONCLUSION 91
BIBLIOGRAPHY 93

LIST OF TABLES

Table 3.1: Classification of MRI guided needle intervention methods with their advantages (light background) and disadvantages (deep background).....30

LIST OF FIGURES

Figure 2.1: Segments of the human liver based on Couinaud segments [12]. Used with permission. 6

Figure 2.2: The image presents the percutaneous radiofrequency ablation (RFA) procedure in the liver (image source from [35]). Used with permission. 11

Figure 3.1: 3D reconstruction by triangulation for an optical tracking system. Image source: http://iotracker.com/indexdaed.html?q=optical_tracking. Used with permission. 15

Figure 3.2: Examples of various commercial OTS with (a) active system (NDI Optotrak), passive system based on (b) retro-reflective infrared markers (NDI Polaris), (c) visible light patterns (Claron MicronTracker), (d) active markers and (e) passive markers. Image source: (a), (b), (d), (e) www.ndigital.com and (c) http://www.clarontech.com. Used with permission. 17

Figure 3.3: Optically tracked surgical tools: (a) active probe, (b) passive probe. (image source: www.ndigital.com) (c) an ex-vivo experiment where optical tracking markers are attached to a gamma probe and phantom [42].Used with permission.....18

Figure 3.4: Application of OTS in the operating room: (a) Polaris localizer camera used to track a surgical instrument in an image-guided liver resection procedure [46], (b) NDI Vicra, a passive OTS mounted in an operating room [47]. Used with permission. 19

Figure 3.5: The prototype surgical navigation system, proposed by Lango et al.; various surgical tools that could be tracked by the proposed system: (a) a preoperative planning pointer that could be used for patient registration, (b) a dedicated intraoperative laparoscopic pointer, (c) a video laparoscope, (d) a grasper for navigation during resection, (e) a radio frequency ablation probe, (f) a flexible ultrasound probe with electromagnetic tracking sensors on the tip [49]. Used with permission. 20

Figure 3.6: Working volume offered by OTS (a) NDI Polaris and (b) NDI Vicra. (image source: www.ndigital.com). Used with permission. 21

Figure 3.7: EMTS working principle. An EM sensor experiences a spatially and temporarily varying magnetic field, produced by the field generator, that induces a current in it. 22

Figure 3.8: Magnetic field generator and sensors of different commercially available EMTS. AC-driven (a) NDI Aurora, (b) Polhemus Fastrak; DC-driven (c) Ascension miniBIRD and (d) passive transponder based "Calypso GPS for the body system" from Varian Medical System Inc. Image source: (a) www.ndigital.com, (b) www.polhemus.com, (c) www.ascension-tech.com, (d) www.varian.com. Used with permission. 24

Figure 3.9: (A) A common EM tracking procedure with the tracking workstation and a US machine for prostate biopsies, (B) EM field generator (circled in blue near the top center of image) is placed close to the target and the fiducial patches (yellow arrow in center of image) [61]. Used with permission. 25

Figure 3.10: A fiber optic cable containing fiber Bragg gratings. 31

Figure 3.11: Principle of fiber Bragg grating sensor [74]. Used with permission. 32

Figure 3.12: Application principle of FBG sensors for shape sensing in minimally invasive surgical tools. 34

Figure 3.13: Reconstructed needle shape while the needle was inserted into a soft-tissue phantom, (a) top view and (b) side view. Mean tip error for (1) single bend (error 1.5±0.8 mm), (2) double bend (error 2.0±0.7 mm), (3) 3D double bend (error 2.1±1.1 mm) and (4) drilling insertions (error 1.7±1.2 mm) [80]. Used with permission. 35

Figure 3.14: 3D Plot of four different fiber shapes, (a) 3D view of the fiber shapes and three corresponding orthogonal views, (b) x-y, (c) x-z, and (d) y-z [86]. The green line segments indicate Bragg gratings locations. Used with permission. 37

Figure 4.1: (a) The complete experimental setup of our FBG-based tracking system, (b) calibration plate holding the needle tip inside a groove,(c)three Newport PM500 linear stages, (d) two manual linear stages, (e) camera-1 and (f) camera-2. 40

Figure 4.2: 3D shape reconstruction of a needle using the shape sensing technique where bending is characterized by the wavelength shift. The left side of the Figure shows the orientation of three FBGs at one triplet. The shift of the wavelengths λ_7, λ_8, λ_9 occurs due to the bending at triplet #3, while the wavelengths $\lambda_1 ... \lambda_6$ remain fixed as no bending takes place at triplets #1 and #2 [88]. 41

Figure 4.3: Image shows a 20G Spinal needle and three fibers glued together. Each fiber includes three FBGs triplets. 42

Figure 4.4: A FBG-based needle with three optical fibers having a 120° configuration. Each fiber has 3 FBGs placed at three different locations (35, 75 and 115 mm) along the needle shaft. 42

Figure 4.5: Web server showing the acquisition settings and acquisition control interface. 43

Figure 4.6: The overall structure of a UDP packet payload provided by the Deminsys interrogator. 44

Figure 4.7: During the calibration procedure, the needle tip is stabilized inside the grooves (a) without bending and (b) with bending for a known amount of displacement of the needle tip. The distance between the successive grooves was 1.4 mm. 45

Figure 4.8: Data flow from FBG data acquisition to visualization of shape sensing in real-time. 48

Figure 4.9: Fabricated planar phantoms, (a) calibration phantom, and (b) validation phantom. ...49

Figure 4.10: (a) Original gel phantom and (b) the generated model from the preoperative MRI image.....50

Figure 4.11: Various parts of the robotic system, (a) vertical and (b) horizontal PM500 linear stages; (c) rear side of a controller and (d) National Instruments GPIB-USB-A Controller for universal serial bus (USB). Image source from: (a-c) www.newport.com and (d) https://www.ni.com. Used with permission. 51

Figure 4.12: Illustration of the communication between the PM500 system and a computer. 52

Figure 4.13: Six multi-modality radiology disk-shaped markers used for the point-based registration.....53

Figure 4.14: In Slicer, fiducial points were selected at the center of the multi-modality radiology disk-shaped markers visible in the MRI DICOM images. 54

Figure 4.15: Several landmarks such as grooves and corners were selected as the fiducials. 55

Figure 5.1: A line is fitted between the measured wavelength-shift and the strain values (calculated from the applied tip bending) to define the calibration matrix. 60

Figure 5.2: Slicer interface showing the reconstructed needle shape with two OpenIGTLink connectors. 61

Figure 5.3: Experimental setup with an Aurora NDI EMTS where the field generator was placed close to the needle tip. 62

Figure 5.4: Acquiring needle tip tracking information from the NDI Aurora system to Slicer through an OpenIGTLink connection. A model in Slicer represents the needle tip with orientation. 63

Figure 5.5: The interface of the module named, 'Fiducial Registration' in Slicer with its input and output parameters. 65

Figure 5.6: Real-time visualization of the reconstructed needle shape in Slicer for various tip deflections using the planar phantom-1. 66

Figure 5.7: TRE is defined as the RMS distance between the actual target location and the estimated needle tip position in Slicer. 67

Figure 5.8: Accuracy of the estimated needle tip position of our FBG-based tracking at various deflections in both (a) *xy* and (b) *xz* planes of phantom-1. 68

Figure 5.9: Real-time visualization of the EM-based needle navigation in Slicer for various tip deflections using planar phantom-1. 69

Figure 5.10: Accuracy of the estimated needle tip position of the Aurora system at various tip deflections in both (a) *xy* and (b) *xz* planes of phantom-1. 70

Figure 5.11: The markers on the needle shaft were used to find the needle shape from the camera images. 71

Figure 5.12: Comparison between the physical and approximated needle shape for several amounts of tip deflections in the xy plane. The plots show the position of the markers on the needle tip along the y-axis. 73

Figure 5.13: Real-time visualization of the reconstructed needle shape with its tip position in Slicer for various amount of tip deflections using planar phantom-2. 74

Figure 5.14: (a) Phantom-2 containing a set of holes and (b) its 3D model, the non-deflected needle tip position is shown as a black star, (c) RMS error distribution of the needle tip position at various deflections (shown in individual color) for the FBG-based tracking system. 75

Figure 5.15: Real-time needle navigation with phantom-2 made in plastic in Slicer using NDI Aurora EMTS for various tip deflections. 76

Figure 5.16: (a) Phantom-2 made of plastic containing a set of holes and (b) its 3D model, the non-deflected needle tip position is shown as a black star, (c) RMS error distribution of the needle tip position at various deflections (shown in individual color) for the Aurora EMTS. 76

Figure 5.17: Needle navigation through various tubes of a gel phantom. The reconstructed needle shapes (shown in blue color) were well inside the segmented tubes. 78

Figure 5.18: Needle navigation using the Aurora EMTS through different tubes of a gel phantom. 79

Figure 6.1: (a) The plastic model of the phantom-2 where white arrows show the distorted holes. (b) 3D model of the phantom-2. 83

Figure 6.2: (a) A needle orientation for which the tip was not tracked by the Aurora system, (b) the tip position (indicated by arrows) is shown well inside the working volume in NDI tool tracker interface. 84

Figure 6.3: Side-by-side physical dimension comparison between a Deminsys© interrogator and an Aurora field generator with its system control unit. 85

Figure 6.4: Image shows the fibers placed inside the bore of a 1.5T MRI scanner. 87

Figure 6.5: The calculated strain of all the FBG sensors both (a) inside and (b) outside the MRI. 88

Figure 6.6: A cylindrical cone shaped plastic object with an inner diameter ranging from 6.2 mm to 30 mm. 89

Figure 6.7: Image shows the curvature measuring experiment where the fibers were wrapped around the plastic object. 89

LIST OF SYMBOLS AND ABBREVIATIONS

AC	Alternating current
BNC	Bayonet Neill–Concelman
CHUM	Centre hospitalier de l'Université de Montréal
CRC	Colorectal cancer
CRLM	Colorectal liver metastases
CT	Computed tomography
DICOM	Digital imaging and communications in medicine
DC	Direct current
EM	Electromagnetic
EMTS	EM tracking system
FBG	Fiber Bragg grating
FBR	Fiducial-based registration
FRE	Fiducial registration error
GPIB	General purpose interface bus
HCC	Hepatocellular carcinoma
IGI	Image guided interventions
IGLI	Image guided liver interventions
IP	Internet protocol
LED	Light emitting diode
MIS	Minimally invasive surgery
MRI	Magnetic resonance imaging
MWA	Microwave ablation
NI	National Instruments

NDI	Northern Digital Inc.
OTS	Optical tracking system
PEI	Percutaneous ethanol injection
PET	Positron-emitting tomography
PDMS	Polydimethylsiloxane
RFA	Radiofrequency ablation
RMS	Root mean square
SVD	Singular value decomposition
SLED	Superluminescent LED
SCU	System control unit
TRE	Target registration error
3D	Three dimension
UDP	User Datagram Protocol
US	Ultrasound
USB	Universal serial bus
UV	Ultraviolet

CHAPTER 1 INTRODUCTION

1.1 Malignancy of the liver

The liver is a vital organ which is at the core of our metabolism and performs various important functions. Cancers may arise from the liver itself or more commonly, spread to the liver from other parts of the body. As venous blood from the intestine must pass through the liver, colon cancers are by far the most common type of cancerous lesions of the liver. Colorectal cancer (CRC) is the leading cause of cancer death in the world, causing over 600,000 deaths per year [1]. Approximately 1.2 million new cases of CRC are diagnosed each year [1]. In Canada, one in fourteen males and one in sixteen females are expected to develop CRC in the course of their lifetime [2]. An alarming increase by 79% by the year 2030, has been predicted [3]. About 20% of CRC cases have liver metastasis (CRLM) at the time of diagnosis and about 50% will develop them during the course of the disease. The incidence of primary liver cancer (mostly hepatocellular cancer, HCC) has also increased worldwide over the last several decades. HCC results in one million deaths worldwide per year. Thus, liver cancer is a very significant clinical problem. Involvement of liver from any cancer usually means the disease is in an advanced stage with a poor prognosis. If left untreated, survival in these cases is usually up to 6-12 months [4].

Generally speaking, treatment of these CRLM and HCC lesions depends on the type, location and stage of cancer, reserve of liver function and normal parenchyma, and patient overall health. Resection of the liver lesion(s) along with resection of the primary colon tumor is the only potentially curative treatment for metastatic CRC. Unfortunately, only about 10% of the CRC patients with liver metastases are eligible for this type of curative surgery. The large size of the primary colon or liver lesion, extensive local spread of the primary colon cancer, multifocal tumors involving various segments of liver, underlying liver disease and other comorbidities usually render most of the patients surgically unfit. If the liver lesion(s) cannot be resected but the patient is otherwise a candidate for surgery, liver transplantation can be the next curative option. Unfortunately, there is a long waiting time for liver transplantation due to the shortage of donor livers. Furthermore, most patients do not meet the stringent criteria for liver transplantation and neither can have resection. In lieu of resection, various palliative treatments are used ranging from local ablation, regional chemotherapy and local radiotherapy to systemic chemotherapy.

While these therapies are mostly for disease control (not curative) and for prevention or treatment of complications, they are increasingly being used to keep the current transplant candidates eligible by reducing tumor burden and preserving healthy liver tissue. In some cases, successful locoregional therapies may render an otherwise non-transplant candidate eligible for a liver transplant.

1.2 Percutaneous liver cancer treatments

Ablation of liver tumor is possible by targeted delivery of a lethal dose of various types of chemicals (alcohol or acetic acid) or energy (heat, microwave, laser). Various devices and methods are available to perform hepatic tumor ablation during laparotomy or laparoscopy but also through percutaneous interventional radiology procedures. In recent years, radiofrequency ablation (RFA) has emerged as the most widely used tumor ablative technique for the treatment of CRLM and HCC [5]. It is effective, relatively safe, cheap and can be performed as an outpatient procedure. Under ultrasound (US) guidance a needle or electrode is placed in the center of the lesion. When RF energy is transmitted to the lesion through the electrode, mobile ions in the surrounding tissue attempt to travel in the alternating directions of the electric field. The movement of these ions raises the temperature (>60°C) causing tissue damage and cancer cell death. RFA is used to treat small lesions having a diameter less than 3.5 cm.

During a typical RFA procedure to ablate a liver cancer lesion, real-time ultrasound (US) is used to guide a needle as close as possible to the target tumor that was previously identified in computed tomography (CT) and/or magnetic resonance (MR) diagnostic imaging. However, in many cases, US cannot show the tumors that were visible in CT or MR for various reasons [6, 7]. Also, during thermal ablation, microbubbles are formed that appear as hyperechoic artifacts with shadows in US images, limiting the visibility significantly, requiring multiple needle insertions. To overcome these problems, multimodal image fusion (to localize the lesions exactly based on registration data from different image techniques, like CT, MR and US) and various needle tracking technologies (usually, electromagnetic or optical) are utilized to track the position of the needle tip in real-time. However, electromagnetic (EM) tracking suffers from interference caused by electromagnetic induction of nearby ferromagnetic materials such as a metallic operation table or any metallic medical diagnostic devices. EM tracking is also incompatible with MR-guided interventions because of the magnetic field interference between the local field generator and the

MR magnet [8]. In the case of optical tracking, the "straight line of sight" requirement limits tracking to the tip of a bent needle [9]. In actuality, precise needle tip placement becomes further challenging due to needle tip deflection caused by needle asymmetry (beveled tip) and due to inhomogeneities in the liver tissue, especially with increasing insertion depth and needle length [10]. Without precise positioning of the needle tip into the center of the target lesion, adequate energy is not delivered to ablate the tumor and adjacent healthy tissue is damaged. Therefore, it is essential to correctly track the needle in real-time for successful delivery of radiofrequency energy. An alternative tracking technology free of limitations of EM or optical tracking, yet MR compitable, is needed.

A promising technology to obtain real-time information of the needle shape is by using fiber Bragg grating (FBG) sensors. An FBG sensor is a type of distributed Bragg reflector constructed inside the core of a glass fiber that reflects one specific wavelength and transmits all others. These miniature FBGs are immune to electromagnetic interference and are capable of accurately sensing even submicron displacement. They are also able to provide read-out at a high sampling rate (>20 kHz), which is important for real-time tracking of a medical device. By placing a series of FBGs along the ablation needle and reading each of them via optical multiplexing, it is possible to retrieve precise, real-time data of the fiber inside the needle. Thus, the 3D shape of the entire needle can be reconstructed by using the MR-compatible FBG sensor measurements that could safely track the needle in real time and in a strong electromagnetic field during MRI-guided interventions on liver tumors, satisfying the main objective of this study.

1.3 Research objectives

In this research project, the global objective was to develop an MR-compatible needle tracking technology designed for RFA procedures in liver cancer. Towards this end, the 3D shape reconstruction of a flexible needle using FBG sensor measurements was studied. The specific objectives of the project were as follows:

(i) Construction of the needle tracking device: Three optic fibers each containing a series of FBGs, were glued together so that the FBG sensors across the fibers were aligned and oriented in 120° to each other. Then, we integrated these three fibers inside a 20G-150 mm needle.

(ii) Development of 3D shape reconstruction algorithm: Once the needle prototype was fabricated, we developed a three-dimensional needle shape reconstruction algorithm based on the FBG measurements collected in real-time during needle guidance.

(iii) Implementation of a navigation software: In addition, to infer the position and 3D shape of the needle in real-time during the RFA procedure, it is important to visualize the needle's position and shape with respect to the internal anatomy of the patient based on a prior CT or MRI imaging. So, the next step was to perform a fiducial-based registration (FBR), by identifying markers on the patient in order to register the FBG tracking space with the image space of the preoperative MRI and to visualize the needle in the image space. actual shape information obtained from the

(iv) In-vitro validation: Finally, we validated FBG-based needle navigation by doing a series of in-vitro experiments. The shape of the 3D reconstructed needle was compared to the measured shape information of the needle obtained from camera images. Needle tip tracking accuracy was also assessed on a ground-truth phantom. Lastly, MRI guided tracking was tested and compared to EM tracking system (EMTS) in terms of fiducial registration error (FRE) and target registration error (TRE).

1.4 Thesis structure

The remainder of this thesis is organized as follows. Chapter 2 presents background information related to this project such as the etiology of liver cancer and various treatment techniques available. Various ablation therapies for CRLM and HCC as well as their individual pros and cons and corresponding mortality and morbidity outcomes are described. Chapter 3 gives an overview of tracking technologies for image guided liver interventions, describes needle tracking techniques under MRI guidance and provides a literature review of optical shape sensing technology. Chapter 4 first describes needle fabrication and FBG calibration processes followed by the methodology for reconstructing the shape of the needle in 3D. This chapter also shows the steps needed to generate various synthetic phantoms used for this project. The results of all the in-vitro experiments with our FBG-based tracking system are presented in Chapter 5. The results obtained from the NDI Aurora system for similar experiments are also demonstrated for comparison. The experimental results are discussed and analyzed in Chapter 6 along with the

limitations of our developed system. Finally, Chapter 7 summarizes the project and proposes future extensions.

CHAPTER 2 BACKGROUND

This section presents the background related to this research project. First, the anatomy of the liver, primary (hepatocellular carcinoma, HCC) and secondary (or metastatic) malignant tumors of the liver will be briefly described. Various treatments of CRLM and HCC such as surgical resection, liver transplantation and different types of locoregional therapies will be presented next along with their advantages and limitations. RFA will be discussed in detail along with some of the challenges with prior image registration and intra-procedure needle tracking.

2.1 Liver anatomy

The liver is the largest organ in the abdomen weighing approximately 1500 g [11]. It is located under the diaphragm to the right side of the abdomen, almost entirely covered the rib cage. The liver moves with respiration and from pulsation from blood circulation in the hepatic arteries. It possesses one large right lobe and a much smaller left lobe. The two other minor lobes called caudate and quadrate lobes, can be seen on the posterior surface.

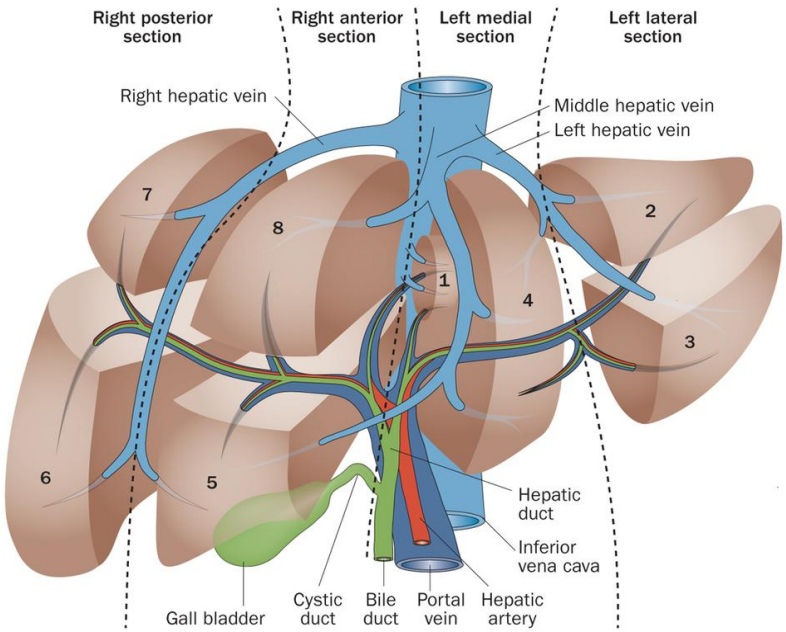

Figure 2.1: Segments of the human liver based on Couinaud segments [12]. Used with permission.

The major blood vessels (portal vein and hepatic artery) after entering the liver divide into right and left branches and supply respective lobes of the liver. However, from a more functional-

anatomic point (Couinaud classification) [13], the liver can be divided into eight independent segments (see Figure 2.1). Every segment has its individual vascular inflow (segmental portal vein and hepatic artery), outflow (segmental hepatic vein) and biliary drainage (biliary duct). The segmental anatomy is the basis for various types of anatomic liver resections. Blood enters the liver through the portal vein (75%) and hepatic artery (25%) [14]. The portal vein, formed by the union of the splenic vein and superior mesenteric vein, brings blood to the liver from the spleen and gastrointestinal tract. The hepatic artery is a branch of the celiac artery and provides 50% of the oxygenation of the organ. The hepatic artery in the liver is divided into two lobar branches, left and right hepatic arteries and each branch gives rise to segmental branches and further ramifications in the parenchyma [15]. The vascular outflow from each segment (segmental veins) links to form the right, middle and left hepatic veins which later merge into the inferior vena cava.

2.2 Liver cancer

Based on the origin of cancer, liver cancer can be classified into primary (originates in the liver) and secondary or metastatic cancer (cancer cells spread by blood from other organs, embed in the liver and then grow to become a mass). Among primary liver cancers, hepatocellular carcinoma (HCC) is the most common, while colorectal liver metastasis (CRLM) is the most common among the secondary liver cancers.

2.2.1 Hepatocellular carcinoma

Hepatocellular carcinoma (HCC) is the most common primary liver cancer [16], accounting for 662,000 deaths worldwide each year [17]. In fact, HCC is the sixth most frequent malignancy and the third leading cause of cancer death worldwide [18]. It is more prevalent in sub-Saharan Africa, China, Japan, central and southeast Asia [18]. Chronic viral hepatitis due to hepatitis B and C viruses, liver cirrhosis from other causes like alcohol and obesity (non-alcoholic fatty liver disease), various toxins and chemicals are identified as likely reasons for HCC. Men in the age group of 30-50 years are affected 2-5 times more frequently than women in similar age group [19]. HCC usually presents at a late stage and life expectancy of non-operable cases at diagnosis ranges between 6 and 24 months [20]. Overall survival rates at 1-year, 3-years, and 5-years have been reported as 66.1%, 39.7%, and 32.5% [20].

2.2.2 Metastatic liver cancer

Cancers originating from other organs like colon, pancreas, lungs or breasts spread to the liver through the bloodstream and lymphatic drainage. However, the majority of liver metastases arise from colorectal cancer as venous blood from the intestine drains through the liver. In fact, 20% of CRC cases have liver metastasis at diagnosis and another 30% develop them during disease progression. With an annual incidence of 1.4 million of CRC worldwide, CRLM continues to be a severe health problem. Naturally, liver metastases are more common than primary liver cancers. Life expectancy without treatment is 6-12 months and the five-year survival rate is <5%. Even with modern chemotherapy, only <10% of patients with metastatic colon cancer who could not have a resection remain alive after five years. With resection of limited CRLM and primary colon cancer combined with chemotherapy, this can be increased to 50% [21].

2.3 Treatment of liver cancer

Malignant liver lesions are treated with a variety of therapeutic modalities, which is an active research area by itself. Though treatments and patient selection vary from institution to institution and country to country, in general, surgical resections (of segments or lobes), liver transplantation, various types of locoregional therapies and systemic chemotherapy, alone or in combinations are typically used to treat HCC and CRLM. Various local treatments include: surgical resection of the affected part of the liver and local ablation of the tumor using different techniques like instillation of ethanol or acetic acid, hyperthermic coagulation using radiofrequency, microwave or laser, cryotherapy, transhepatic arterial chemoembolization, radioembolization and hepatic intra-arterial chemotherapy. These modalities may be employed alone or in various combinations. Resection is potentially curative in HCC and has the best outcome. Resection of the limited liver metastatic lesion with the removal of the primary colon tumor in combination with chemotherapy can be curative in CRC. Liver transplant is another potentially curative treatment for HCC without extrahepatic spread. Many factors like tumor size, number and location in liver, reserve of healthy liver tissue and function, and surgical fitness dictate which method is best for an individual patient.

2.3.1 Resection operation

When patients are eligible for surgery, resection offers the best outcome in the treatment of HCC and some cases of CRC with limited CRLM. Surgical removal of primary colon lesions along with surgical removal of limited metastatic lesion(s) in liver combined with pre- and/post-operative chemotherapy can be curative in >40% cases. Resection of liver metastasis also helps systemic chemotherapy by reducing the cancer burden. This technique involves surgically removing the portion of the liver harboring cancer, while carefully preserving healthy residual parenchyma. During a resection, up to 80% of the volume of liver can be removed. The 5-year survival rate of patients with isolated liver metastases from CRC treated with resection is between 30% and 58% [22]. However, 90% of patients with metastatic CRC are not candidates for surgical resection due to bilobar disease, proximity to critical structures that precludes complete resection, and comorbidities rendering patients unfit [23]. Due to better surgical techniques, this area is changing quickly and more and more patients are now offered resection that in the past were deemed to have unresectable tumors. Tumor recurrence after surgical resection is common, especially if the resected margin is positive for cancer (70% of the patients at five years) but also due to microvascular invasion and satellite nodules [24, 25]. Improvements in surgical techniques, post-resection chemotherapy and use of RFA showed promising results.

2.3.2 Nonsurgical treatment

Most of the patients with CRLM are unsuitable for liver resection or transplantation due to the extent of the disease (multiple metastases, locations), limited healthy hepatic parenchyma and lack of a donor. Various locoregional treatments and systemic therapies are available in this situation to prevent tumor progression and delay the need for systemic chemotherapy. Ablation of the tumor is done through intratumoral injection of chemicals, radiofrequency ablation (RFA) or new technologies, such as microwave or laser ablation. Cryoablation and irreversible electroporation are other ablative methods. Results of systemic chemotherapy (using fluorouracil, leucovorin, oxaliplatin, irinotecan, bevacizumab, etc.) in advanced CRC are good, where it (mostly sorafenib) is mostly used as a palliative therapy.

2.3.2.1 Ablation therapy

Ablation is a minimally invasive treatment that applies an effective toxic or lethal dose of chemicals or temperature change (high or freezing temperature) on the cancerous area to kill the cancer cells. Ablation is done by intratumoral injection of acetic acid or ethanol, radiofrequency ablation (RFA) or using new technologies, such as microwave, laser, irreversible electroporation or cryogenics. The percutaneous route is usually preferred while lesions in the dome of the liver or close to the inferior liver margin are treated laparoscopically or need a laparotomy. However, access to the tumor is not always possible and risks of bowel perforation, ischemic liver injury, bleeding, and infection are present.

2.3.2.2 Percutaneous intratumoral injection

Percutaneous ethanol injection (PEI) generally requires repeated sessions: tumors less than 2 cm usually need 3 to 4 sessions, while tumors 2 to 3.5 cm are treated in 8-12 sessions. This technique is effective for small tumors (<3 cm) [26]. It is more efficient in treating HCC lesions than CRLM as HCC has a capsule, which together with the surrounding cirrhotic liver tissue prevents dissemination of the alcohol or acetic acid. Complications of PEI were addressed in a report of 270 patients with small liver tumors (≤2 cm) where the major complication rate was only 2.2% and no mortality was reported [27].

2.3.2.3 Microwave ablation (MWA)

In the case of microwave ablation (MWA), a thin microwave antenna is placed percutaneously directly into the tumor to deliver electromagnetic microwave energy. The microwaves create an agitation of water molecules inside or near the tumor regions, causing friction that generates heat leading to cancer cell death via coagulation necrosis. The main advantages of MWA over other thermal ablation techniques are: 1) increased stability in higher intratumoral temperature, 2) ability to ablate larger tumor volumes, 3) quicker ablation times, and 4) improved convection profile to cover the tumor [28]. Most of the data are from Asian countries and recent studies demonstrated complication rates of 14.2 to 20.6% [29]. A study of 94 RFA treatments for 224 lesions in 87 patients reported overall mortality rate of 2.3% [30].

2.3.2.4 Cryoablation

This technique involves inserting cooled thermally conductive fluids, such as liquid nitrogen and argon gas, into the tumor through cryoprobes to freeze the tumor cells. The main drawback with cryoablation is that it requires laparotomy. Cryoshock has a reported mortality of 8% [31] along with other local complications such as hemorrhage, subphrenic abscesses, bilomas and biliary fistula [32], restricting its use in current clinical practice. Several studies with cryoablation reported high complication rate (>50%) [33] and high mortality rate (maximum of 17%) [34].

2.3.2.5 Radiofrequency ablation

Radiofrequency ablation (RFA) is a popular treatment modality for unresectable hepatic tumors in a non-transplant candidate. It is usually performed percutaneously, by an interventional radiologist, as an outpatient (i.e. without being admitted to a hospital) procedure. RFA is a safe and effective. A typical RFA procedure involves inserting a needle inside a target liver tumor through the skin (percutaneously, but can also be done laparoscopically) under image (commonly ultrasound) guidance. Once the needle tip is inserted in the center of the cancerous lesion, 400 to 500 KHz sinusoidal excitation is applied from the RFA source.

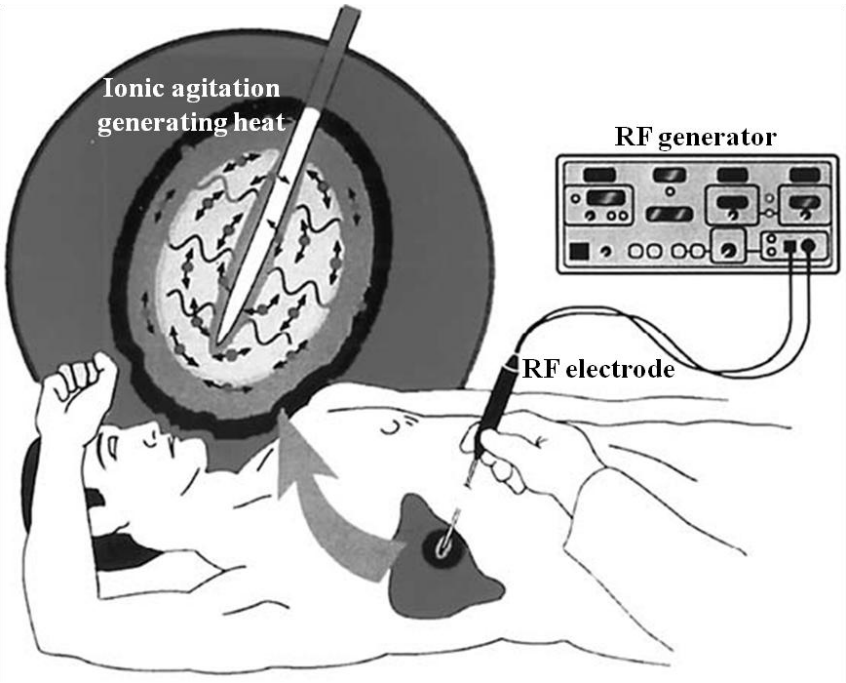

Figure 2.2: The image presents the percutaneous radiofrequency ablation (RFA) procedure in the liver (image source from [35]). Used with permission.

Due to the RF current flow in the lesion, mobile ions in the surrounding tissue attempt to travel in alternating directions of the electric field. The movement of these ions (also called, "ionic agitation") produces heat that spreads into surrounding tissues until thermal equilibrium is achieved. Typically, the temperature for ablation ranges from 50° to 100°C. Above 45-50°C tissue damage is caused by thermal coagulation and protein denaturation while cell death occurs at around 60°C.

Various types of needle electrodes have been developed that deploy an array of multiple curved stiff wires (diameter of 2~4 cm) in the form of an umbrella. RFA is suitable for CRLMs that are smaller than 3.5cm and not located close to major blood vessels [36]. However, tumors having diameters of ≥5 cm are unsuitable for complete ablation using the current RFA devices and requires multiple sessions. A meta-analysis of 1000 RFA treatments for 2140 lesions in 664 patients showed that the number of needle insertion increases as the size of the tumor increases - mean number of needle insertions is 1.5, 2.3, 4.2 and 11.7 times for nodules of <2, 2.1 to 3, 3.1 to 5, and >5 cm, respectively [37].

Generally, the overall survival rates of patients treated with RFA at 3 and 5 years are 70-91% and 48-77% [38], respectively which are higher than those of patients treated with other ablative treatments. The similar survival rates of patients at 3 and 5 years with PEI are 54% and 39% [39], respectively and with MWA are 72%, and 52%, respectively [40]. Even though RFA was primarily developed for patients who were not suitable for surgical resection, its application has expanded as a bridging therapy to convert nonresectable tumors to resectable ones [41]. The main advantages of RFA over other ablation techniques are its cost-effectiveness and its low complication rates. It has a local recurrence rate of 3.6-6% and procedural mortality rate of up to 2%. The limiations are: difficulty with percutaneous access of the tumor, close proximaty (<1cm) of the tumor to major blood vessels rendering RFA unsuitable due to heat sink effect from rapid blood flow and the difficulty of assessing the extent of tissue damage.

2.4 Summary

This chapter highlighted the etiology of liver cancer and the various treatment techniques for liver cancer, particularly for CRLM. Even though surgical resection is considered as the gold standard to treat CRLM, unfortunately, only 10% of patients are eligible for this treatment. Among non-surgical treatments, RFA is accepted as the primary ablative modality due to its cost-

effectiveness and low complication rates. The next chapter will focus on image-guidance systems for RFA.

CHAPTER 3 LITERATURE REVIEW

This section begins with an overview of various tracking technologies for image guided interventions (IGI); In particular, image guided liver interventions (IGLI) such as thermal ablation of the tumor with RFA, MWA, etc. and surgical resection. Various needle tracking techniques under MRI guidance are also discussed. It also highlights the problems and limitations of the existing tracking technologies, especially in an MRI suite or operation room containing ferromagnetic materials. Recent applications of the optical shape sensing technology as an alternative tracking system to circumvent issues related to incompatibility of the MRI and electromagnetic tracking, are also reviewed.

3.1 Image-guided interventions in liver tumors

Image-guided intervention for liver tumors is challenging because of a complex anatomical structure and large deformation of the liver topology, as well as patient's breething and changes in posture. Typically, a surgical plan is performed based on the preoperative CT or MRI scans, due to their ability to visualize precisely the location of tumor in relation to vascular structures and surrounding anatomy. During intervention, this plan is transferred to the operating theater, to match the patient's anatomy with the corresponding structures seen in preoperative images. A proper alignment of the coordinate systems, commonly called “image-to-patient registration”, is essential to achieve precise positioning of the surgical tools in the preoperative image space. A soft-tissue organ such as the liver deforms significantly during surgery because of the patient being under the effect of anesthesia or positioned differently on the surgical table, or for laparoscopy due to distention of the abdomen with gas. Therefore, the surgeon cannot rely on the preoperative image alone to estimate the location of the tumors and related vessels under the surface or inside the liver. Generally, intraoperative navigation of a needle or catheter is facilitated by using a real-time intraoperative imaging system, such as ultrasound imaging, incorporating with various tracking technologies such as electromagnetic or optical systems. In this section, we describe the general working principles and the classification of various tracking systems along with their applications in IGLI and surgical resection. Challenges for each of the tracking systems are highlighted, which will motivate the introduction of a novel tracking technology.

3.1.1 Optical tracking system (OTS)

In its early years, optical tracking was the most established tracking modality for IGI due to its relatively high accuracy over a large workspace. It is widely used in image-guided surgery to determine the position and orientation of line-of-sight surgical instruments.

3.1.1.1 Working principle of OTS

OTS includes two components: a series of cameras and markers/patterns. The working principle relies on triangulation. Typically a set of cameras, mounted at known positions from each other, capture the images of the markers attached rigidly to the surgical tools (as shown in Figure 3.1). The markers are segmented in the camera images and from these segmented images, the disparity of the markers in each frame is calculated, which then allows calculating the 3D position of the markers. If the 3D positions of at least three markers are known, the 3D orientation of the surgical tool can be computed directly.

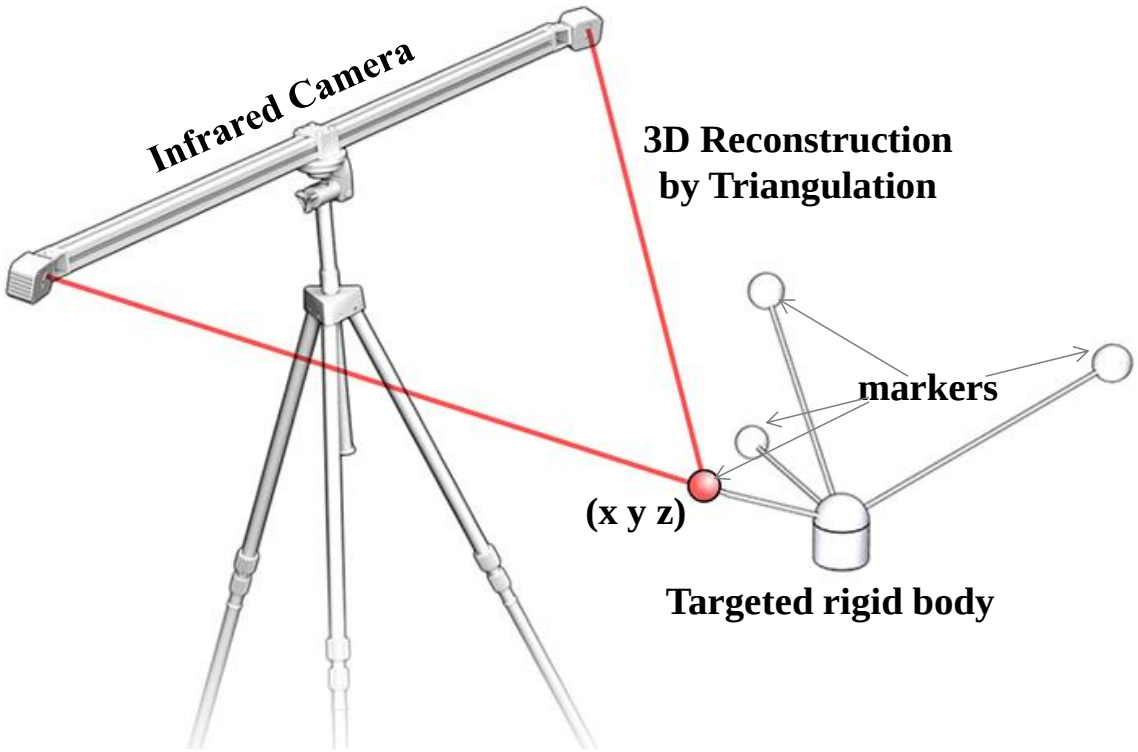

Figure 3.1: 3D reconstruction by triangulation for an optical tracking system. Image source: http://iotracker.com/indexdaed.html?q=optical_tracking. Used with permission.

3.1.1.2 Classification of OTS

OTS can be classified into two categories: active and passive tracking. The active system (e.g. Northern Digital Inc., (NDI) Optotrak) uses a collection of (minimum of three) infrared light emitting diodes (LEDs) attached to a surgical tool in a fixed and non-symmetric fashion. LED markers can emit signals on their own (referring to the term "active") to be received by cameras. The non-symmetric arrangement of the markers ensures correct determination of the pose of the surgical tools from the camera images. The active systems are typically wired, so the markers can be identified implicitly by activating them in a sequence. Therefore, more than one surgical tool having similar marker topology can be tracked.

In contrast, passive OTS uses markers that cannot generate signals by themselves and need external activation to be localized (hence the term "passive"). The passive system itself can be divided into two further categories, one that uses retro-reflective infrared markers (e.g. NDI Polaris) and another that is based on visible light patterns (e.g. Claron MicronTracker). In the former passive system, a group of spherical retro-reflective markers is lit up when infrared light is emitted onto them. As a result, the markers appear as circles in the infrared camera images, irrespective of their orientation. However, as all the markers look identical to each other in the images, the topology of the markers attached to the surgical tools should be distinct from others. The later passive system uses known, specific patterns that have high contrast edges for robust segmentation. The benefit of these patterns is that they can be tracked by a stereo camera pair, without the assistance of infrared markers.

Overall, the performance of the tracking system may be improved by optimizing the camera and marker configuration. For example, increasing the distance between the cameras increases fiducial registration error, while target registration error (TRE) can be reduced by increasing the distance between markers attached to a single surgical tool. However, a larger camera system also requires a larger working space and handling of larger surgical tools might be problematic during an intervention. Figure 3.2 shows various commercial OTS available in the market.

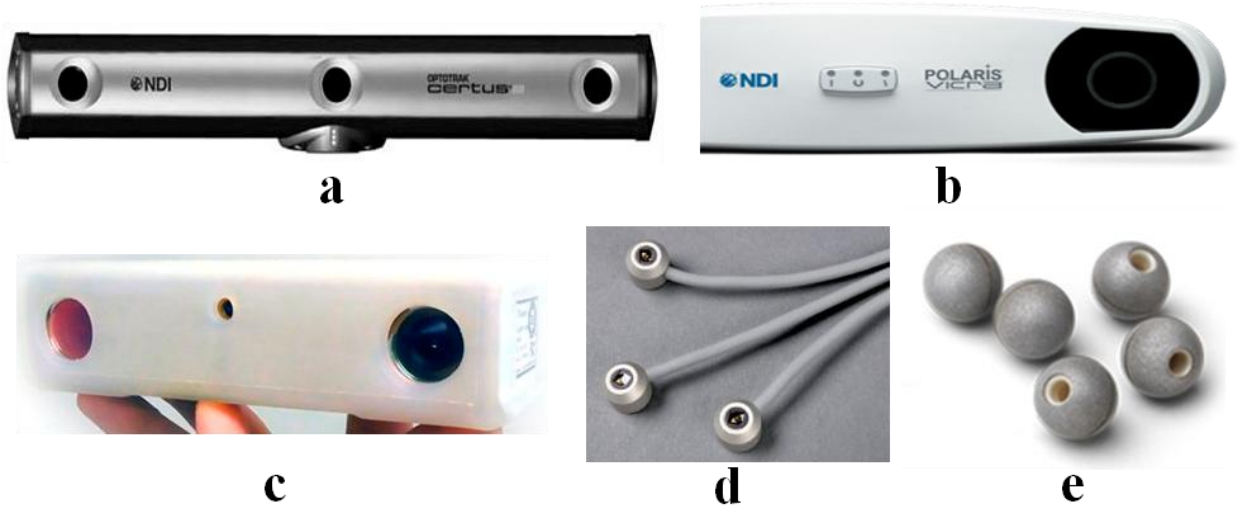

Figure 3.2: Examples of various commercial OTS with (a) active system (NDI Optotrak), passive system based on (b) retro-reflective infrared markers (NDI Polaris), (c) visible light patterns (Claron MicronTracker), (d) active markers and (e) passive markers. Image source: (a), (b), (d), (e) www.ndigital.com and (c) http://www.clarontech.com. Used with permission.

3.1.1.3 Procedural steps with OTS in IGLI

Optical tracking systems can track markers attached to a surgical tool, patient or object that needs to be located in real-time (as shown in Figure 3.3). For percutaneous procedures, at least, three markers are mounted on the needle base. Calibration of the needle is performed to determine the transformation between the markers and the needle tip, subsequently allowing an OTS to track the needle tip in real-time.

An image-to-patient registration (typically, fiducial-based registration) is done so that the needle tip can be guided precisely to a selected target in the preoperative image space. During a registration procedure, a set of landmarks in the preoperative image is selected and the corresponding positions of the landmarks in patient space are retrieved by touching the markers with the needle tip. Finally, a verification step is performed to validate the registration accuracy to ensure reliable navigation of the needle.

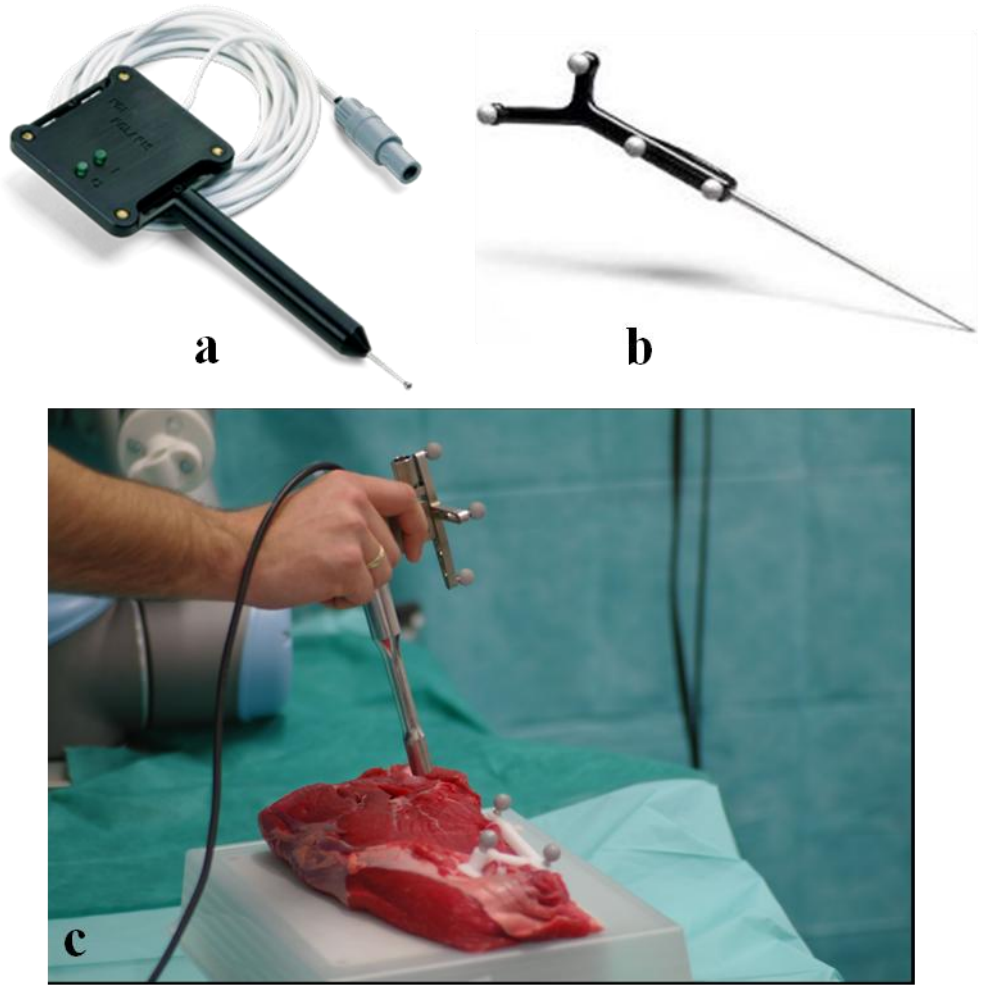

Figure 3.3: Optically tracked surgical tools: (a) active probe, (b) passive probe. (image source: www.ndigital.com) (c) an ex-vivo experiment where optical tracking markers are attached to a gamma probe and phantom [42]. Used with permission.

3.1.1.4 Studies of OTS in IGLI

Herline et al. reported one of the earliest image-guided hepatic surgery systems in 1999. They developed a liver motion compensation model which they tested on a porcine liver to investigate the tracking accuracy of surgical tools using an OPTOTRAK 3020 OTS (NDI, Waterloo, ON, Canada) in open and laparoscopic surgeries [43]. Cash et al. extended this work by incorporating a commercially available laser range scanner (RealScan 200C; 3D Digital Corp., Sandy Hook, CT, USA) in open abdominal hepatic tumor resections for the liver surface registration [44]. Intraoperative data obtained from a laser range scanner were shown to be more robust and yield

accurate registration results compared to the optical tracker, as the laser scanner was capable of acquiring thousands of points on the liver surface [45].

Figure 3.4: Application of OTS in the operating room: (a) Polaris localizer camera used to track a surgical instrument in an image-guided liver resection procedure [46], (b) NDI Vicra, a passive OTS mounted in an operating room [47]. Used with permission.

Lange et al. used another optical tracking system, (NDI Polaris, Waterloo, ON, Canada) for a 3D US based navigation system aimed at tumor resection [46] (as shown in Figure 3.4(a)). An intraoperative US image, obtained from a tracked 3D US probe, was matched with a preoperative CT image using a non-rigid registration algorithm. Another method for open surgery was proposed by Markert et al. [48]. Their method was based on manual registration between a 3D vascular model extracted from the intraoperative 3D ultrasound image and the preoperative CT-based model. Optical sensors were attached to the US probe and were tracked by an optical position measurement system (NDI Vicra®, Waterloo, ON, Canada) to get the spatial orientation [48]. In another study, Peterhans et al. also used NDI Vicra OTS (shown in Figure 3.4(b)) to develop a navigation system for efficient visualization and tool guidance during surgery. Their simple and clinically applicable navigation system was validated on nine patients [47].

The studies described so far are related to open liver surgery. However, in the case of minimally invasive surgery (MIS), the surgeon does not have the privilege of direct visualization of the liver or the operating field. This limitation has motivated the development of image-guided navigation systems that allow effective navigation of surgical tools to the estimated tumor location laparoscopically. Typically, a small laparoscopic ultrasound probe, capable of generating 2D images, is inserted into the patient's body through a small incision. These laparoscopic US

images are combined with the tracking system to improve the safety, accuracy, and outcome of the overall laparoscopic surgery. Lango et al. developed a navigation prototype for laparoscopic surgery, which could be used with an optical (e.g. NDI Polaris) or an electromagnetic (e.g. NDI Aurora) tracking system (Figure 3.5) [49]. Beyond the live scene obtained via the laparoscope alone, the surgeons benefited from the augmented laparoscopic images with the intraoperative ultrasound data [50].

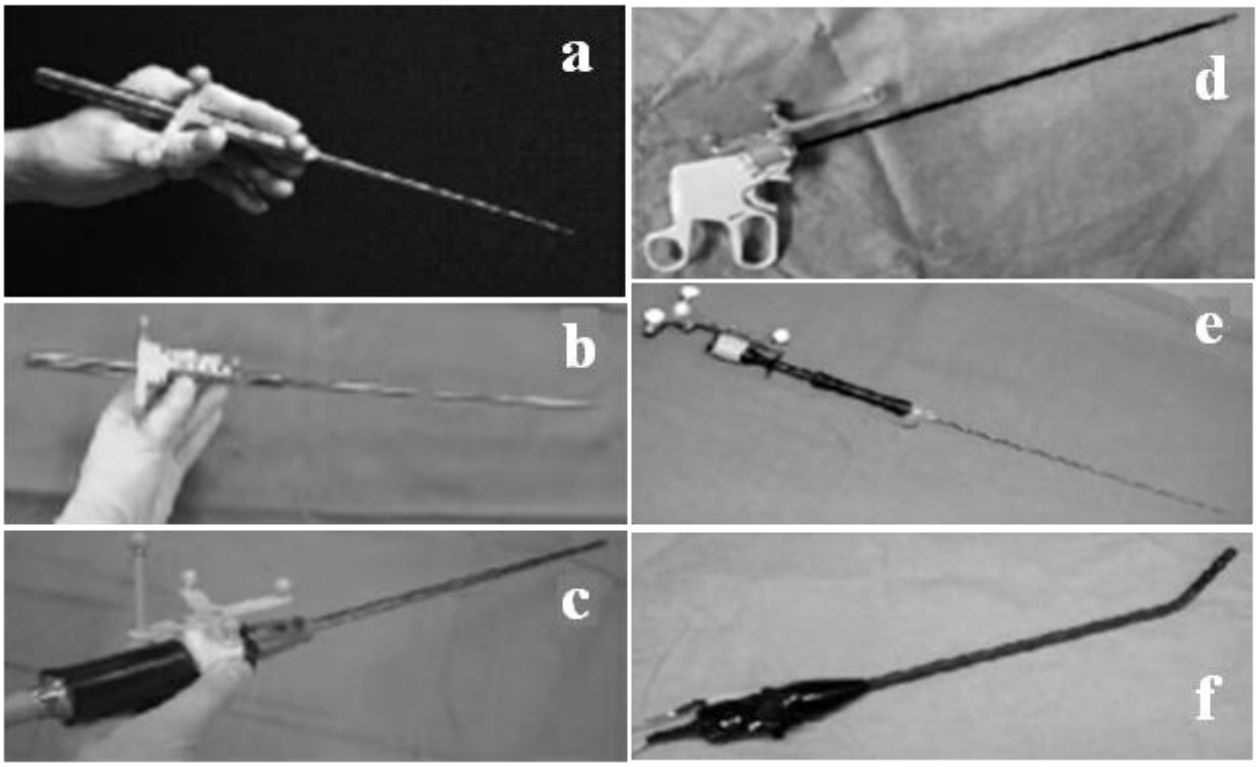

Figure 3.5: The prototype surgical navigation system, proposed by Lango et al.; various surgical tools that could be tracked by the proposed system: (a) a preoperative planning pointer that could be used for patient registration, (b) a dedicated intraoperative laparoscopic pointer, (c) a video laparoscope, (d) a grasper for navigation during resection, (e) a radio frequency ablation probe, (f) a flexible ultrasound probe with electromagnetic tracking sensors on the tip [49]. Used with permission.

Feuerstein et al. used an OTS, consisting of four optical tracking cameras (ARTtrack2, ART GmbH), to determine the position and orientation of both the mobile C-arm scanner and the laparoscope in a single coordinate system [51]. So, additional registration was not required to augment the intraoperative CT on the live laparoscopic video.

3.1.1.5 Advantages of OTS

The main advantage of OTS is that it can offer a large working volume (as shown in Figure 3.6) with sub-millimeter accuracy. According to NDI, the major manufacturer of medical tracking systems, the positional accuracy of NDI Polaris OTS is 0.50 mm with a precision of 0.25 mm [52]. It is not susceptible to magnetic interference, so can be used alongside MRI or in the presence of other metal objects. Also, a wireless system simplifies the operation environment.

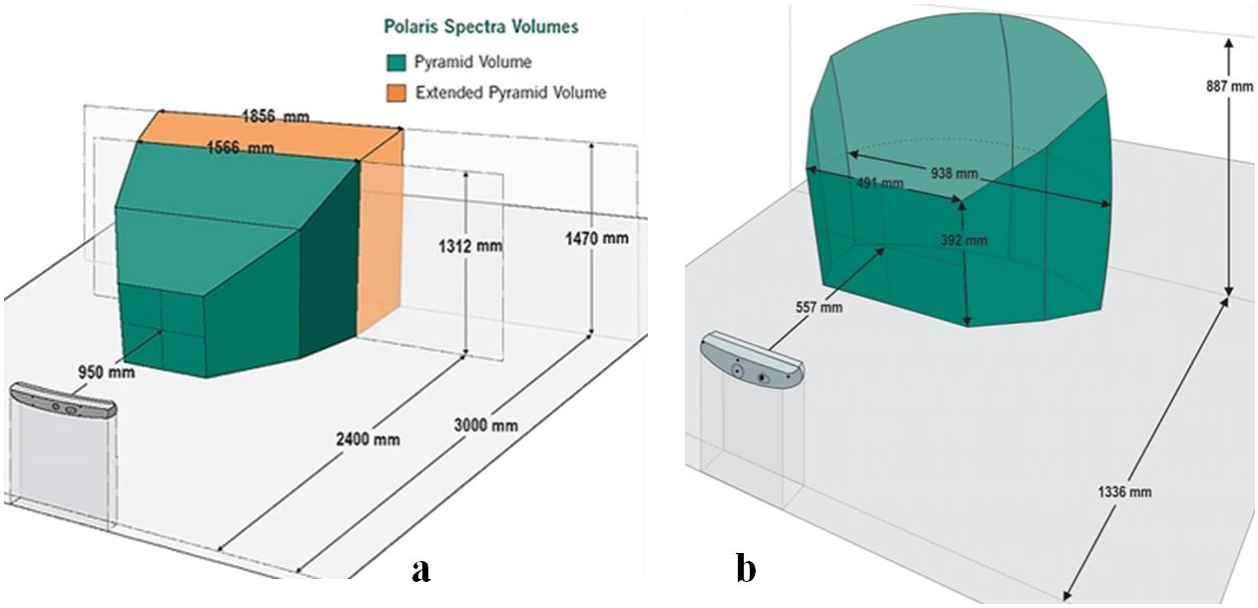

Figure 3.6: Working volume offered by OTS (a) NDI Polaris and (b) NDI Vicra. (image source: www.ndigital.com). Used with permission.

3.1.1.6 Disadvantages of OTS

On the other hand, OTS requires an unobstructed line of sight between the cameras and the tracked instruments. This constraint limits the application of OTS tracking the instrument inside the patient. For example, the tip of a flexible needle that is not visible by the cameras cannot be tracked directly. Besides, the attachment of a set of markers to the tracked instruments often makes their use very cumbersome.

3.1.2 Electromagnetic tracking system (EMTS)

The advent of the electromagnetic tracking system (EMTS) occurred as a method of choice where the line of sight is blocked, since OTS is no longer a suitable option. EMTS does not

require a direct line of sight to its markers. As a result, its application has surged in various medical fields - especially in image guided interventions that utilize flexible instruments inside the body.

3.1.2.1 Working principle of EMTS

EMTS includes a field generator that produces an ultra-low magnetic field with spatially and temporarily variable field strength (see Figure 3.7). When an electromagnetic sensor coil is placed in this varying magnetic field, a weak but detectable electrical current is generated in the sensor coil according to Faraday's law of electromagnetic induction. Depending on the strength of this induced current, the position and the orientation of the coil is defined within a Cartesian coordinate system defined by the field generator. Modern field generators have six or nine coils in a tetrahedral configuration that allows computing 5 degrees of freedom (DOF) from a single sensor coil (three translational and two rotational) [53]. As the size of this sensor is very small (less than 1 mm), two sensors can be coupled in a non-parallel manner to determine all the 6-DOF (three translational and three rotational).

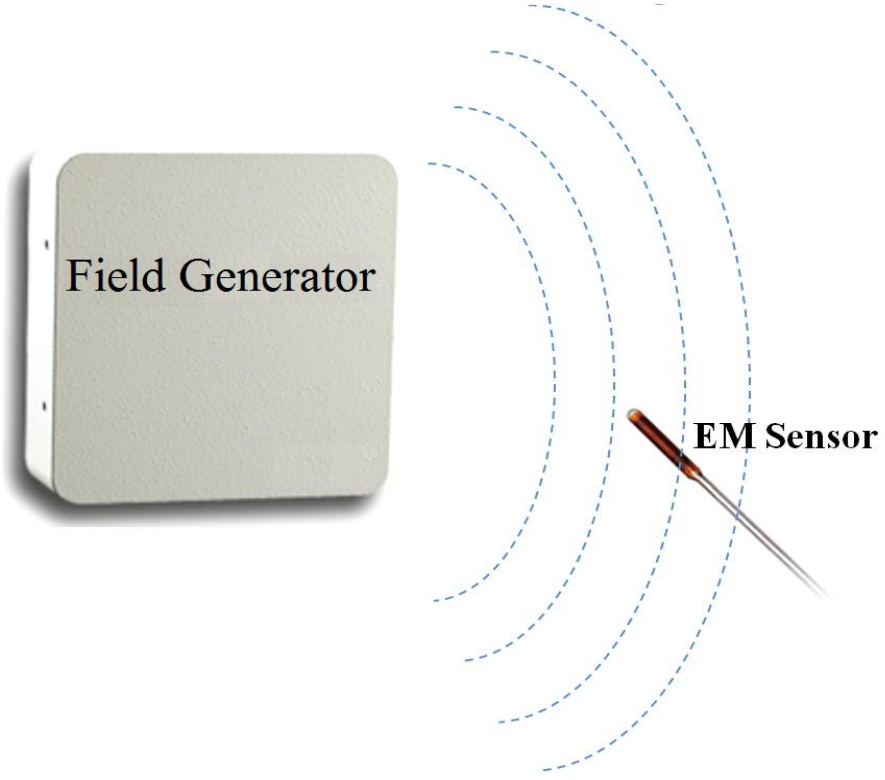

Figure 3.7: EMTS working principle. An EM sensor experiences a spatially and temporarily varying magnetic field, produced by the field generator, that induces a current in it.

3.1.2.2 Classification of EMTS

EMTS can be classified into three categories: alternating current (AC) driven, direct current (DC) driven and passive or transponder systems. As implied by their name, AC-driven systems use AC magnetic fields where inductive sensors measure the variation of the magnetic flux; DC-driven systems use fluxgate sensors in DC magnetic fields [54]. AC-driven EMTS are available from NDI Aurora (Figure 3.8a) and Polhemus Fastrak (Figure 3.8b) while Ascension miniBIRD (Figure 3.8c) offer DC-driven EMTS. Passive or transponder EMTS uses either small permanent magnets or implanted transponders. Tracking is done either by measuring the magnetic field of the magnets or analyzing the emitted signal properties (e.g. intensity, delay or phase shift) from the transponders [55]. For example, Calypso GPS for the body system, from Varian Medical System Inc. (Palo Alto, CA, USA), is a passive transponder based tracking technology (see Figure 3.8d).

3.1.2.3 Procedural steps in image guided intervention using EMTS

Electromagnetic tracking provides real-time tracking (refresh rate 40 Hz) of a variety of surgical tools by integrating miniature-size EM sensors. For instance, in image guided needle interventions, the tip of the needle includes a 5-DOF EM sensor that facilitates tracking the tip in real-time. Typically, the intervention procedure begins with the acquisition of preoperative images with a set of fiducial markers (e.g. skin markers). Then, to perform image-to-patient registration (e.g. fiducial-based registration), a set of fiducial markers in the patient space are chosen by touching with the needle tip and consequently, the corresponding markers are selected in the image space. After the registration step, the tracked needle tip can be represented in the same image coordinate space. Finally, the registration accuracy is verified to confirm successful navigation.

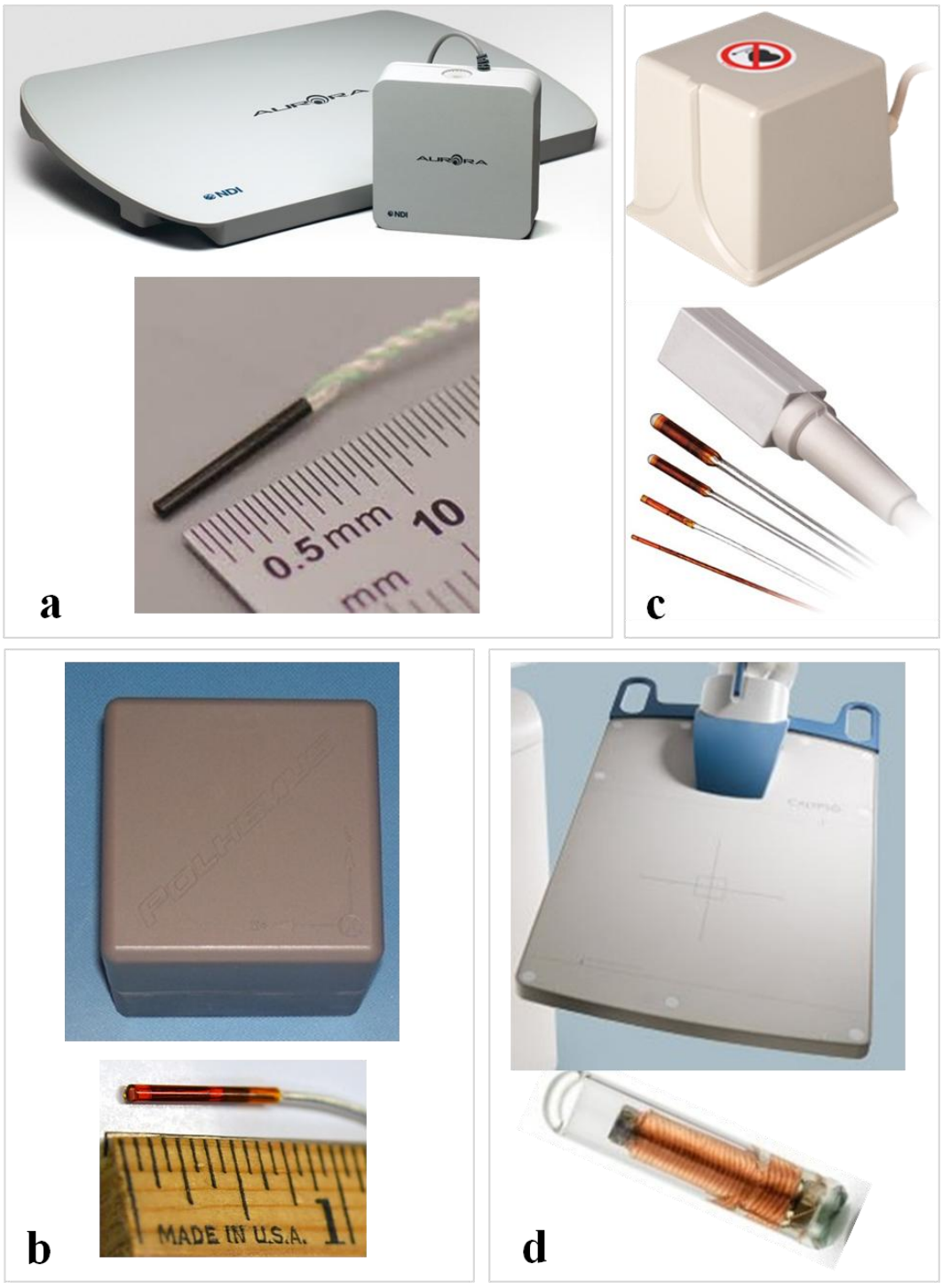

Figure 3.8: Magnetic field generator and sensors of different commercially available EMTS. AC-driven (a) NDI Aurora, (b) Polhemus Fastrak; DC-driven (c) Ascension miniBIRD and (d) passive transponder based "Calypso GPS for the body system" from Varian Medical System Inc. Image source: (a) www.ndigital.com, (b) www.polhemus.com, (c) www.ascension-tech.com, (d) www.varian.com. Used with permission.

3.1.2.4 Studies related to EMTS in IGLI

Integration of a miniature electromagnetic sensor inside a needle tip enables spatial tracking of needles and facilitates needle navigation in various thermal ablation procedures. Generally, in these procedures, preoperative CT, MRI or positron-emitting tomography (PET) images are fused with real-time US images, where EMTS is typically used to localize the needle or the US probe in the fused image space. Percutaneous biopsy and RF ablation in the liver has been performed under CT/US guidance [56, 57] or in combination with PET [58] or MRI [59] guidance using an EM tracking system.

Some clinical studies reported needle tracking accuracy with EM navigation system for biopsy and RFA procedures in the liver and various other organs such as lung, spine and kidney [57, 60]. Krucker et al. achieved a spatial tracking error of 3.8 ± 2.3 mm in a 40-patient clinical trial [57]. In another study, Penzkofer et al. performed twenty-five procedures where the spatial tracking accuracy was 3.1 ± 2.1 mm [56]. The tracking accuracy was sufficient enough to perform the needle intervention successfully during the biopsy and RF ablation.

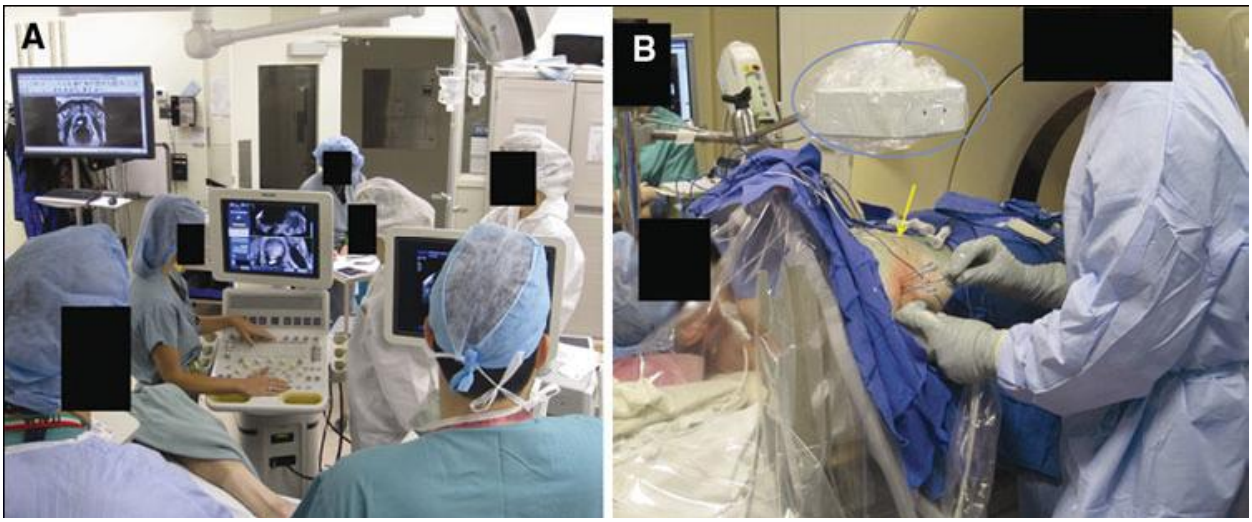

Figure 3.9: (A) A common EM tracking procedure with the tracking workstation and a US machine for prostate biopsies, (B) EM field generator (circled in blue near the top center of image) is placed close to the target and the fiducial patches (yellow arrow in center of image) [61]. Used with permission.

EMTS was also used in guiding the needle tip precisely to the liver tumor without using any conventional real-time imaging modality [62, 63]. The EM system can track a 5 DOF small

sensor embedded in a needle tip. A point-based registration was performed by obtaining the position of the skin fiducial markers, by touching each fiducial with the needle tip, and selecting the corresponding position in the preoperative CT data slices. The experiment was performed on a physiological respiratory liver phantom model containing a motion simulator, and then on a Yorkshire swine's liver where radio-opaque agar nodules were injected as the targeted tumors. However, in order to track the target's motion, a separate reference needle was embedded in the anatomic region of interest [62, 63]. For some laparoscopic RFA studies, a 3D US image was generated from a sweep of 2D US images. The 2D images were obtained from a conventional laparoscopic US probe integrated with an EM navigation system [64, 65]. A similar study was performed for microwave ablation using NDI Aurora EMTS in [66].

In another microwave ablation study, Sindram et al. developed a 3D US guidance system for the open hepatic microwave ablation procedure using a computer-based image guidance system, InVision™ System (InnerOptic Technology, Inc., Hillsborough, NC, USA) [59]. The system was integrated with an NDI infrared OPTS to follow the position of the US handpiece and the ablation antenna in real-time. The guidance system was assessed initially on an agar phantom, followed by an eight-patient pilot trial. However, due to the ablation "line-of-sight" problem, the operators were faced with problems in three out of eight patients, causing difficulty with hand positioning that made the actual task of ablation complex [59]. This limitation was overcome by incorporating an EMTS (e.g. NDI Aurora), the use of which expanded later in the laparoscopic setting [67].

Some other commercial systems based on EM tracking technology were also developed for percutaneous puncture in the liver; for example, US-guided Ultraguide system (Ultraguide Ltd., Yokneam, Israel) [68] and the CT-guided Magellan system (Biosense Webster Inc., Diamond Bar, CA, USA) [69]. However, none of these systems gained popularity, possibly due to the lack of robustness of their EM tracking technology. The *Cappa C-Nav* (Siemens AG, Erlangen, Germany) has been used for needle puncture in the liver [56], but has recently stopped using EM tracking, relying instead on image-based tracking.

3.1.2.5 Advantages of EMTS

The main advantage of EMTS is that unlike OPTS, it does not require a direct line of sight between the field generator and the sensors. Additionally, miniaturization of electromagnetic

sensors (diameters of 5-DOF and 6-DOF sensors are 0.3 and 0.9 mm, respectively) allows them to be easily integrated in tools facilitating tracking of rigid or flexible instruments in minimally invasive applications. Furthermore, EMTS can track more than one sensor (four 6-D or eight 5-D sensors) simultaneously. It is, therefore, possible to reconstruct the shape of flexible instruments (such as catheters or bendable needles) by incorporating a series of sensors inside the tool. Finally, because of their miniature size, EM sensors at the needle tip can be placed close to the target, which lowers the chance of tracking error. In a controlled distortion-free environment the tracking error in EMTS is around 1.2 mm [55].

3.1.2.6 Disadvantages of EMTS

The major limitation of EMTS is its susceptibility to magnetic field distortions induced by any nearby ferromagnetic materials such as a metallic operation table, pacemakers, or any large medical devices (for example, MRI scanners). In such a case, the accuracy may deteriorate dramatically with tracking error up to 7.6 mm [70, 71]. It is, therefore, essential to verify the accuracy of the EMTS before starting a procedure, especially in a new clinical environment that obviously causes a long setup time in clinical practice.

Compared to OTS, EMTS has less tracking accuracy and lower working volume (only 50-70 mm^3). NDI, the principal manufacturer of both EMTS and OTS, has evaluated the accuracy of both systems, particularly of the Polaris optical and Aurora EM tracking systems. According to their study, Aurora EMTS has higher positional accuracy error (1.40 mm) with higher precision error (0.70 mm) compared to Polaris OTS (0.50 mm and 0.25 mm, respectively) [72]. Another technical study compared the same NDI products and found similar results with four times higher positional error in EM tracking than in optical tracking [73].

For more reliable measurements, the field generator of EMTS needs to be placed very close to the patient, thereby reducing the size of the tracking volume. Another factor is the orientation of the EM sensor (whether it is pointing to or away from the field generator) that determines its accuracy. EM sensors are also fragile and more expensive than OTS markers. Frequent usage is not ideal, as these are usually embedded in clinical tools and are tethered by wires to the system control unit.

3.2 MRI guided interventional procedure

MR imaging during interventions are primarily used for target definition due to its high soft-tissue contrast and great resolution enabling excellent visualization of small liver tumors or anatomical structures adjacent to the target tissue even without the use of any contrast medium. Moreover, because of the ability to guide the needle placement using angiographic sequences with freely selectable slice angulations, MRI guided interventions are becoming increasingly attractive. An additional advantage is the precise differentiation between living tumor tissue and tissue with induced coagulation (due to thermal damage). In fact, the entire thermoablative therapy can be planned, guided, and controlled by MRI. But a dynamic, diffusion weighted and contrast MR is needed to diagnose tumors first and then to assess tumor ablation and any viable tumor post RFA application.

3.2.1 MRI guided needle interventions

Depending on the tracking technique, MRI guided needle tracking can be divided into two categories: passive and active. The passive tracking method is the traditional technique. Similar to X-ray guided procedures, MRI is used to guide the needle. Due to the signal void or susceptibility artifacts created by the needle body, the needle appears black in the MR image that makes it identifiable on the image for tracking. As this tracking technique is completely based on the MR imaging system, no hardware or software modification is required. However, tracking information is updated by the temporal frequency of MRI (image acquisition) which is low and does not allow real time tracking. MRI temporal frequency can be increased by sacrificing image resolution but it makes needle tracking problematic due to low contrast of the needle with its surrounding soft tissues. Another limitation of this tracking technique is the requirement of *a priori* knowledge of the needle position to define the MRI scan plane. If the needle deviates from the scan plane due to bending, manual repositioning of the scan plane must be performed, which makes the procedure time consuming. Moreover, the size and appearance of the artifact are greatly affected by MRI sequence parameters and other factors. For example, the orientation of the needle with respect to the MRI main magnetic field determines the artifact's characteristics.

Unlike passive needle visualization methods, active MRI needle tracking is an independent MRI procedure by itself and is separate from the regular MR imaging scheme. Therefore, optimization

of active needle tracking can be performed without affecting the MR imaging scheme. However, modification to the needle and also the MRI system is required for this method. Active needle tracking is based on either the enhancement of the contrast between the needle and its surroundings or by defining the MR scan plane to follow the needle insertion (Table 3.1). In the former method, the needle incorporates a loop wire, through which a weak current is introduced that induces a local distortion of the magnetic field. When the needle is placed in the main magnetic field of the MRI, the homogeneity of the magnetic field is perturbed, thus making the needle appear dark in the image. Though this technique looks similar to the passive tracking method, adjusting the applied current in this approach can control the extent the artifacts. However, *a priori* knowledge of the needle position to define the MR scan plane (i.e. similar to the passive tracking method) is required. Furthermore, the projection image obtained from this wire cannot be used to view the needle because of low contrast between the needle and its surrounding tissues; therefore, typical MR imaging sequences are used in addition. The latter active tracking method defines the MR scan plane using either an external system (e.g. optical stereotactic system) or a micro-RF coil integrated internally into the needle. The working principle of the optical stereotactic system, as well as its pros and cons were discussed in section 3.1.1. From the previous discussion, it is clear that optical stereotactic systems cannot track the tip of a needle while it is bent inside the patient. Furthermore, the coordinate space of the stereo system needs to match the MRI coordinate space by registration, causing inevitable computation as tracking errors.

Table 3.1: Classification of MRI guided needle intervention methods with their advantages (light background) and disadvantages (deep background)

<table>
<tr><th colspan="2">PASSIVE</th><th colspan="3">ACTIVE</th></tr>
<tr><td>Needle visualization based on signal void</td><td>Needle visualization based on susceptibility artifacts</td><td>Tracking depends on contrast enhancement by locally inducing field inhomogeneity</td><td colspan="2">Tracking depends on defining MR scan planes</td></tr>
<tr><td colspan="2"></td><td></td><td>External (optical stereotactic system)</td><td>Internal (micro-RF coil)</td></tr>
<tr><td colspan="2">No hardware/software change required</td><td colspan="3">Independent from MRI imaging scheme, so possible to optimize both procedures separately.</td></tr>
<tr><td colspan="2" rowspan="2">Safe for the patient</td><td rowspan="2">Artifacts are controllable by adjusting the amplitude of the direct current.</td><td colspan="2">Able to define the MRI scan plane continuously to detect the needle, so in real time.</td></tr>
<tr><td>Separate from MR scanner and patient, so safe.</td><td>Able to track the tip inside the patient.</td></tr>
<tr><td>Tracking is not reliable, especially in low MRI signal region.</td><td>Difficult to control the size and visualization of the needle artifact</td><td>To view 3D needle shape needs several projection images with different angles, so time consuming</td><td>Registration of external tracking system to MR scanner is a must</td><td>MR scan plane can be updated based on the tip position, however needle shape is unknown.</td></tr>
<tr><td colspan="2">Difficult to visualize the device when in conflict with soft tissue contrast</td><td>Difficult to visualize the needle and the anatomy when the contrast is low</td><td>There is some obvious registration computation error</td><td rowspan="2">Mutual inductance among the coils, those are close to each other, degrades their performance.</td></tr>
<tr><td colspan="2">Requires a priori knowledge of the device position for MR scan plane</td><td>Requires a priori knowledge of the device position for MR scan plane</td><td>Cannot track the internal part of the needle inside the patient</td></tr>
<tr><td colspan="2">Manual repositioning required to track bending needle, time consuming</td><td colspan="3" rowspan="2">Hardware and software modification is often required.</td></tr>
<tr><td colspan="2">Depends on the MRI image frequency, so not suitable for real-time tracking</td></tr>
</table>

Alternatively, a micro-RF coil (similar to EM sensor) can be integrated into the needle tip and followed in MR scanner space directly without doing any coordinate space registration. As a result, it is possible to update the MR scan plane according to the tip position. Nevertheless, the actual orientation of the entire needle is unknown, which is crucial for navigation. One option could be to follow a pre-defined path computed from preoperative images, but that would not be reliable due to the deformation of the liver. Integrating multiple micro-RF coils along the needle to calculate the tip and orientation could be an option. However, it is challenging since mutual inductance between the coils that are close to each other degrades their performance. Finally, electrically conductive leads entering a patient's body cause excessive heating, resulting in burn injuries to patients undergoing MR procedures which is a major patient safety concern.

Alternatively, optical sensing is a more recent technology that can be applied to "sense" the tip and orientation of a needle. This thesis work investigates the potential of optical sensing to allow active MR needle tracking so that intraoperative needle tracking is possible under simultaneous MR image guidance. In the next section, we will discuss the fundamentals of optical sensing technology.

3.3 Optical sensing technology

The foundation of optical sensing technology is the optical fiber - a flexible, thin and transparent strand of silica glass. Optical fibers typically include a transparent core encircled by a transparent cladding that in turn is surrounded by a buffer coating (see Figure 3.10).

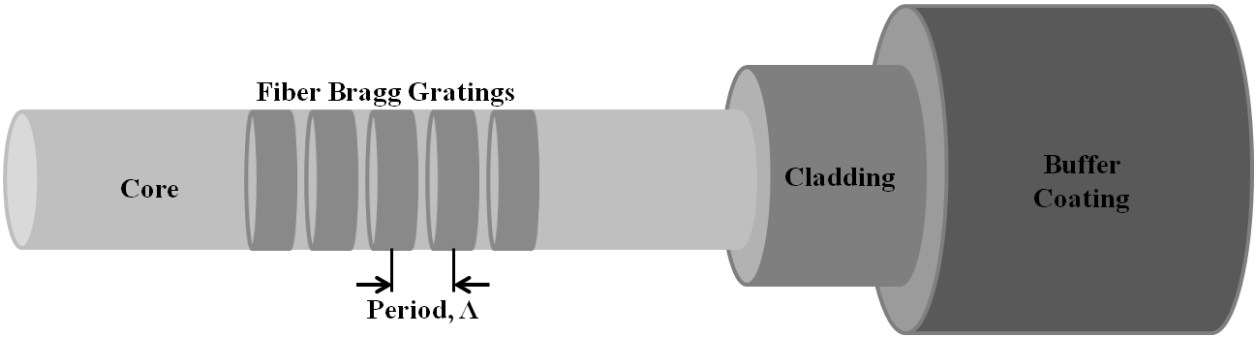

Figure 3.10: A fiber optic cable containing fiber Bragg gratings.

The refractive index of the inner core, n_{core} is higher than the refractive index of the outer cladding, n_{clad}. When light is transmitted from the core to the cladding with an angle greater than

the critical angle, it causes total internal reflection at the core-cladding interface and keeps the propagating light within the core. The outermost buffer coating ensures protection of the fiber from the external environment and physical damage.

3.3.1 Fiber Bragg Gratings

Due to the photosensitivity of optical fibers, the core refraction index in an optical fiber is altered by optical absorption of ultraviolet (UV) light. This allows the fabrication of periodic modulation of the refractive index directly into the fiber core, called a Fiber Bragg Grating (FBG). When a broad-spectrum light beam is passed through to an FBG, light reflection occurs at each change of refractive index. As a result, multiple reflections of the light happen from the repeated modulation of the refractive index. At one specific wavelength (called Bragg wavelength), all the reflected signals are in phase and interferes constructively to form a back reflected signal to the input end. Light reflections occurring at other wavelengths are out of phase, interfere destructively, so cancel out each other and as a result are transmitted through the grating. Therefore, FBG reflects one specific wavelength and transmits all others (as shown in Figure 3.11).

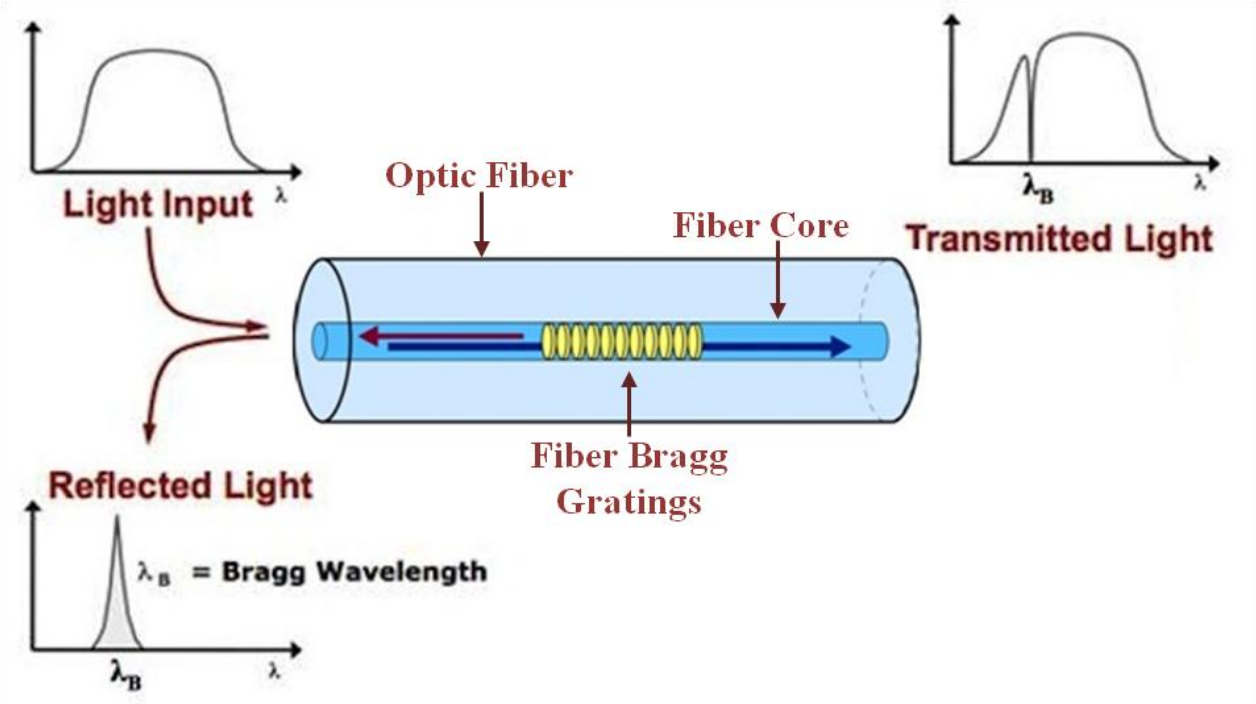

Figure 3.11: Principle of fiber Bragg grating sensor [74]. Used with permission.

The Bragg wavelength, λ_B is defined as follows [75]:

$$\lambda_B = 2n_{eff}\Lambda \quad \text{(Eq. 3.1)}$$

where n_{eff} is the effective refractive index and Λ is the period of the gratings. When the period of the grating is altered, because of strain or temperature change, the reflected wavelength shifts accordingly (Eq. 3.1), which allows the FBG to act as an optical sensor to measure a wide variety of parameters, for instance, strain, force, pressure, temperature [76].

3.3.2 Application of FBG sensors in the medical field

FBGs are small in size (around 5 mm), immune to electromagnetic interference and have the ability to sense submicron strain. They can be read at high sampling rates (>20 kHz), which is sufficient for real-time tracking. These characteristics inspired a wealth of research in various medical domains. For example, FBGs have been used for studying the biomechanical behavior of the musculoskeletal system, pressure mapping in different orthopedic joints, pressure distribution at the intervertebral disc, dental biomechanics, chest wall deformation during respiration, and various human-machine interfaces [76]. Due to their immunity to electromagnetic interference, FBG sensors are considered a suitable technology to use safely in a high electromagnetic field such as in an MRI suite. As a result, applications such as temperature measurement of the patient under MRI-guided hyperthermia have exploited FBG sensors [77]. In addition, sensors have also been integrated into surgical tools to measure forces in minimally invasive surgeries, such as in retinal microsurgery, surgical knots and robotic surgery [77]. The shape estimation of catheters and endoscopes using FBG sensors has also been proposed.

3.3.3 Shape sensing

One of the advantages of FBG is that it supports optical multiplexing that facilitates the integration of more than one FBG sensor in a single fiber and reading each of them. Hence, a series of FBG sensors can be placed along a single fiber and then integrated into flexible surgical devices such as needles. Recently, FBGs have been applied on biopsy needles, catheters and other minimally invasive tools for shape detection and force sensing (e.g. to develop exoskeletal robot fingers) [78, 79]. In general, three fibers each with a number of FBGs are glued together to

form an equilateral triangle (on transversal plan) and then placed along the device, as shown in Figure 3.12. A broadband light source is transmitted through the fibers. When the device bends, the fibers also bend. Depending on the bending magnitude and the direction, compression or expansion of the FBG sensors occur. Therefore, the period of the grating changes which causes the reflected wavelength to shift forward or backward. The amount of the wavelength shift directly depends on the amount of the changes in the period of gratings. We describe the working principle of shape sensing in Figure 3.12.

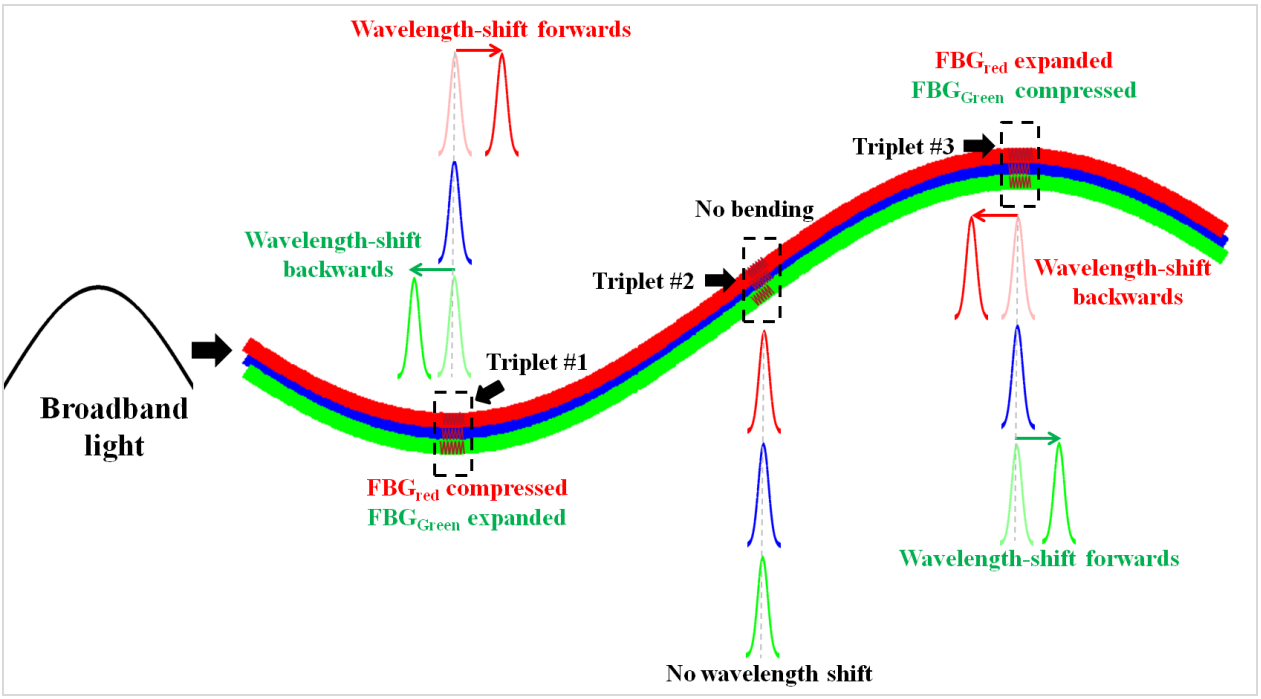

Figure 3.12: Application principle of FBG sensors for shape sensing in minimally invasive surgical tools.

We represent the three fibers with three different colors - red, green and blue. There are three sensors in each fiber and the sensors are aligned therefore, the cross section of this active area contains three FBG sensors. We call this active area a "triplet". In the first active area (i.e. triplet #1), the FBG in the green fiber is expanded, that (let us assume) causes the reflected wavelength shift in the backward direction. The FBG in the blue fiber does not have any bending effect, so its reflected wavelength position is unmoved. However, the FBG in the red fiber is compressed which shifts the reflected wavelength in the forward direction. On the other side, we are assuming a similar amount of bending in triplet #3 as in triplet #1 but in the opposite direction. As a result, the reflected wavelength shift happens in the forward and backward directions for the FBG in the

green and red fibers, respectively. As there is no strain in triplet #2, the reflected wavelength for all the three FBG sensors is unchanged. Now, based on the wavelength-shift of the three FBG sensors in a triplet, it is possible to calculate the strain and hence, estimate the curvature radius and the orientation at that position. Once the curvature information is available at the active regions (i.e. triplets), the entire shape can be reconstructed using an interpolation method.

Recently, using FBG-based shape sensing technology to design minimally invasive surgical tools has attracted the attention of researchers. Abayazid et al. [80] used a Nitinol alloy-based flexible needle, having a length of 185 mm and diameter of 1 mm with a beveled tip of 30°. The needle included FBG sensors at four different locations, each location containing three sensors.

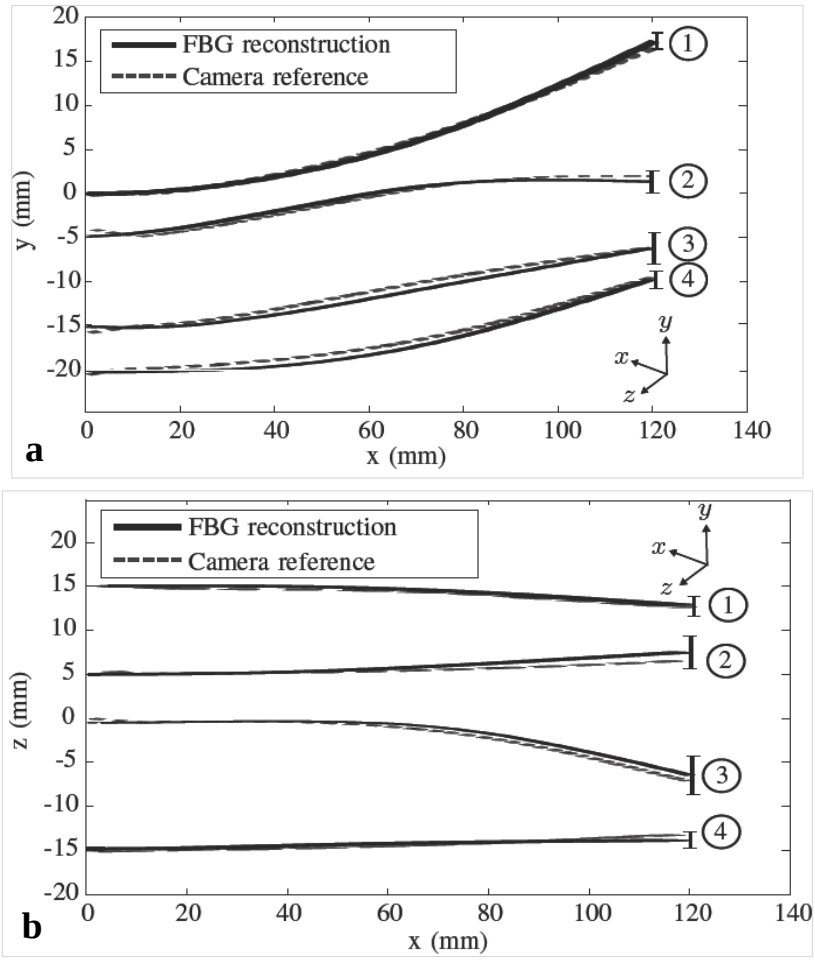

Figure 3.13: Reconstructed needle shape while the needle was inserted into a soft-tissue phantom, (a) top view and (b) side view. Mean tip error for (1) single bend (error 1.5±0.8 mm), (2) double bend (error 2.0±0.7 mm), (3) 3D double bend (error 2.1±1.1 mm) and (4) drilling insertions (error 1.7±1.2 mm) [80]. Used with permission.

A gelatin-based soft-tissue mimicking phantom was used for the experiment. While the needle was inserted into the phantom, the 3D shape of the needle was reconstructed using the FBG sensor data. Their reconstructed needle shape was compared with the images obtained from the two cameras. We measured a mean tip accuracy of 1.3 mm for 110 mm insertion and 1.8 mm for 120 mm insertion (see Figure 3.14).

Park et al. [81] inscribed three fibers with a 120° configuration on the inner stylet of an 18G-150 mm MRI compatible biopsy needle. Each fiber with a diameter of 250 μm, contained two FBGs at 22 mm and 85 mm distance from the base of the needle. They measured tip deflection in two orthogonal planes (*xy* and *yz*) around the needle axis. For actual tip deflection of ±15 mm, the root mean square (RMS) errors for the estimated tip position were 0.38 mm and 0.28 mm in *xy* and *xz* planes, respectively.

In another needle shape reconstruction study, Henken et al. estimated the tip position of an 18G-200 mm long needle. Each of the three fibers contained two FBGs at 56 mm and 126 mm from the needle base. A mean accuracy of 0.89 mm (std 0.42 mm) and 1.32 mm (std 0.48 mm) was obtained during deflection of the needle tip up to 12.5 mm [82]. In their subsequent work [83], they investigated the suitability of FBG-based shape sensing for robotic needle steering by simulating extensive error analysis to quantify the accuracy of the needle tip tracking.

Reza et al. [84] studied real-time 3D shape needle tracking using FBG sensors for teleoperated beveled-tip needle steering under MRI guidance. Three fibers were embedded in a similar fashion like the previous methods into a 110 mm long and 0.6 mm inner stylet of a 20G MRI-compatible biopsy needle. Three FBGs were included in each fiber. The minimum number of sensors and their optimal positions in the fibers were studied to keep the needle tip tracking error below 0.5 mm for various amounts of needle insertion depth. Finally, the reconstructed needle shape was visualized in 3D slicer, which is a free open-source software application for medical image computing.

Moore *et al.* [85] presented a shape sensing method by transforming distributed curvature data into a 3D shape by applying elastic rod theory. Their method could be used to estimate the shape and location of fiber a such as a catheter in 3D. However, their experimental results show an error or 7.2%, most likely due to the twisting of the fiber which was not considered in their method [85].

Lee *et al.* [86] developed 3D shape sensing using femtosecond laser direct-written Bragg grating. Unlike all the previous methods their sensor configuration did not maintain a 120° angular difference between FBG sensors. One waveguide was written at the center of the coreless fiber and two additional waveguides were written with a slight offset and parallel with the center waveguide. The authors proposed to use the center waveguide, positioned in the fiber's neutral axis, for temperature compensation as it should be naturally insensitive to bend-induced strain due to its position. Figure 3.15 shows their reconstructed 3D fiber shape for four different shapes, including the unstrained straight fiber position (black color).

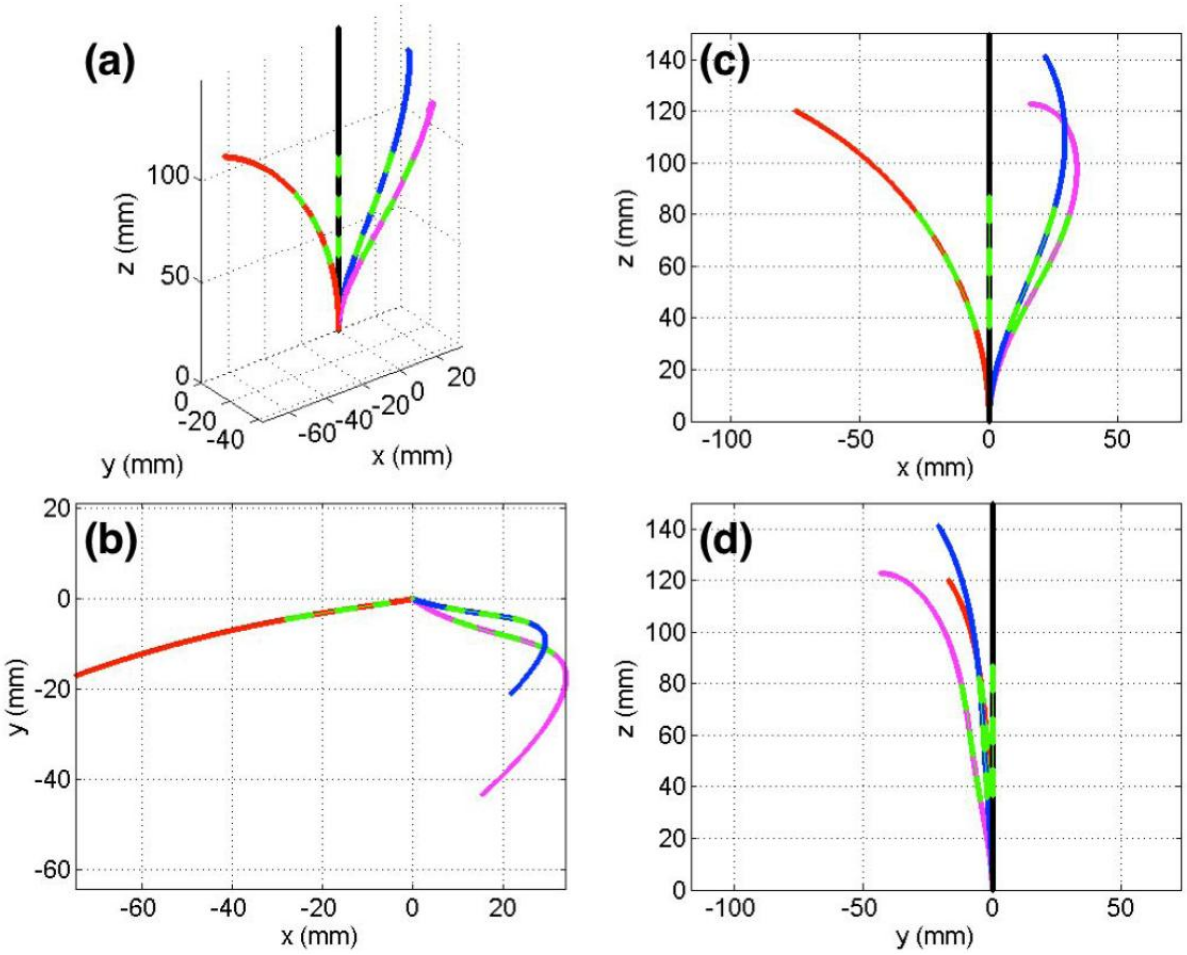

Figure 3.14: 3D Plot of four different fiber shapes, (a) 3D view of the fiber shapes and three corresponding orthogonal views, (b) x-y, (c) x-z, and (d) y-z [86]. The green line segments indicate Bragg gratings locations. Used with permission.

Another study [87] mainly focused on simulation work to optimize shape sensing. In this study, the author developed a simulation tool that can calculate the strain value of the FBGs for a given shape. Their simulation tool also showed the reconstructed shape from the strain data.

3.4 Summary

Tracking systems are a key component in IGLI, enabling real-time navigation of a needle during insertion. Optical and electromagnetic tracking systems are the most commonly used systems both in research and clinical settings. However, OTS are not feasible for tracking needle bending inside the body and EMTS are not compatible in or near an MR magnet. Therefore, a new tracking system that can be easily and reliably integrated into an MRI environment, without breaking the clinical workflow, is necessary. FBG sensors have shown huge potential in a limited amount of medical applications due to their unique advantages such as-small size, high sampling rate, immunity to electromagnetic interference and multiplexing capability. It is evident from the literature review that the application of FBG sensors in medical device tracking through shape sensing has great potential. This technique can have a strong impact on a number of MR compatible procedures.

CHAPTER 4 METHODOLOGY

This chapter begins with a complete description of the experimental setup used to design and track an interventional needle with shape sensing. The needle fabrication and FBG calibration processes are explained, followed by a description of the methodology to reconstruct the shape of the needle in 3D. The representation of the reconstructed 3D needle model and the incorporation of that model in the preoperative MRI image space are then described. The different steps to generate various synthetic phantoms, such as planar and gel phantoms are also demonstrated. Finally, a validation scheme to assess the overall tracking accuracy of our FBG-based technique is shown.

4.1 Experimental setup

Our experimental setup and its individual components are shown in Figure 4.1. Three linear stage motors (PM500 stage, Newport Corporation, CA, USA), two arranged for horizontal movements (side to side and front to back) and one for vertical movements (Figure 4.1c), were used to displace the needle in three different axes. These three motors were assembled and the needle was fixed on the topmost motor. A calibration plate (Figure 4.1b) having a series of integrated grooves along its edges was used for the calibration procedure. This calibration was to establish the relationship between the strain at the sensor locations and the measured wavelength-shift values measured from those sensors directly. Contiguous grooves on the calibration phantom, spaced at 1.4 mm, were used to hold the tip of the needle at fixed positions during measurement. The other end of the needle (i.e. the base) was fixed with a strong spring metal alligator clip. The fabricated fibers (illustrated in section 4.2) were placed inside a needle and were clamped near the base of the needle to restrict any unwanted rotation or twist. The fibers were connected to an interrogator (Deminsys© Python 850-55 interrogator, Technobis, Uitgeest, Netherlands), which in turn was linked to a computer by an Ethernet connector. Deminsys© Python has four channels and each channel typically supports eight sensors for the interrogation of signals up to 20kHz. In our setup, the acquisition data from the interrogator were transferred to the computer using the UDP-protocol. In addition, two linear manual stages (Figure 4.1d) were used to adjust the position of the calibration phantom in both xy and xz planes during the calibration process. Two

cameras (Figure 4.1e and 4.1f) were incorporated to capture the top and side views of the needle simultaneously during the experiment.

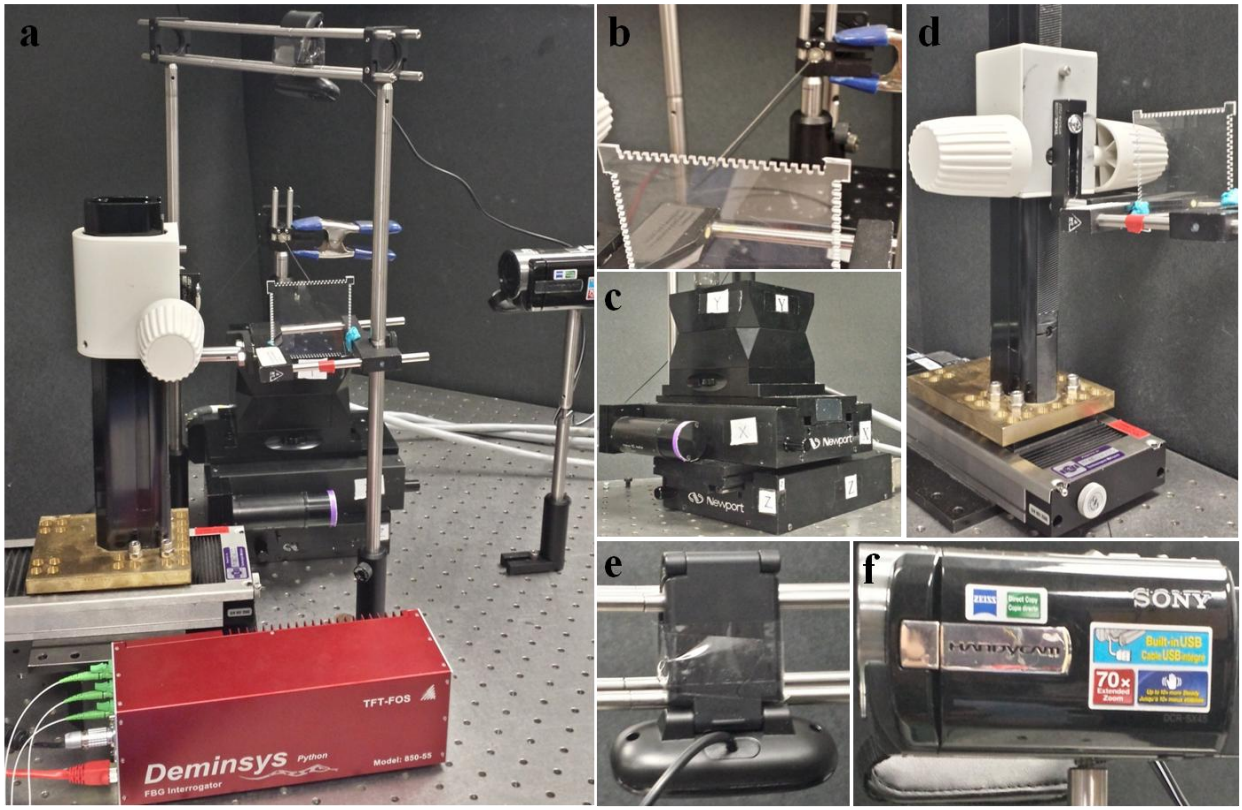

Figure 4.1: (a) The complete experimental setup of our FBG-based tracking system, (b) calibration plate holding the needle tip inside a groove, (c) three Newport PM500 linear stages, (d) two manual linear stages, (e) camera-1 and (f) camera-2.

4.2 Needle fabrication

The proposed needle integrates FBG sensors made by a periodical modification of the fiber's refractive index, giving an increase in reflection for a specific wavelength. When strain is applied along the fiber axis, the period of the grating is changed, leading to a frequency shift in the reflected wavelength. It is thus possible to build a 3D shape reconstruction system, modeling the fiber in 3D space using several triplets, each made of three FBG sensors separated by 120° as shown in Figure 4.2. This will be explained in the following sections.

The typical setup uses a broadband laser source to guide light in the fibers. When the fiber bends (for example, at triplet #3 as shown in Figure 4.2), FBG sensors are either stretched or

compressed, leading to a shift in their reflection spectrum toward longer or smaller wavelengths, respectively.

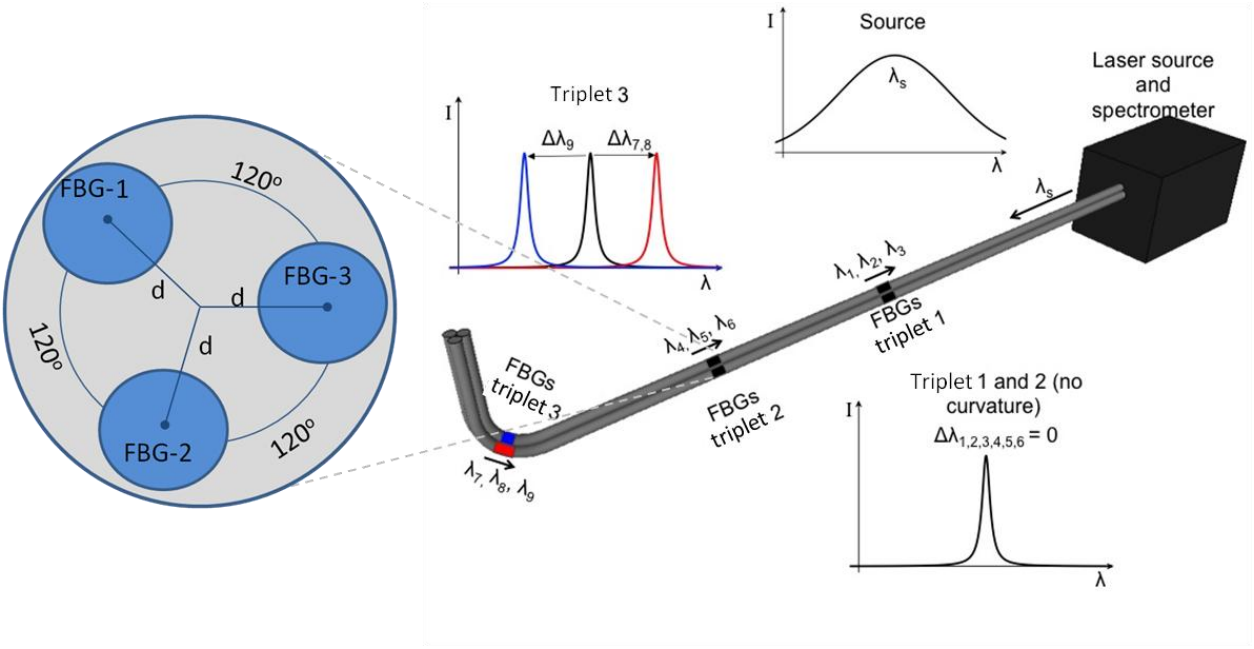

Figure 4.2: 3D shape reconstruction of a needle using the shape sensing technique where bending is characterized by the wavelength shift. The left side of the Figure shows the orientation of three FBGs at one triplet. The shift of the wavelengths λ_7, λ_8, λ_9 occurs due to the bending at triplet #3, while the wavelengths λ_1...λ_6 remain fixed as no bending takes place at triplets #1 and #2 [88].

If there is no bending in the sensing area (e.g. at the locations of triplets #1 and #2), the reflection spectrum of all FBG sensors remains unchanged. A spectrometer is connected to the fibers to analyze the reflection spectrum of all the nine FBGs in real-time. Knowing the magnitude of the spectra's shift, the curvature radius and the orientation of the fibers triplet can be deduced easily. Finally, interpolation is applied on the curvature and its directional data is used to estimate the entire 3D shape along with the tip position.

In our system, three fibers were glued together and integrated into a 150 mm long needle with a 0.603 mm inner diameter (20G Kimberly-Clark Chiba Spinal Needle), as shown in Figure 4.3. The diameter of each fiber was 125 μm and the distance between each fiber core to the center of the fiber triplet was ~72.17 μm (i.e. 125/√3). Therefore, the outer diameter of a fiber triplet prior to gluing was ~134.67 μm (i.e. 72.17+125/2).

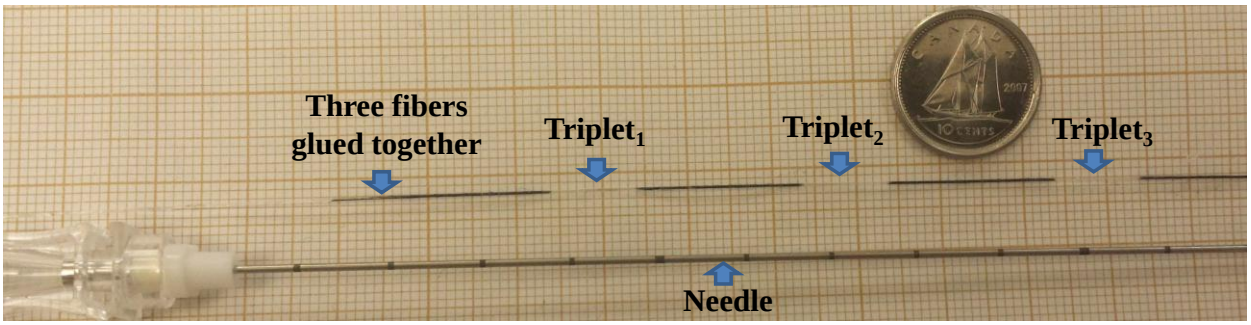

Figure 4.3: Image shows a 20G Spinal needle and three fibers glued together. Each fiber includes three FBGs triplets.

We requested the Advanced Photonics Concepts Laboratory (APCL) of Polytechnique Montreal, Montreal, Canada for fabricating three fibers and glueing them according to our desired specification. This lab fabricated FBGs in optical fibers and glued them together using UV curing glue maintaining an angular distance of 120° between each other as shown in Figure 4.4. Each fiber contained three FBGs located at 35 mm, 75 mm and 115 mm distance from the needle base where the Bragg wavelengths are (~843.3, ~847.8, ~854.3 nm), (~844.1, ~847.7, ~853.9 nm) and (~844.6, ~847.9, ~853.8 nm), respectively. Figure 4.4 shows the configuration of the fibers with FBGs inside the needle. All the three fibers were connected to the Deminsys© Python interrogator through three individual channels.

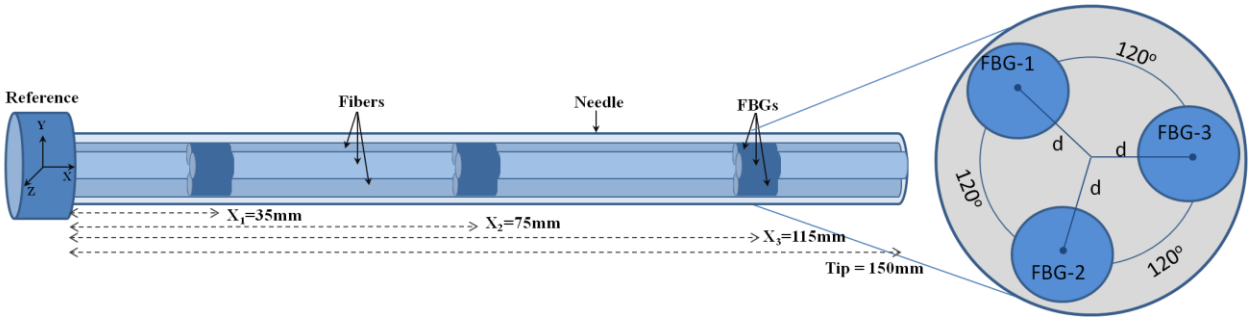

Figure 4.4: A FBG-based needle with three optical fibers having a 120° configuration. Each fiber has 3 FBGs placed at three different locations (35, 75 and 115 mm) along the needle shaft.

4.3 Acquiring sensor data from the Deminsys© interrogator

In order to transmit the sensor data directly from the Deminsys© interrogator to a local computer, we proceeded with the manufacturer's instructions as follows. First, a connection was made between the computer and the Deminsys system using an Ethernet connector and then by

selecting the proper Internet protocol (IP) address from the properties of the Ethernet connection of that computer. This enabled us to communicate with the Deminsys system from the computer through a web server. We then turned on three superluminescent LEDs (SLEDs) in the interrogator. These three SLEDs sent high power density light through the three fibers connected to the interrogator by three individual channels.

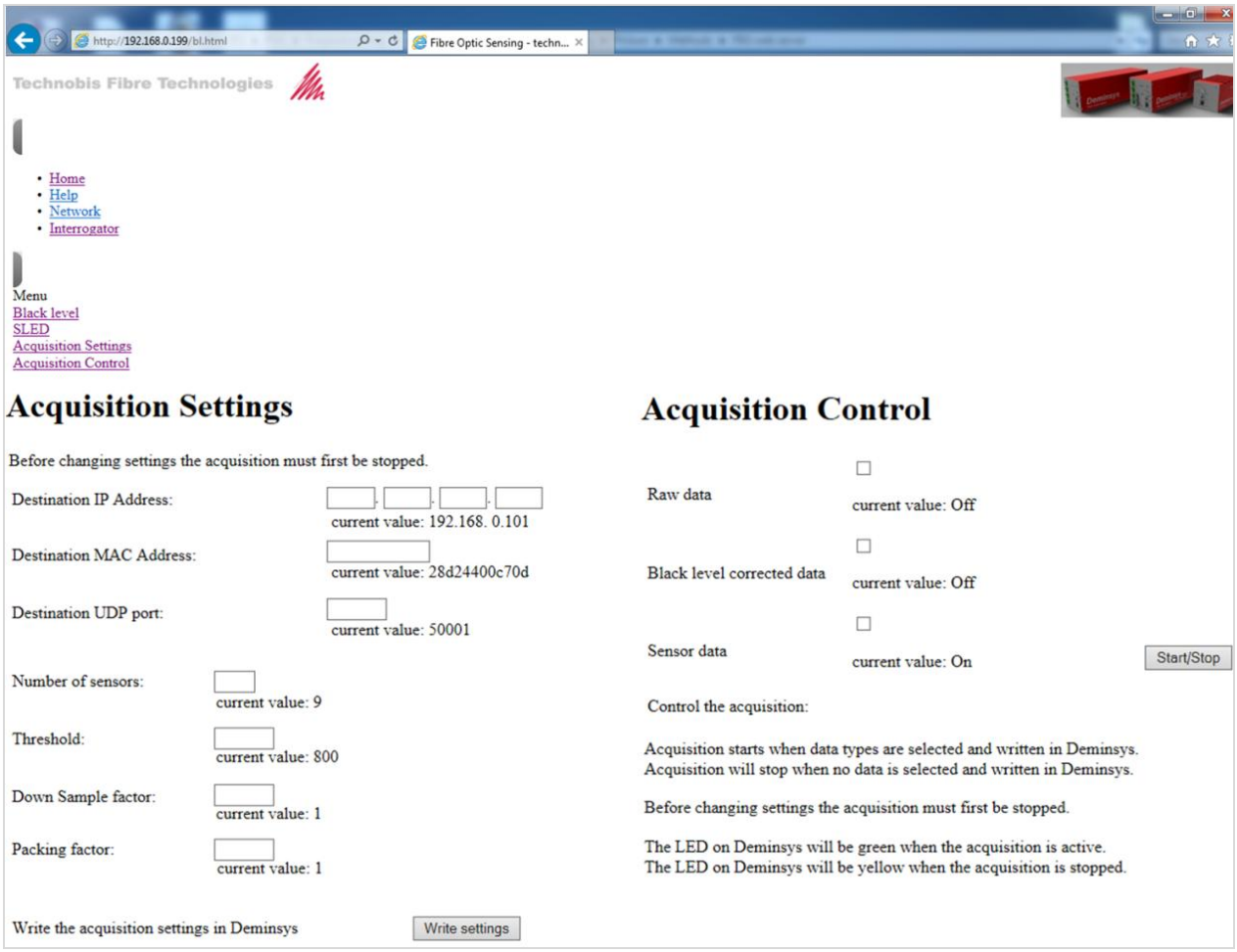

Figure 4.5: Web server showing the acquisition settings and acquisition control interface.

Once the SLEDs were activated, we also set the acquisition parameters such as: (i) the total number of FBG sensors (i.e. 9 in our setup), (ii) the threshold value to detect the sensor signals that depends on the quality of the used FBG sensors and their reflected light intensity (i.e. 800 for our FBG sensors), (iii) the downsampling factor (i.e. 1 in our setup) that defines the sample-rate as the acquisition data appears at the host and (iv) the packing factor (i.e. 1 in our setup) that allows the UDP data payload to be sent in a more bandwidth effective manner, as shown in Figure 4.5. Once all the acquisition parameter values were assigned through the web server

interface, we started the acquisition by selecting the sensor data option in the acquisition control interface.

The interrogator continuously sends the sensor data to the computer as a series of UDP payload packets. It is crucial to understand the structure of the UDP packet payload in order to extract the specific information related to the wavelength data. The structure of the payload has four main sections, as shown in Figure 4.6. "Protocol_ID" is the first section providing the protocol version number. The second section is "Generic_Section" giving the general information about the interrogator such as the version, type and identifying number of the interrogator. The specific data format, which is defined in the packet is indicated by "Data_Protocol_ID". Finally, the last section "Data_Section" contains the sync input and the sensor data. As we were interested in the sensor data, we skipped the first three sections and parsed the sensor data. To do that, we had to develop an application in Matlab to acquire UDP packets and extract the wavelength data from each packet.

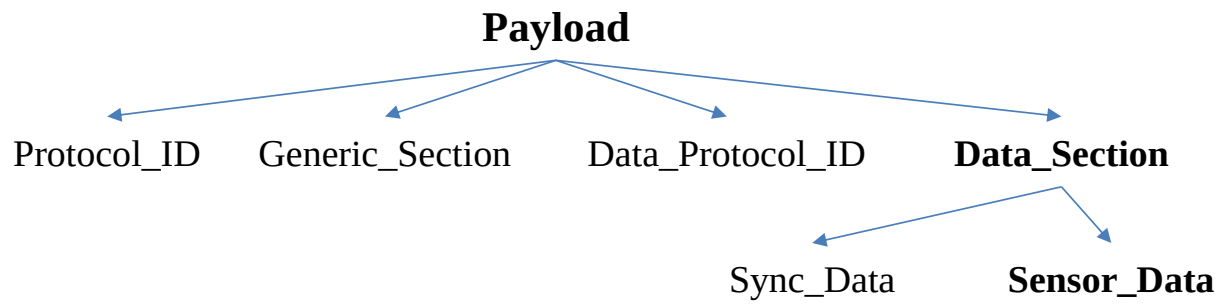

Figure 4.6: The overall structure of a UDP packet payload provided by the Deminsys interrogator.

4.4 Calibration procedure

From the Deminsys© interrogator, the wavelength data of the three FBG sensors in a triplet location was retrieved. The strain value at a triplet location of the needle was estimated by performing a calibration procedure. From this strain value it is possible to calculate the curvature at that triplet location. The proposed calibration procedure for the needle determines the strain value at each FBG sensor location along the needle according to the observed wavelength shift values of the corresponding sensor. The calibration matrix at a location x_l along the needle is defined in Eq. 4.1, where $\varepsilon_{xy}(x_l)$ and $\varepsilon_{xz}(x_l)$ represents the strain in xy and xz planes,

respectively, $\Delta\lambda_{fbg} = \{1,2,3\}$ represents the wavelength-shift and C_i values of the calibration matrix:

$$\begin{bmatrix} \Delta\lambda_1 \\ \Delta\lambda_2 \\ \Delta\lambda_3 \end{bmatrix} = \begin{bmatrix} C_1(xy) & C_1(xz) \\ C_2(xy) & C_2(xz) \\ C_3(xy) & C_3(xz) \end{bmatrix}_{x_l} \begin{bmatrix} \varepsilon_{xy} \\ \varepsilon_{xz} \end{bmatrix}_{x_l} \quad \text{(Eq. 4.1)}$$

According to [74], we can define the strain, $\varepsilon_{xy}(x_l)$ at location x_l in *y*-direction (similarly, in *z*-direction) as a function of x_l:

$$\varepsilon_{xy}(x_l) = \frac{3 \cdot d \cdot y(L) \cdot x_l}{L^3} \quad \text{(Eq. 4.2)}$$

where, d is the distance between the fiber center and the needle center and L is the needle length. We calculated $\varepsilon_{xy}(x_l)$ for different known deflections $y(L)$ = (1.4,2.8,...,14 mm) of the needle tip by placing the tip in the grooves of the calibration phantom (as shown in Figure 4.7), and simultaneously retrieving the corresponding wavelength shift $\Delta\lambda_{fbg}$ from the Deminsys© interrogator.

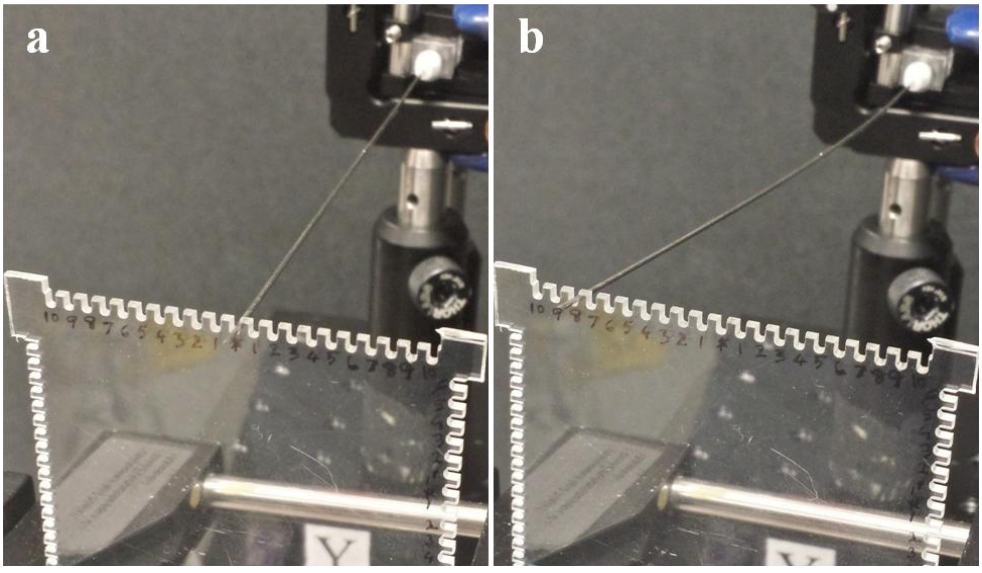

Figure 4.7: During the calibration procedure, the needle tip is stabilized inside the grooves (a) without bending and (b) with bending for a known amount of displacement of the needle tip. The distance between the successive grooves was 1.4 mm.

Finally, the calibration matrix component $C_{fbg}(xy)$ was found as the slope of the fitting line between $\varepsilon_{xy}(x_l)$ and $\Delta\lambda_{fbg}$ using the least square method. Similarly, we computed $C_{fbg}(xz)$ for the *xz* plane.

4.5 Needle shape reconstruction

Once the calibration matrix was calculated, its inverse matrix was multiplied with the shifted wavelengths of the FBGs in a triplet in order to generate the strain values at each triplet location. Assuming the needle behaves as a cylindrical rod under pure bending, we can get the curvature from the strain as follows:

$$y'' = \varepsilon_{xy} / d \qquad \text{(Eq. 4.3)}$$

where d is the distance from the fiber center to the core of the needle. Considering our needle configuration, the second derivatives at four different locations (three FBGs positions and the tip where the strain was zero) were known. Therefore, it was possible to fit a third order polynomial along the needle as follows:

$$y''(x_l) = A_y {x_l}^3 + B_y {x_l}^2 + C_y x_l + D_y \qquad \text{(Eq. 4.4)}$$

Polynomial coefficients (A_y, B_y, C_y, D_y) were calculated by solving the following system of equations:

$$\begin{bmatrix} A_y \\ B_y \\ C_y \\ D_y \end{bmatrix} = \begin{bmatrix} x_1^3 & x_1^2 & x_1 & 1 \\ x_2^3 & x_2^2 & x_2 & 1 \\ x_3^3 & x_3^2 & x_3 & 1 \\ L^3 & L^2 & L & 1 \end{bmatrix}^{-1} \begin{bmatrix} y''(x_1) \\ y''(x_2) \\ y''(x_3) \\ 1 \end{bmatrix} \qquad \text{(Eq. 4.5)}$$

The approximated needle profile was obtained by performing a double-integration of Eq. 4.4, so that *y* coordinates along the needle were given as follows:

$$y_{Approx}(x_l) = \frac{A_y}{20} x_l^5 + \frac{B_y}{12} x_l^4 + \frac{C_y}{6} x_l^3 + \frac{D_y}{2} x_l^2 \qquad \text{(Eq. 4.6)}$$

The same procedure was used to find $z_{Approx}(x_l)$.

4.6 Navigation software

Once the shape of the needle is reconstructed, it is represented in the coordinate system of the FBG interrogator. However, it is not enough to simply infer the 3D shape of a needle in real-time and view the shape in an arbitrary space. For real-time image-based navigation, the reconstructed needle shape needs to be superimposed on the preoperative image space. Towards this end, a fiducial-based registration was performed in order to align the FBG-based tracking space with the preoperative image space from a CT or MRI.

4.6.1 Real-time visualization of needle profile

For real-time visualization, the following procedure was employed, which required the development of a number of software tools to streamline the process prior to needle guidance. To begin with, as previously stated, a function was developed in MATLAB (R2013b) in order to process the raw UDP packets acquired from the interrogator to extract the wavelength data. The calibration matrix between the shifted wavelength and the strain was generated (according to section 4.2) and stored locally on a PC, which was used later for rendering the needle profile in real-time (as described in section 4.3). The estimated needle profile values in MATLAB were transferred to 3D Slicer for navigation. 3D Slicer (Slicer) is free and open source software that can be easily configured to one's own application. We developed a module and integrated that into Slicer for visualizing the needle shape. The connection between MATLAB and Slicer was possible using the OpenIGTLink library, another free open-source library for communication among devices and software. The whole data flow from the FBG data acquisition to the shape sensing visualization in real-time is shown in Figure 4.8.

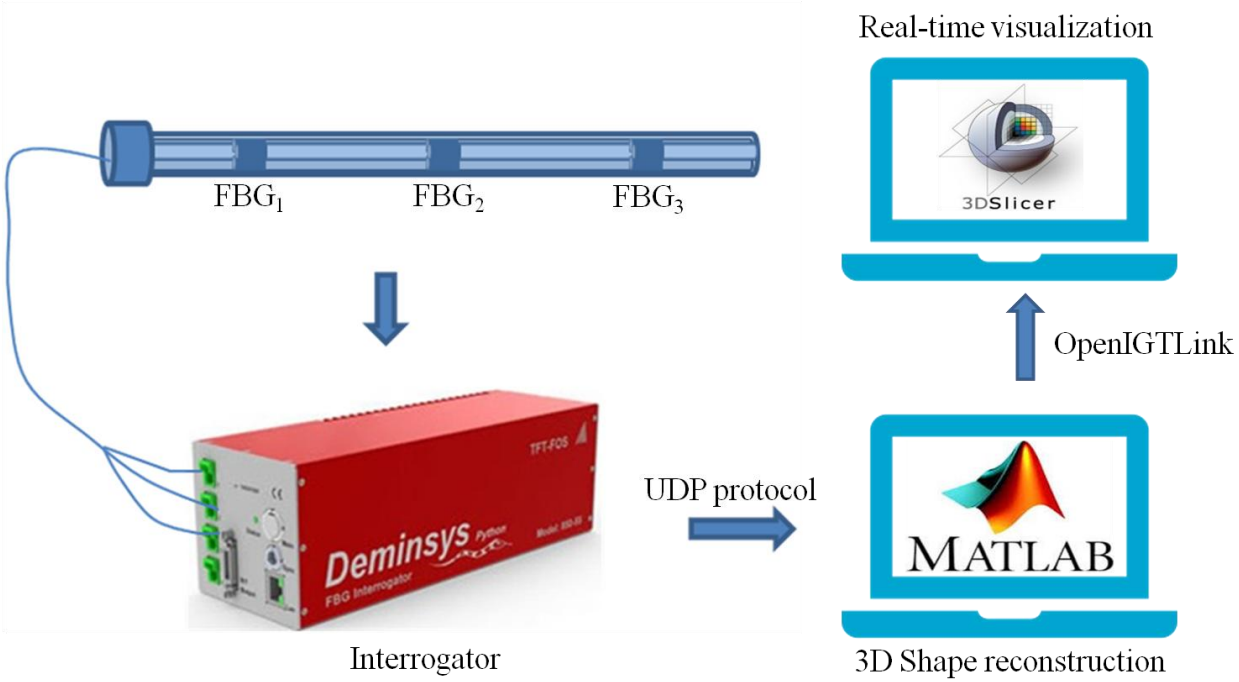

Figure 4.8: Data flow from FBG data acquisition to visualization of shape sensing in real-time.

4.6.2 3D Model generation

We created various calibration objects and planar phantoms for validation purposes. In addition, a gel phantom containing different tube orientations was made for the in-vitro experiments.

4.6.2.1 Planar phantoms

In order to fabricate the planar phantom, a 3D model of the phantom was initially designed in SketchUp (www.sketchup.com), a free 3D modeling computer program. Later, the model was loaded into a CNC milling machine for the fabrication. The models had a series of grooves just big enough to hold the needle tip tightly. The calibration phantom was made of acrylic glass with grooves spaced 1.4 mm apart (Figure 4.9(a)), while a copper metal based phantom having grooves spaced at 2.67 mm ((i.e. phantom-1 as shown in Figure 4.9(b)) was fabricated to validate the needle tip accuracy of our FBG-based tracking system.

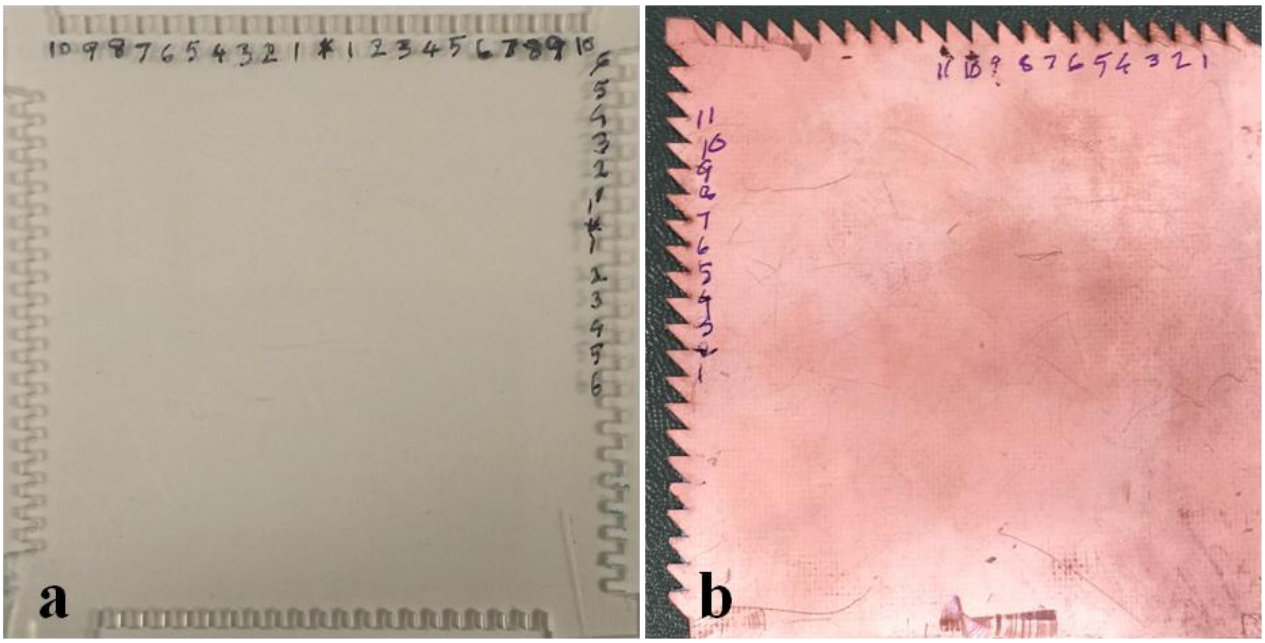

Figure 4.9: Fabricated planar phantoms, (a) calibration phantom, and (b) validation phantom.

4.6.2.2 Anatomical gel phantom

The gel phantom consisted of four transparent silica tubes and polydimethylsiloxane (PDMS) elastomer (Sylgard 184, Dow Corning Corporation, Midland, Michigan, USA). The PDMS elastomer itself had two components: an elastomer base and an elastomer curing agent. At the beginning, a small plastic pot was chosen in which four holes were created. Then, one end of the silica tubes was fixed inside the holes and the other end was placed within the pot following different orientations. The tubes (inner diameter of 1.58 mm) were oriented in different directions so that it was possible to guide the needle (outer diameter of 0.9 mm) inside the tube and bend it accordingly to assess tracking curvature. PDMS elastomer was used as a medium to keep the tubes' orientation stable. The medium was prepared by thoroughly mixing the base and the curing agent in a ratio of 10:1 and then poured inside the pot to cover all the tubes. Since the mixture had a significant quantity of air bubbles that could cause artifacts in MRI images, degassing was performed by placing the mixture in a vacuum degassing oven for a couple of hours. When all the bubbles disappeared, the oven temperature was set to 60°C for one hour. Then the mixture became solid and the phantom was ready for the experiment. Six multi-modality radiology markers (IZI Medical Products, Maryland, USA) were placed facing the needle entry point so that it was possible to touch the markers' center point with the needle tip. Finally, MRI images of

the gel phantom were acquired from a 3T clinical MR scanner available at Centre hospitalier de l'Université de Montréal (CHUM), Montreal, QC, Canada.

In order to generate a model from the MRI image volume, a simple thresholding was first applied to extract the tube structures. Then, a 3D surface model was constructed from the segmented image data by applying marching cubes algorithm [89]. The model was further improved and smoothed to generate a continuous 3D shape model. Figure 4.10 shows the original gel phantom and the generated model from the MRI image.

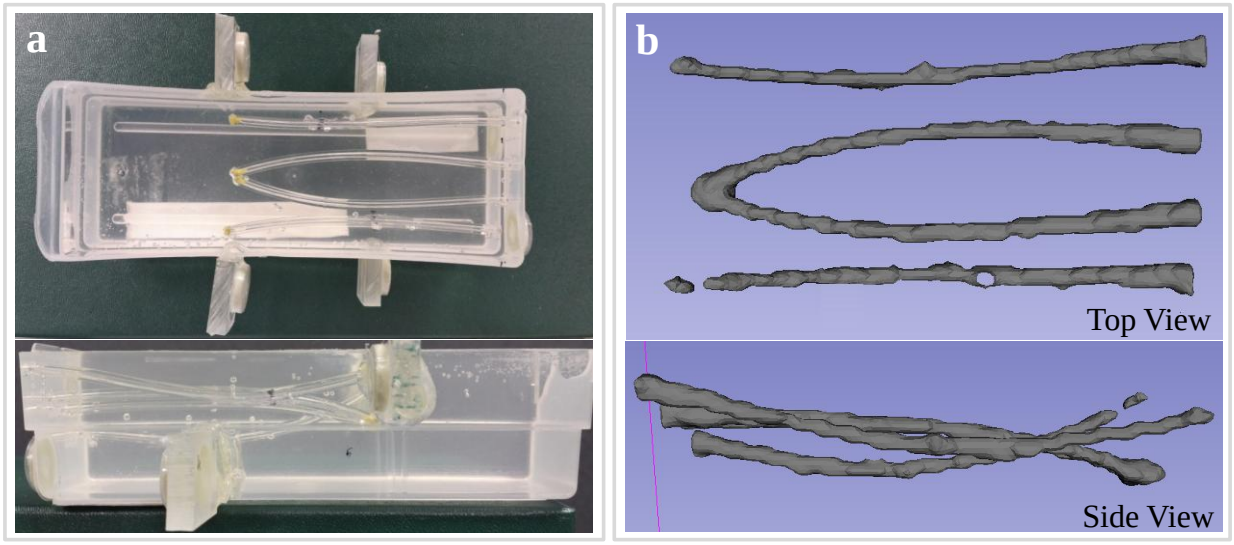

Figure 4.10: (a) Original gel phantom and (b) the generated model from the preoperative MRI image.

4.6.3 Robotic system for needle translation

We assembled three Newport PM500 linear stages on a flat metal tool board. As the accuracy of the PM500 stage greatly depends on the smoothness of the surface beneath, great care was taken when mounting the stages on the board. At first, any remaining dirt, dust or hard spots that might hinder the smoothness of the surface were removed from the board. We started by rubbing the surface with an Indian oil stone and then gently placed the stages on the cleaned surface. Two horizontal PM500 stages were arranged, one on top of the other, where the bottom stage moved front-to-back and the upper stage moved side-to-side. One vertical linear stage was then placed on top of the horizontal stages to move up and down. It is important to note that all the three stages were attached carefully such that the center of mass of all the three PM500 stages was

well-aligned. Figure 4.11 shows the various parts of our robotic system that was used for the needle translation.

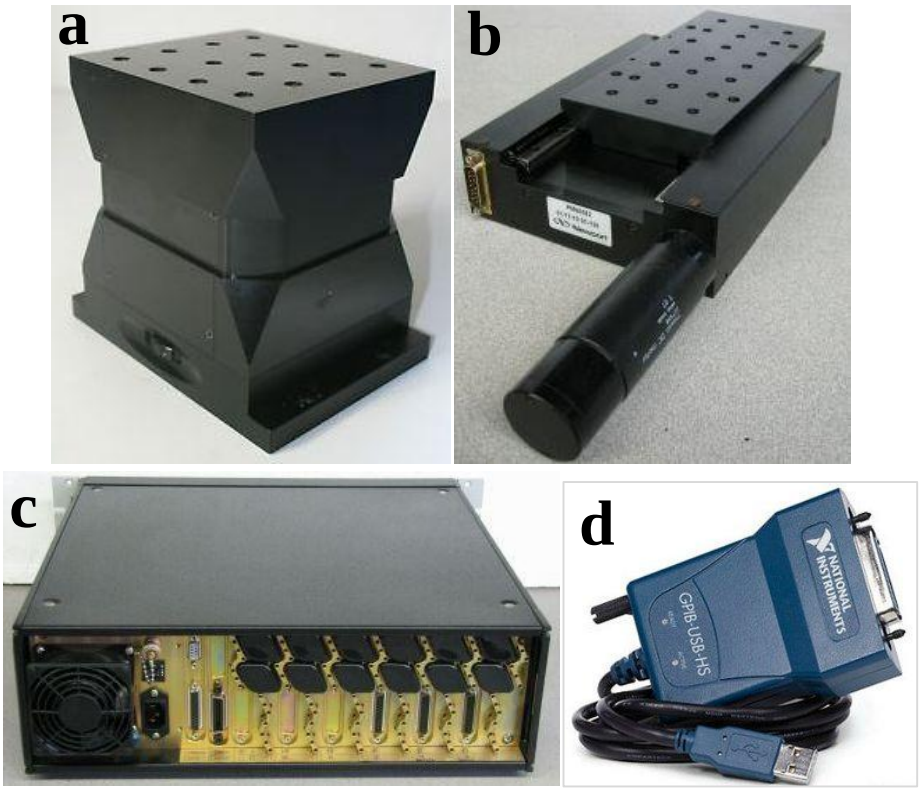

Figure 4.11: Various parts of the robotic system, (a) vertical and (b) horizontal PM500 linear stages; (c) rear side of a controller and (d) National Instruments GPIB-USB-A Controller for universal serial bus (USB). Image source from: (a-c) www.newport.com and (d) https://www.ni.com. Used with permission.

All stages were attached firmly with particular care and the weight of the combined load (i.e. additional upper stages with cable connectors and needle holder) was supported by the base stage. We also left the rear panel of the controller unblocked, in order to allow for air ventilation and provide adequate cooling. As suggested in the manufacturer's reference manual, cables were arranged carefully to avoid any disturbance due to tension or friction of the cables during motion. In case of an emergency, a Bayonet Neill–Concelman (BNC) connector, next to the cooling fan of the controller, was set up to shut down the whole system instantly.

In the reference manual, two communication interfaces were recommended: RS-232 and general purpose interface bus (GPIB). There are some advantages of GPIB over an RS-232 interface such

as providing more speed, capability to handle more than one instrument per GPIB controller card and an advanced synchronization ability [90]. In our robotic setup for needle translation, a computer was connected to the PM500 system by a GPIB-USB-HS (IEEE 488) interface adapter from National Instruments (NI), Austin, Texas, USA (as shown in Figure 4.11d). Furthermore, a software driver from NI to support GPIB-USB-HS was installed on the computer. MATLAB can support the GPIB interface through its "Instrument Control Toolbox". We developed an application in Matlab to control the whole PM500 system from a computer. The application allowed us to move the needle in three different directions and send the current combined translation of the needle from its initial position to Slicer. This translation information was used to update the reconstructed needle shape model in Slicer. Figure 4.12 shows the flow of commands sent to the PM500 system from a computer and data received from a PM500 system by the computer through a GPIB port via standard IEEE-488 cables.

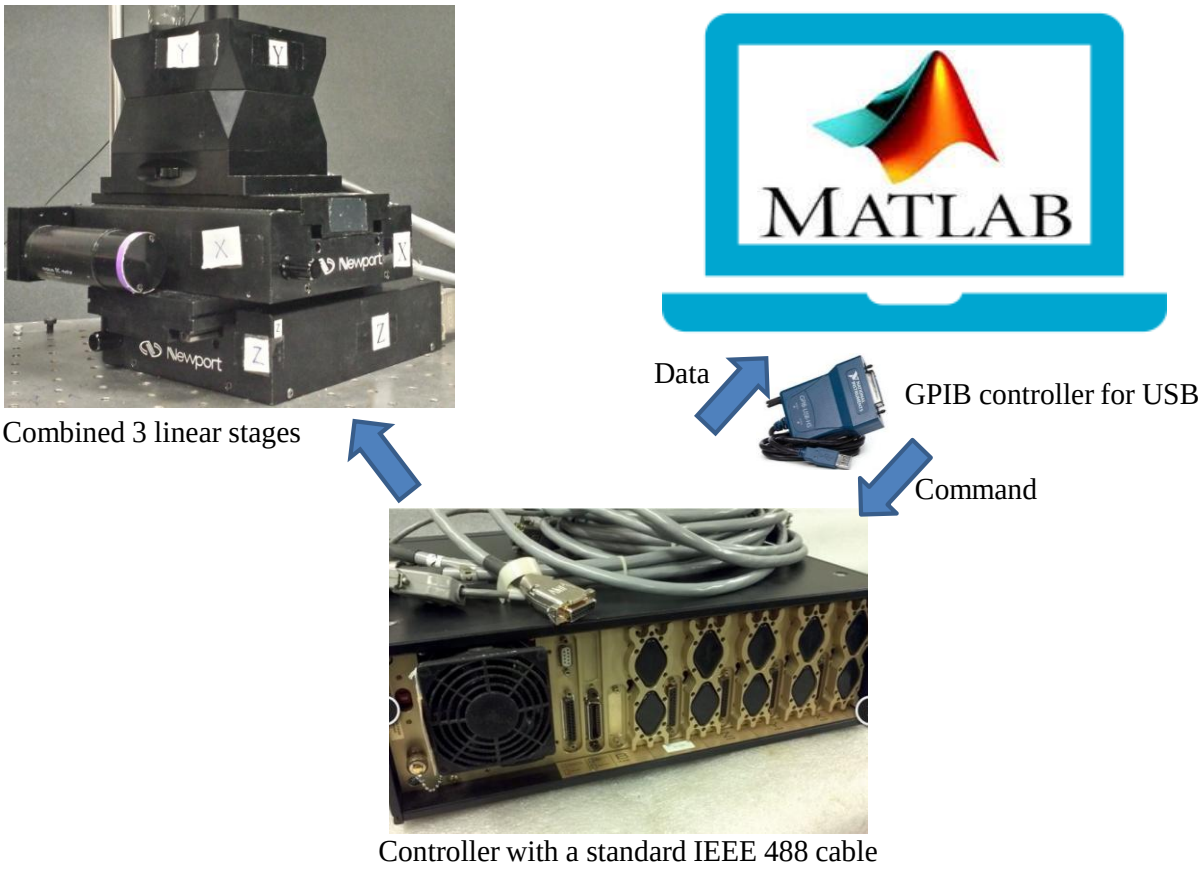

Figure 4.12: Illustration of the communication between the PM500 system and a computer.

4.6.4 Point-based registration

In order to represent the 3D reconstructed needle shape in correspondence with the preoperative MRI image space including the phantom, a phantom-to-image registration was developed to register both coordinate systems. Registration describes the mathematical relationship between two spaces to align one space to another. When this mathematical relationship is represented by using a 4×4 homogeneous matrix containing 3D rotation and 3D translation together - the registration is called, "rigid". Among the various rigid registration methods, point-based registration is the most popular for IGI. The main reason of its popularity stems from its closed form solution when a point set in the source space and its corresponding point set in the target space are given. The point set can be obtained by identifying landmarks from the anatomical structures of the patient (e.g. grooves of the phantom for our in-vitro experiment) or directly from the fiducial markers placed on a patient (e.g. skin markers fixed to our gel phantom). The main benefits of the fiducial marker-based approach over anatomical landmarks are the ability to select any number of points in any orientation, higher accuracy of point localization and ease of establishing the point correspondences.

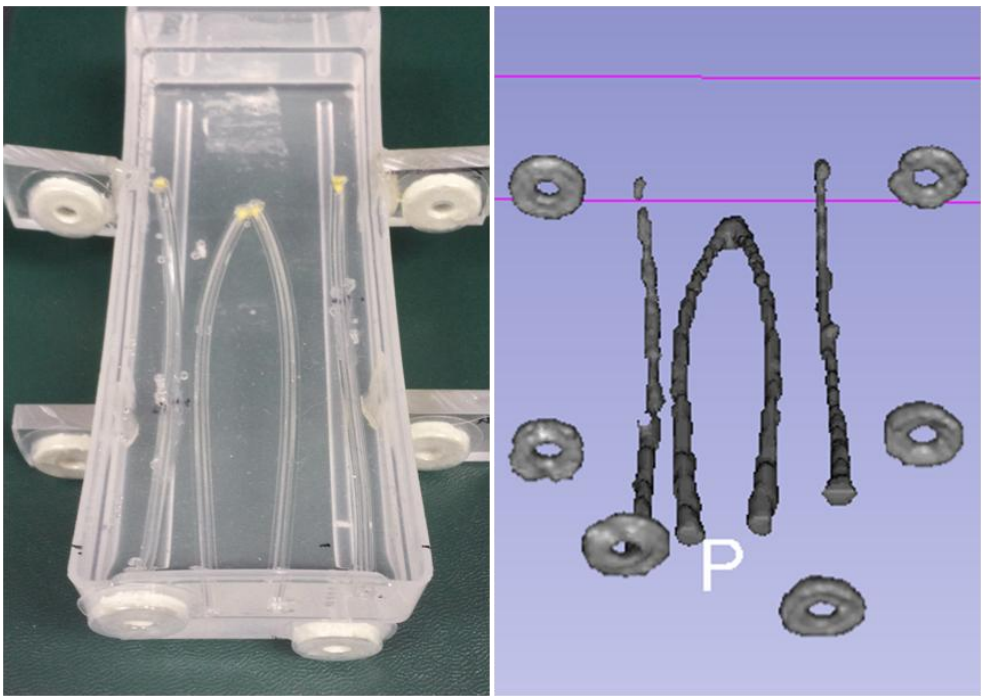

Figure 4.13: Six multi-modality radiology disk-shaped markers used for the point-based registration.

We used a 3D model of the planar validation phantom (as shown before, in Figure 4.6b) and a preoperative MRI image of the PDMS gel phantom for our in-vitro experiments. For the gel phantom, a set of multi-modality radiology markers (IZI Medical Products, Maryland, USA) was used as the fiducials for registration (see Figure 4.13).

To perform the experiment with the gel phantom, we loaded the preoperative MRI image of the phantom within the Slicer environment. The MRI image was in "Digital imaging and communications in medicine" (DICOM) format, a standard in medical imaging. Then, we searched for the multi-modality radiology markers in the MRI image slices and carefully placed fiducials at the center of the marker's position, as shown in Figure 4.14.

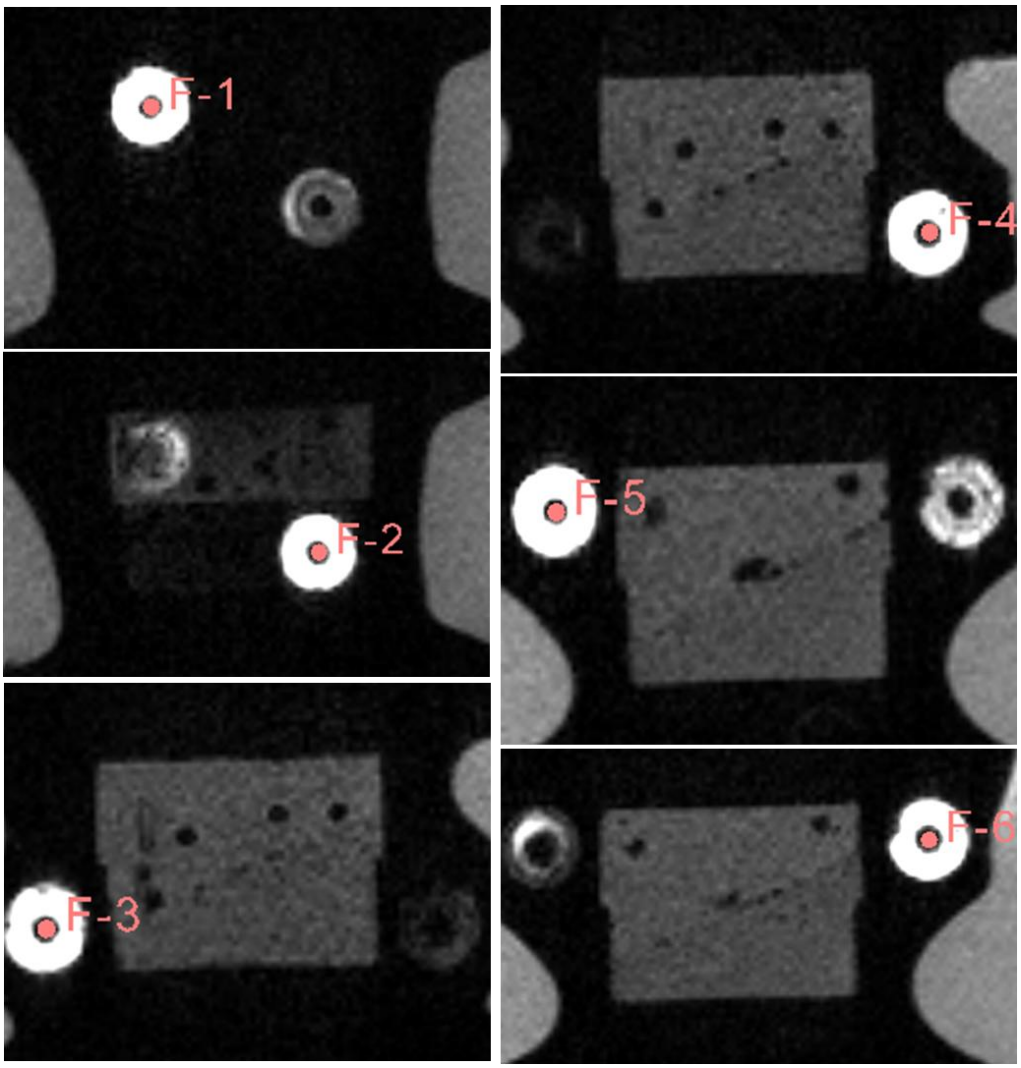

Figure 4.14: In Slicer, fiducial points were selected at the center of the multi-modality radiology disk-shaped markers visible in the MRI DICOM images.

Once the fiducials were selected in the image space, the 3D positions were stored locally on the PC in order to perform the registration afterward. During the registration procedure, the positions of the fiducials in the physical space were obtained by placing the tip of the needle at the center of the markers and recording the needle tip. Accurate needle placement was achieved by using our robotic system for needle translation.

On the other hand, to perform point-based registration using the planar phantom, we began by loading the 3D model of the phantom in Slicer. We then placed the fiducials at several easily identifiable locations (such as grooves or corners) of the phantom. These fiducials' position (as shown in Figure 4.15) were saved and used repetitively during subsequent registration procedures. Similar to the experiment with the gel phantom, the corresponding fiducials' locations in the physical space were acquired by touching these positions with the tip of the needle.

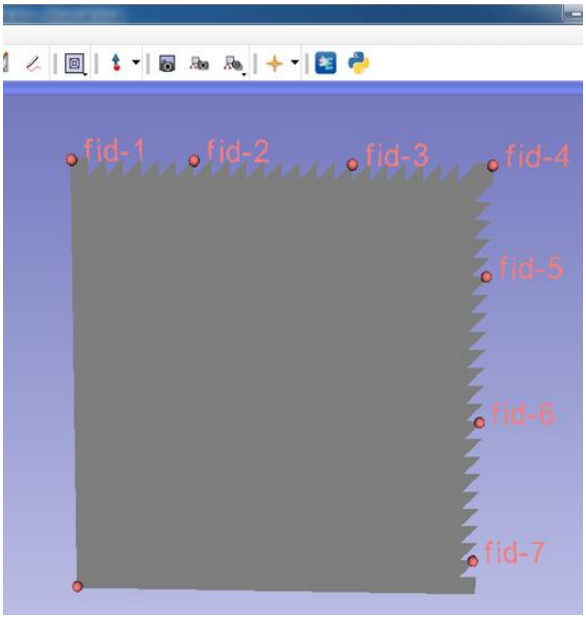

Figure 4.15: Several landmarks such as grooves and corners were selected as the fiducials.

Once a set of fiducial points is defined in both the image and physical spaces, point-based registration was performed to find a rigid transformation from one space to the other. Let us now describe the steps of the point-based rigid registration algorithm. For the sake of simplicity, we can represent the fiducials in physical space and image space as P and I, respectively, while N is the total number of fiducials in each coordinate system. The measurement of fiducial locations in each coordinate system contains some errors. If we assume errors are isotropic, identical and

symmetric random noise for all the fiducials, then the unknown transformation can be calculated by finding the rotation R and the translation T that minimizes the error. Therefore, the registration problem can be formulated as follows [91]:

$$\arg_{T,R} \min \frac{1}{N}\sum_{i=1}^{N}\left|\left(RP_i + T\right) - I_i\right|^2 \qquad \text{(Eq. 4.7)}$$

First, we need to calculate the mean of the fiducials' position in each space

$$\overline{P} = \frac{1}{N}\sum_{i}^{N} P_i$$

$$\bar{I} = \frac{1}{N}\sum_{i}^{N} I_i$$

The translation T can be defined as $T = \bar{I} - R\overline{P}$. To find R. Initially, we need to subtract the mean from every fiducial position in each space. So, we get $\tilde{P}_i = P_i - \overline{P}$ and $\tilde{I}_i = I_i - \bar{I}$ where the centroid of the fiducials is the same in both spaces. This allows expressing Eq. 4.7 as follows:

$\arg_R \min \frac{1}{N}\sum_{i=1}^{N}\left|R\tilde{P}_i - \tilde{I}_i\right|^2$ which can be expanded to

$$\arg_R \min \frac{1}{N}\sum_{i=1}^{N}\left[\tilde{P}_i^2 - 2\left(R\tilde{P}_i\right)\cdot\tilde{I}_i + \tilde{I}_i^2\right] \qquad \text{(Eq. 4.8)}$$

Eq. 4.8 can be equivalently rewritten as the maximum of similarity:

$$\max \frac{1}{N}\sum_{i=1}^{N}\left(R\tilde{P}_i\right)\cdot\tilde{I} \qquad \text{(Eq. 4.9)}$$

which can also be written using the trace of the covariance matrix, $R\tilde{P}\tilde{I}^T$ as follows:

$$\max\left(trace\left(R\tilde{P}\tilde{I}^T\right)\right) \qquad \text{(Eq. 4.10)}$$

According to the singular value decomposition (SVD) theorem, the square matrix $\tilde{\tilde{P}}\tilde{\tilde{I}}^T$ can be represented by the product of three matrices: two orthonormal matrices U, V and a diagonal matrix Λ:

$$\tilde{\tilde{P}}\tilde{\tilde{I}}^T = U\Lambda V^T \qquad \text{(Eq. 4.11)}$$

where $U^TU = V^TV$ is the identity matrix, $\Lambda = diag(\lambda_1, \lambda_2, \lambda_3)$ and the eigenvalues $\lambda_1, \lambda_2, \lambda_3$ are non-negative. Finally, the rotation R that maximizes the trace (in Eq. 4.10) and minimizes the error (in Eq. 4.7) can be found as:

$$R = V \quad diag(1,1,\det(VU)) \quad U^T \qquad \text{(Eq. 4.12)}$$

More detailed explanations of this method can be found in [91]. The complete implementation of the point-based registration algorithm is built in Slicer as a module named, "Fiducial Registration". In our project, we used this module to perform the registration.

4.7 Validation methodology

As we can see, the registration step is important for any IGI system to match the physical space with the image space. Therefore, the quality of the registration must be determined before beginning an intervention. In general, any non-zero displacement (typically, represented as the root mean square (RMS) distance) between a transformed point from physical to image space and the corresponding point in image space is considered as the registration error. Fiducial registration error (FRE) is a commonly used indicator of registration accuracy. FRE is defined as (according to Eq. 4.13) the RMS distance between the corresponding fiducials in physical and image space after the registration:

$$FRE = \sqrt{\frac{1}{N}\sum_{i}^{N}(\hat{y}_i - y_i)} \qquad \text{(Eq. 4.13)}$$

where $\hat{y}_i$ is the transformed fiducial location from the physical space to image space, y_i is the corresponding fiducial location in the image space and N is the total number of fiducial points used for the registration. A high FRE indicates a poor alignment between the coordinate spaces,

whereas a low FRE indicates a better matching between them. However, a low FRE does not always imply a truly accurate registration. Therefore, target registration error (TRE) should also be considered that can better represent the accuracy of the given registration by showing the actual uncertainty at the point of interest. Registration with low FRE cannot ensure a low TRE and vice versa [92]. The TRE can be calculated similarly to FRE, as the RMS distance between corresponding points (i.e. targets) other than fiducials in physical space and image space. Generally, a few factors such as the number of fiducials and their configuration relative to the target are considered to improve the accuracy of the registration. In this project, both FRE and TRE were calculated for all the in-vitro experiments.

4.8 Summary

In this chapter, we described the entire experimental setup for this project, as well as the fabrication process of the needle and various phantoms used for validation. Moreover, the calibration procedure was illustrated, followed by a description of the needle 3D shape reconstruction methodology. The data flow from the FBG data acquisition to the visualization of the 3D shape-sensing needle in Slicer was also demonstrated. Finally, this section concluded with the description of the validation technique employed in this project. In the next section, we will present the experimental results using the methods described here.

CHAPTER 5 RESULTS

During RFA interventions, the needle shape and the tip position need to be displayed in real-time with respect to the preoperative image of the patient, along with the selected target. The overlay of the needle shape helps the interventional radiologist to guide the needle tip precisely to the target. In this chapter, we represent the results evaluating various components of the proposed system. First, section 5.1 illustrates the reconstructed needle shape in Slicer using our proposed calibration procedure. In this project, we used an NDI Aurora EMTS as the state of the art tracking system. Section 5.2 demonstrates the tip position and orientation of a needle tip in Slicer when the tip is tracked by the Aurora system. Then, we show the results of all three in-vitro experiments performed with our developed FBG-based tracking system in section 5.3, 5.4 and 5.5 separately. These individual sections also include the results of similar experiments carried out with the Aurora EMTS for comparison. Finally, we conclude this chapter by a summary in section 5.6.

5.1 Needle shape representation in Slicer

In the first set of experiments, we applied our proposed calibration procedure, as described in section 4.3. During the calibration procedure, we calculated the strain from the measured wavelength-shift of each FBG sensor for different known deflections of the needle tip. The plot in Figure 5.1 shows the relationship between the strain and the wavelength-shift for each sensor at one triplet location. We represented this relationship by fitting a line using the least square method and then defined the slope of the fitted line as the calibration matrix.

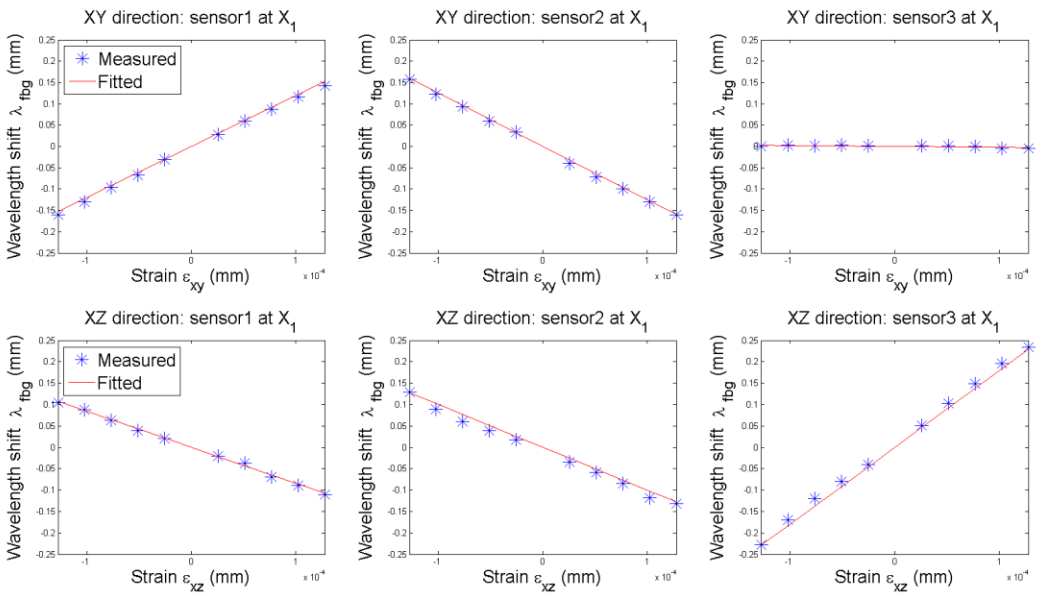

Figure 5.1: A line is fitted between the measured wavelength-shift and the strain values (calculated from the applied tip bending) to define the calibration matrix.

In Figure 5.1, the measured values of the wavelength-shift are represented with the '*' symbol, whereas the linear fits are shown with the line. It is important to note that bending at any triplet causes the wavelength-shift of one or two FBG sensors in one direction and the other FBG sensors in the opposite direction. For example, due to bending in the *xy* plane, a similar but opposite amount of wavelength-shift occurred at sensors #1 and #2 while sensor #3 was unaffected. On the other hand, bending in the *xz* plane caused the wavelength-shift of sensors #1 and #2 in the same direction, and an equal amount of wavelength-shift of sensor #3 in the opposite direction.

Afterward, we used the calibration matrices to get the 3D shape information of the needle profile. These 3D positions were sent to Slicer using the OpenIGTLink protocol by an OpenIGTLink connector named 'Deminsys' (see Figure 5.2). We developed a module in Slicer to represent the 3D view of our reconstructed needle model. Another OpenIGTLink connector (named 'NewPort') was also created to receive the needle translation information for updating the reconstructed needle position in Slicer.

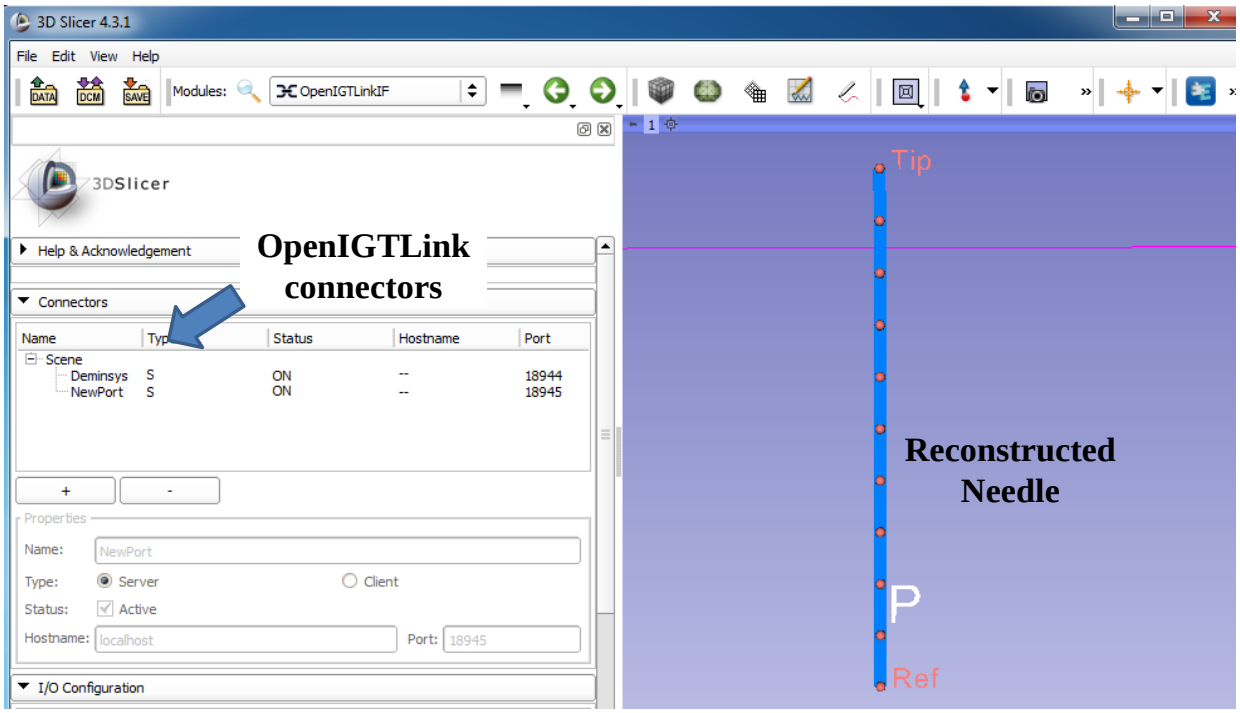

Figure 5.2: Slicer interface showing the reconstructed needle shape with two OpenIGTLink connectors.

5.2 Connecting NDI Aurora EMTS with Slicer

In this project, we compared the needle navigation accuracy of developed the FBG-based tracking system with the accuracy of the NDI Aurora EMTS in terms FRE and TRE accuracy. To perform this experiment, we integrated the Aurora system with our experimental setup, as shown in Figure 5.3. The Aurora system included a planar magnetic field (connected to the host computer by a USB port) and a Chiba-tip needle (18G/150mm). A 5DOF sensor was integrated into the tip of the needle that allowed the needle tip to be tracked during navigation in real-time. We installed the NDI toolbox software in the host computer to setup the NDI Aurora tracking system for needle tracking. The connection between the Aurora system and Slicer was established using the OpenIGTLink protocol.

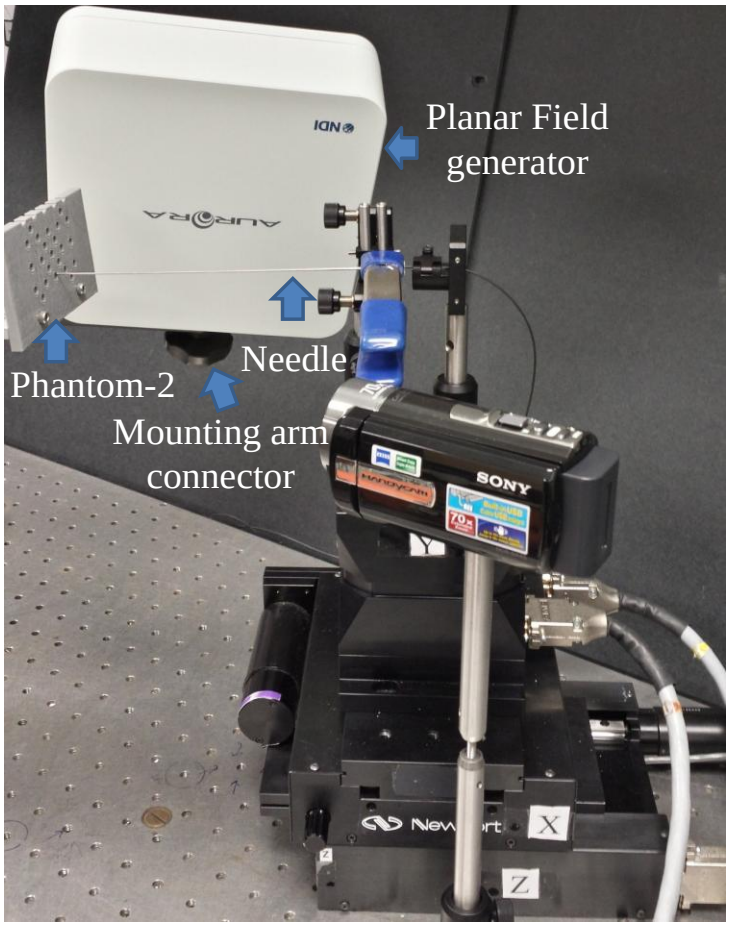

Figure 5.3: Experimental setup with an Aurora NDI EMTS where the field generator was placed close to the needle tip.

Before the experiment, the working environment was carefully tested to ensure there were no magnetic field distortions induced by any nearby ferromagnetic materials. We connected the field generator with a mounting arm that enabled us to place the field generator at any desired position and angulation. This mounting arm also restricted any unwanted movement of the field generator and provided reliable data measurements. The field generator was positioned close to the needle for tracking the tip precisely anywhere within the experimental volume. It was confirmed by moving the needle tip at various positions within the working volume for different orientations of the needle, and then checking whether the tip was properly tracked. A tool tracking utility was provided with the NDI toolbox that showed the tracking information (i.e. the 3D coordinate and orientation of the tip). This tracking utility also defined the characterized measurement volume in a graphical window.

During the experiment, the movement of either the field generator or the phantom was prohibited as the shifting of any of these could cause a misleading navigation of the needle tip. Furthermore, all the cables were kept separate from each other without any coiling or bending. Particular care was taken to place all the cables aside from the measurement volume as they could produce magnetic interference.

At the beginning of the experiment, we established a connection between the NDI Aurora system to Slicer using a software toolkit named, "Plus" [93]. Plus is an open-source software that can offer data acquisition from various devices such as tracking devices (e.g. NDI Aurora©), ultrasound imaging devices (e.g. Ultrasonix), and video capturing devices (e.g. Epiphan).

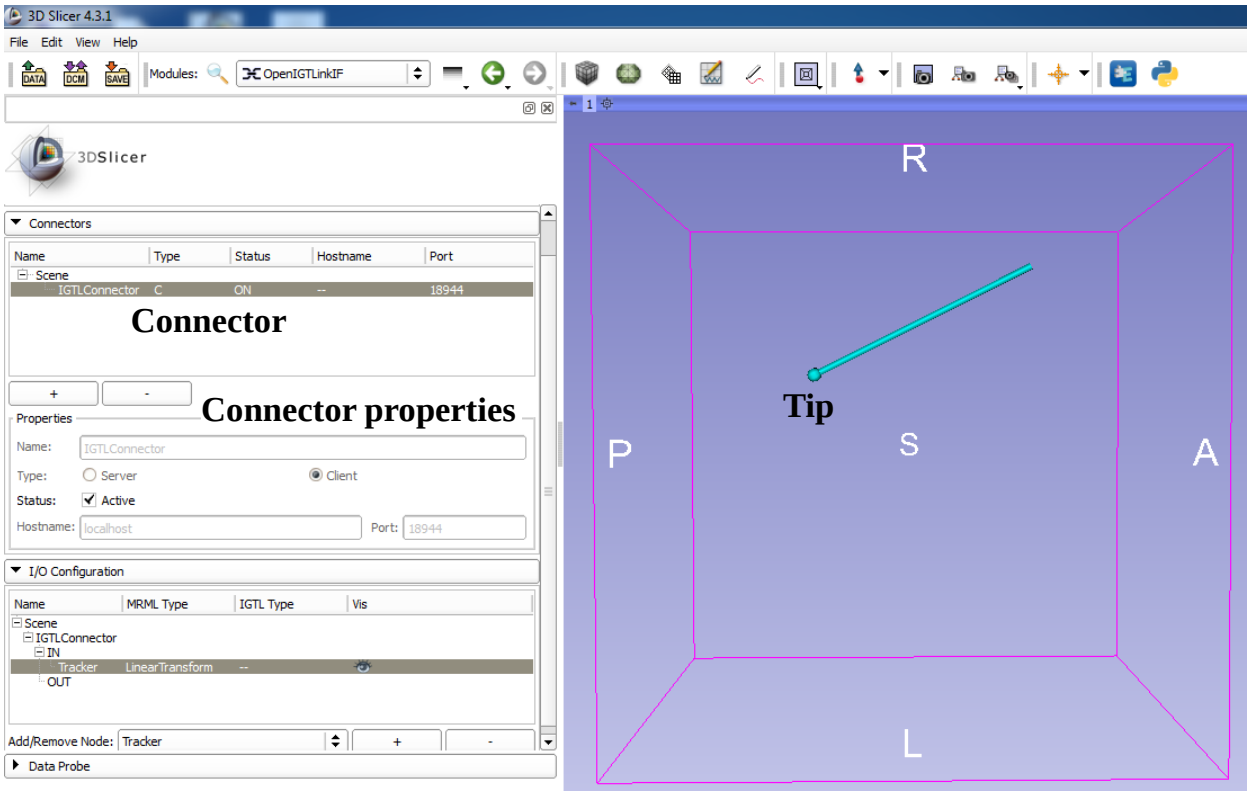

Figure 5.4: Acquiring needle tip tracking information from the NDI Aurora system to Slicer through an OpenIGTLink connection. A model in Slicer represents the needle tip with orientation.

First, we launched the Plus application and connected to the NDI Aurora Tracker by providing appropriate parameter values through an Extensible Markup Language (XML) file. We defined the parameters related to the Aurora system such as the type and ID of the tracker, serial port

number and acquisition rate. We also specified the parameters associated with the OpenIGTLink connection between Plus and Slicer (for example, port number, the type and name of transmitted message). The Plus application transmitted the tracking information (i.e. the 3D coordinate and orientation of the needle tip) from the Aurora tracker to Slicer. In Slicer, we created a connection through the OpenIGTLinkIF module to receive the transmitted data. As shown in Figure 5.4, the connection was built by providing the type (i.e. client) and port number (i.e. the listening port number defined in Plus). Once the connector started to receive the tracking data (as a 4x4 transformation matrix), we represented the 3D view of the needle tip in Slicer using a model.

5.3 In-vitro experiment with planar phantom-1

The first in-vitro experiment was performed using a planar phantom having regular grooves interleaved at a distance of 2.67 mm (as explained in Chapter 4 in Figure 4.9b). This phantom stabilized the needle tip at various deflections in both xy and xz planes independently. Prior to the experiment, the 3D model of the phantom was loaded in Slicer. The reconstructed shape of the needle was then fed to Slicer for visualization. Finally, a point-based registration was performed as described in section 4.6.4 to co-align both coordinate systems. Some specific grooves and corners of the phantom were used as fiducials for registration.

We used the "Fiducial Registration" module of Slicer to perform point-based registration. To define the input parameters of the algorithm, we selected the fiducials identified in the image or phantom model space as the "Fixed landmarks", while the fiducials in the physical space were selected as the "Moving landmarks". We obtained a registration matrix as an output of the module. The module also displayed the FRE with an output message indicating the quality of the registration. Figure 5.5 shows the interface of the "Fiducial Registration" module in Slicer.

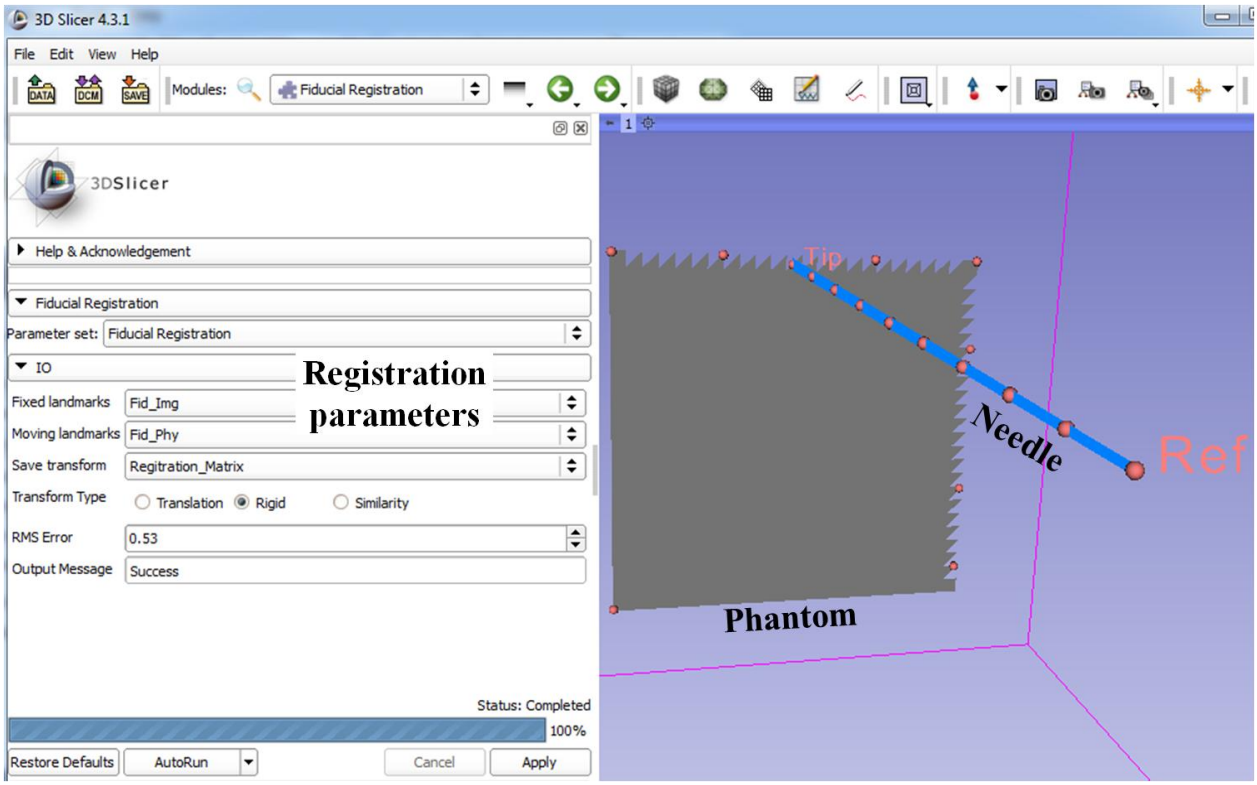

Figure 5.5: The interface of the module named, 'Fiducial Registration' in Slicer with its input and output parameters.

The interface provides the option to select a different set of fiducials as the input parameters and save the output registration matrix with RMS error. After obtaining a 4×4 homogeneous matrix as the registration matrix, we applied that matrix to the reconstructed needle shape to overlay on the phantom model. Then, the tip of the needle was placed in different grooves while the corresponding position of the tip and the needle shape in Slicer were captured. The needle navigation in the physical space was also recorded by the cameras used in our setup. We combined these two video sequences together for side-by-side comparison. Some screenshots of the video clip are shown in Figure 5.6.

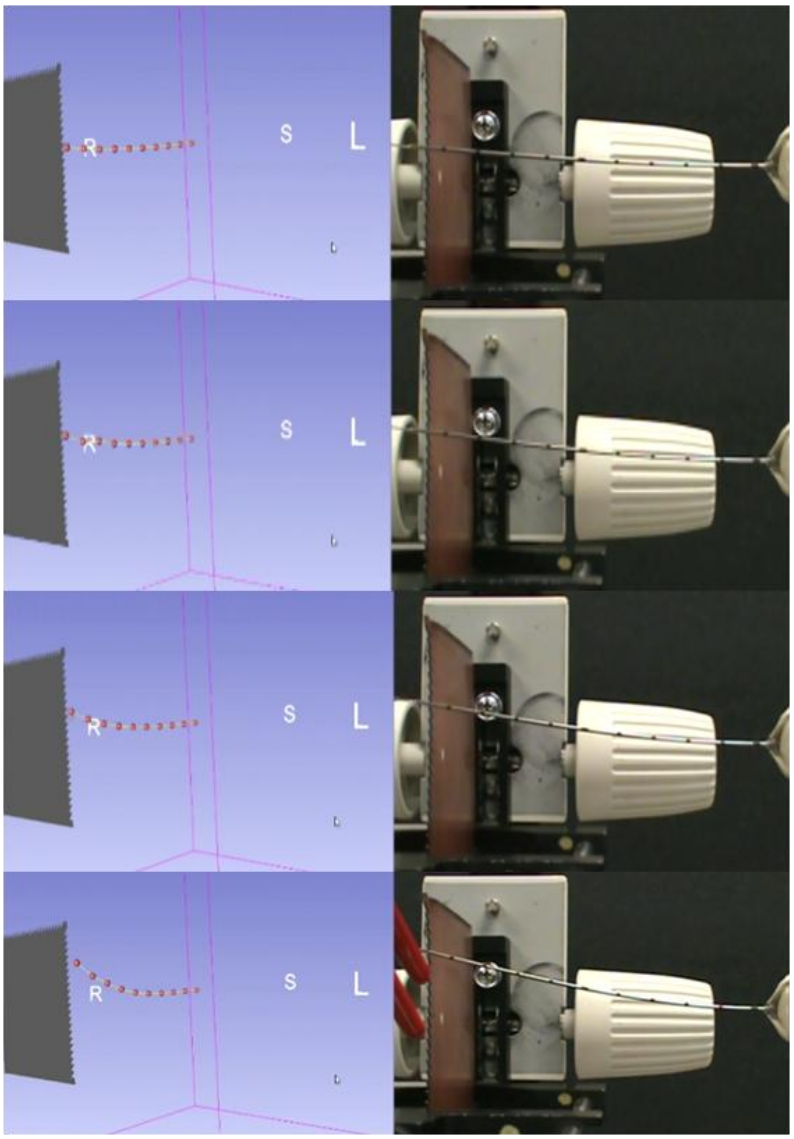

Figure 5.6: Real-time visualization of the reconstructed needle shape in Slicer for various tip deflections using the planar phantom-1.

In Figure 5.6, the left side shows the reconstructed 3D needle shape with its tip position in the grooves of the phantom model in Slicer and the right side displays the needle shape with tip position in the physical space. It is apparent from these results that for various levels of tip deflection, our reconstructed needle model can successfully show the accurate position of the needle tip.

Evaluating the quality of the registration accuracy is essential. One such quantitative measure is the fiducial registration error (FRE), as described in section 4.6. In this experiment, the FRE was

calculated repetitively using different sets of fiducial point pairs (N=6~8), where the average RMS error was found to be 0.54 ± 0.12 mm.

Another quantitative measure to assess registration accuracy, the target registration error (TRE), was calculated to evaluate the registration accuracy at the target location. The tip of the needle was placed in different grooves of the phantom, and the corresponding tip position of the needle model was recorded in Slicer. Obtaining the position of both the target (i.e. the groove) and the corresponding estimated needle tip in Slicer was straightforward and accurate, as it was possible to place a small sphere at both the positions in Slicer that showed their 3D coordinates directly. The RMS distance between the target and the needle tip was calculated to generate the TRE (as illustrated in Figure 5.7). The TRE was calculated at various points of interest of the phantom. However, the points that were used to calculate the FRE were not selected for the TRE.

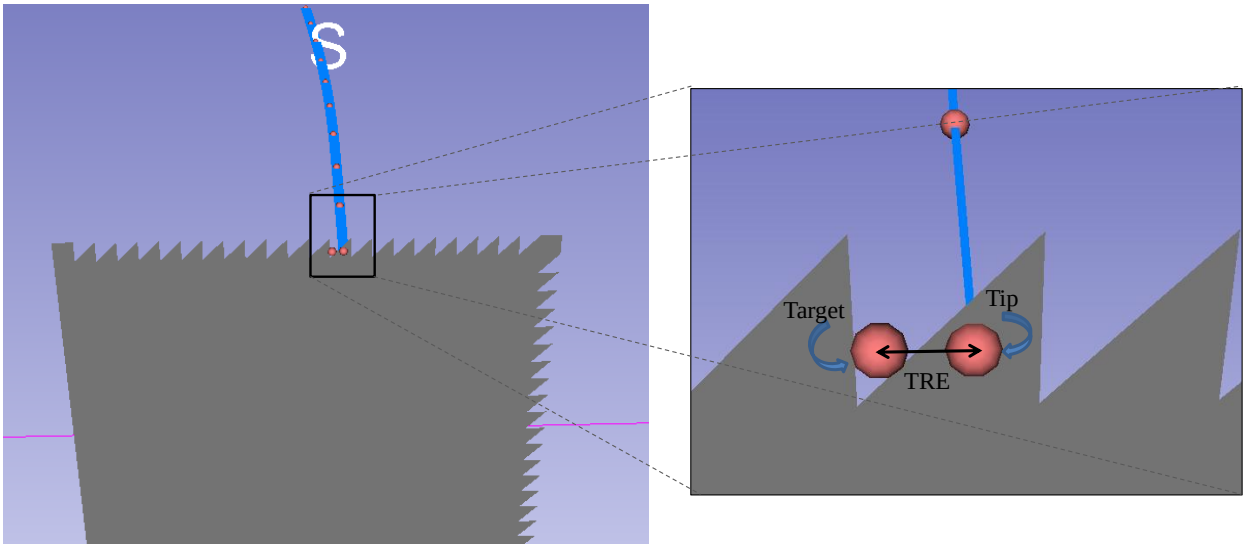

Figure 5.7: TRE is defined as the RMS distance between the actual target location and the estimated needle tip position in Slicer.

Phantom-1 allowed the deflection of the needle tip in both the *xy* and the *xz* plane separately up to 10.68 mm from its initial position. Figure 5.8 represents the TRE distribution for the tip deflection of ±2.67, ±5.34, ±8.01, ±10.68 mm from its initial position in both the *xy* and the *xz* direction. The measurements were taken 10 times at different grooves. Analyzing the error distribution statistically, we can see in the figure that the RMS error is increasing linearly with the amount of tip deflection (i.e. TRE = 0.05*tip_deflection_amount, where 0.05 is the slope).

The overall RMS error obtained by our system was 0.96 ± 0.05 mm and 0.95 ± 0.06 mm for a tip deflection maximum of 10.68 mm in *xy* and *xz* plane, respectively.

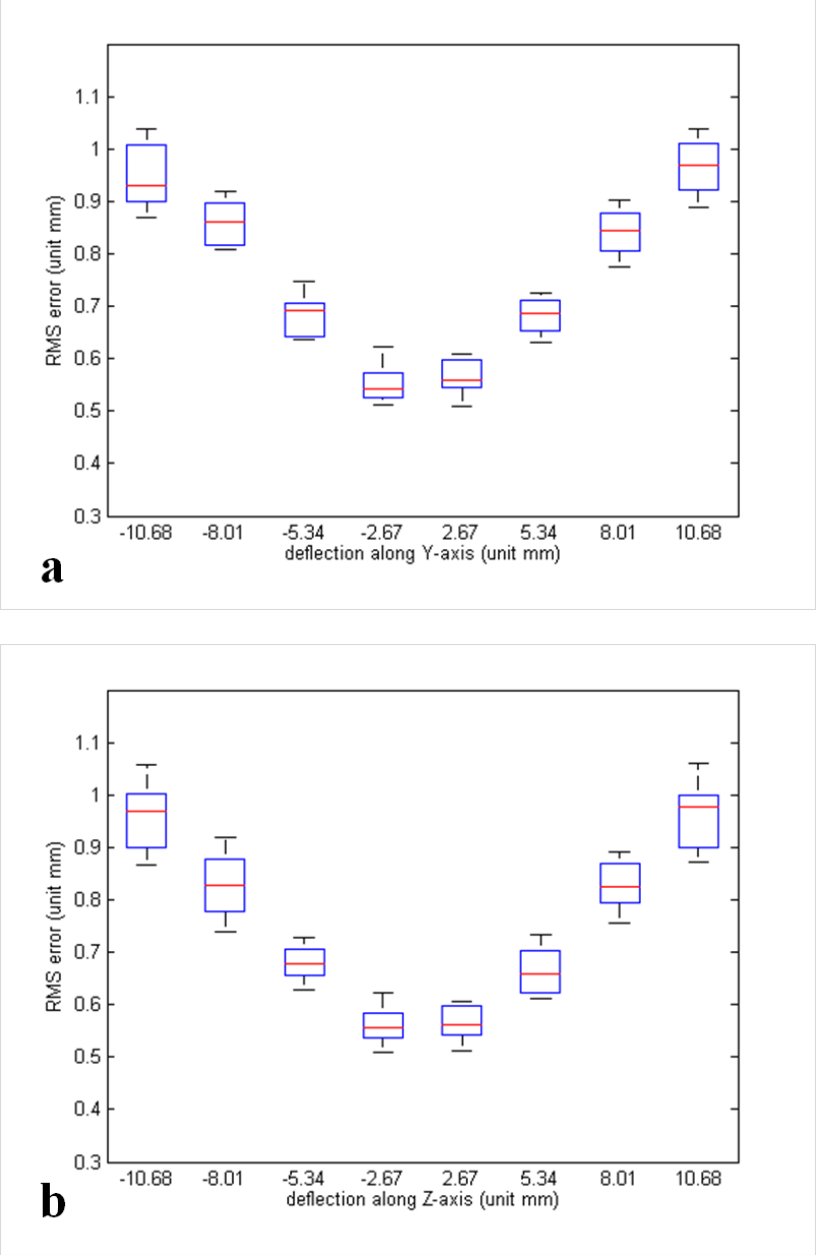

Figure 5.8: Accuracy of the estimated needle tip position of our FBG-based tracking at various deflections in both (a) *xy* and (b) *xz* planes of phantom-1.

We did the same experiment with the Aurora NDI EMTS. At first, we connected the Aurora system to Slicer as described in the previous section 5.2. Once we received the needle tip tracking information, then the phantom model was loaded in Slicer. We performed the registration

procedure using the similar grooves and the corner points of the phantom. After that, we applied the registration matrix on the needle model. We obtained an FRE of 0.49 ± 0.08 mm. The registered needle model was overlaid on the phantom-1 model. Then, similar to the experiment with the FBG-based tracking system, we placed the tip of the needle at different grooves and the corresponding position of the tip in Slicer was captured. We captured the entire needle navigation procedure by the cameras. Figure 5.9 shows a side-by-side comparison of the needle navigation in Slicer and the physical space.

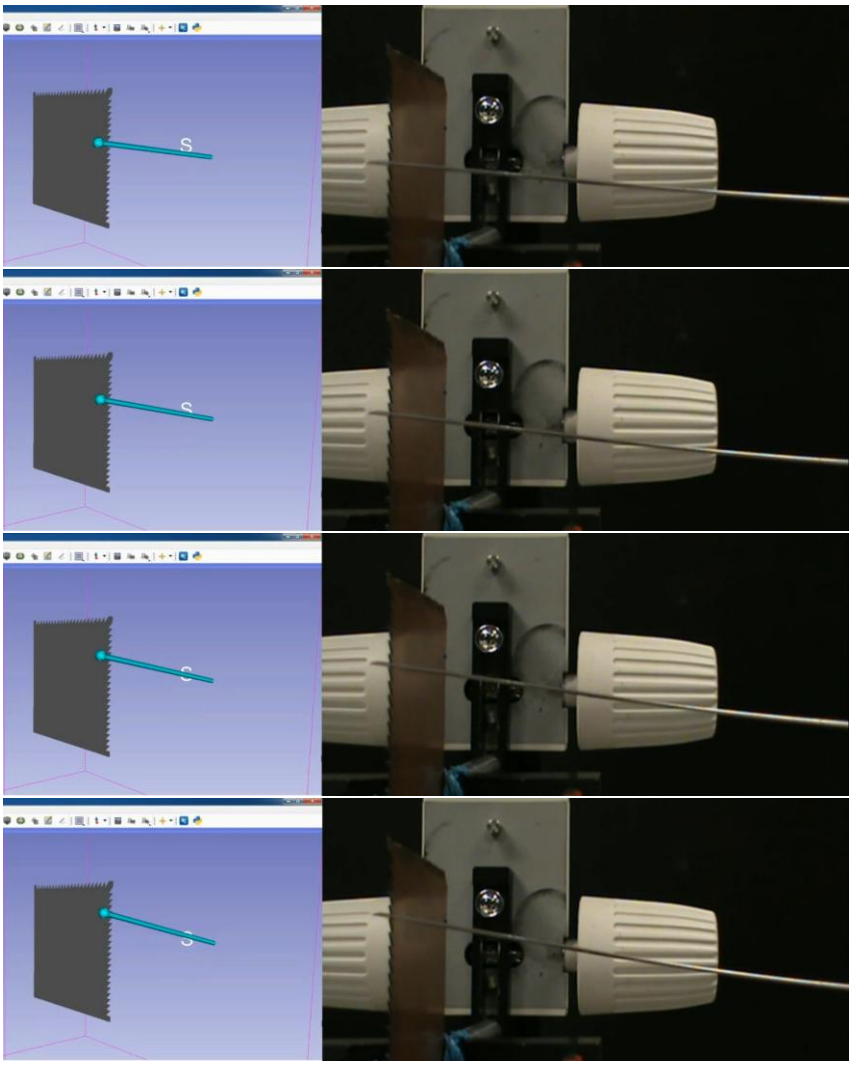

Figure 5.9: Real-time visualization of the EM-based needle navigation in Slicer for various tip deflections using planar phantom-1.

The left side of Figure 5.9 shows the tip position in the grooves of the phantom model in Slicer and the right side displays the corresponding needle shape with tip position in the physical space.

We calculated the TRE distribution for the tip deflection of ±2.67, ±5.34, ±8.01, ±10.68 mm from its initial position in both *xy* and *xz* direction. Figure 5.10 shows our calculated TRE distribution for the Aurora system. The overall mean RMS error obtained by the Aurora system was between 0.54~ 0.83 mm and 0.51~0.84 mm for a tip deflection maximum of 10.68 mm in *xy* and *xz* plane, respectively.

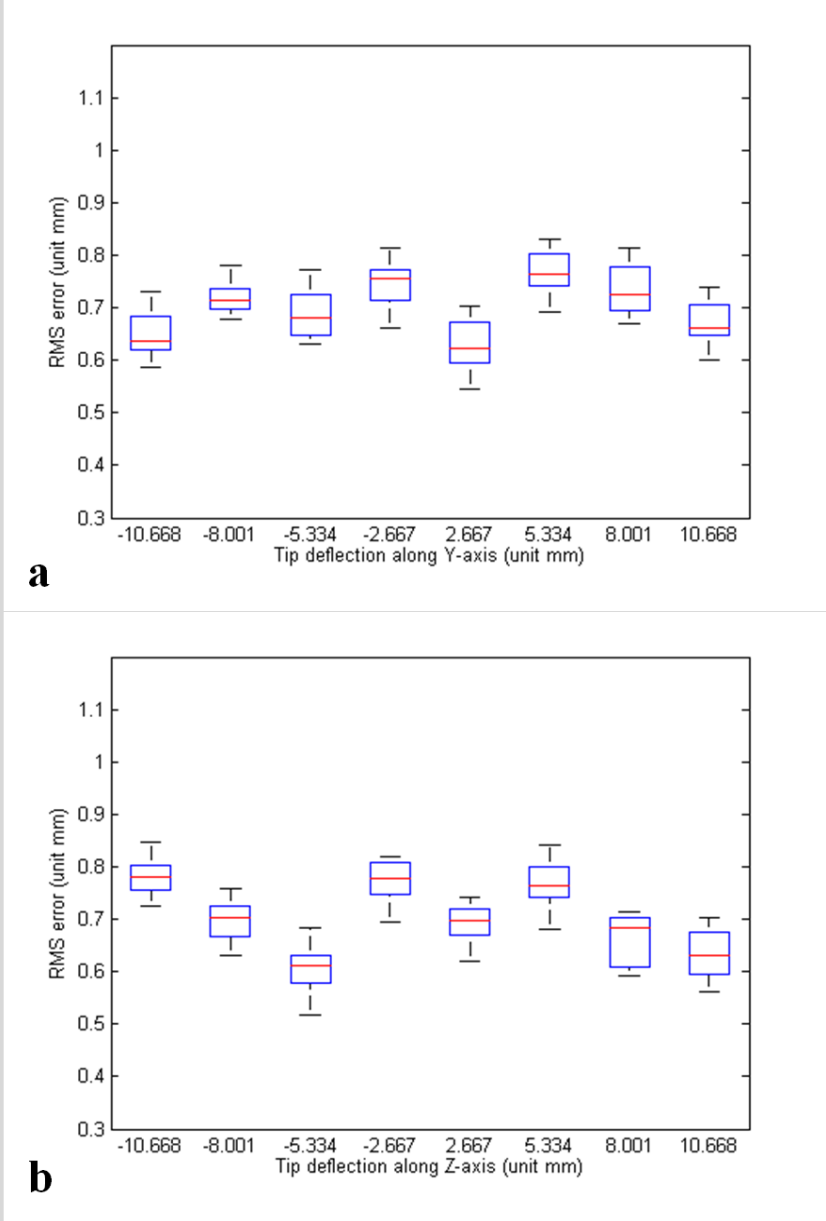

Figure 5.10: Accuracy of the estimated needle tip position of the Aurora system at various tip deflections in both (a) *xy* and (b) *xz* planes of phantom-1.

We also evaluated the shape accuracy of the reconstructed needle at different tip deflections for our developed FBG-based tracking system. In our experimental setup (as shown in chapter 4 in Figure 4.1), two cameras were installed that captured the top and the side views of the needle. The needle had a series of circular black markers uniformly placed on its shaft. These markers were clearly visible in the camera images and easily selected by clicking the mouse pointer on them.

When the needle is not bent, the physical distance between two successive markers is 10 mm, as shown in Figure 5.11. A similar equivalent distance between the successive markers was obtained from the camera image in a number of pixels, *#pixel*. Therefore, the physical distance between two pixels in the camera image was calculated by *dis* = 10 mm / *#pixels*.

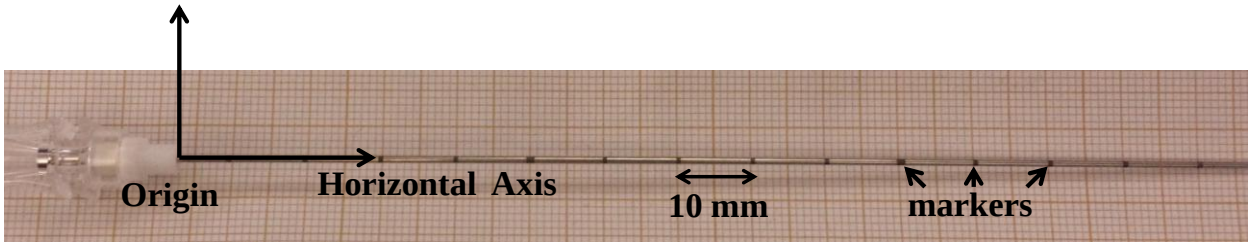

Figure 5.11: The markers on the needle shaft were used to find the needle shape from the camera images.

The base of the needle was used as the origin where the straight non-bending needle shaft was considered as the horizontal axis. Therefore, the positions of the markers of a non-bending needle from its base to the tip direction were [10 mm,0], [20 mm,0],...,[150 mm,0]. For any deflection of the tip, the needle shaft was bent, and the markers were displaced from the horizontal axis. This displacement for each marker was initially counted in pixels, then converted into a physical distance and finally the markers' position was defined from the origin.

On the other hand, the corresponding position of the markers in the reconstructed needle model was obtained directly from our reconstruction algorithm. In Figure 5.12, the plots show the theoretical position of the markers (denoted by 'O') that was calculated from the camera images. Also, the plots view the experimental position of the marker (denoted by '*') that was approximated by our algorithm. The calculated mean RMS error of the entire needle for the maximum tip deflection of ±10.68 mm were 1.42 ± 0.21 mm and 1.47 ± 0.19 mm in xy and xz plane, respectively. However, the needle provided with the Aurora system contained a sensor

only at the tip. As there was no sensor along the needle shaft, it was not possible to reconstruct the actual shape of the needle using the Aurora EMTS.

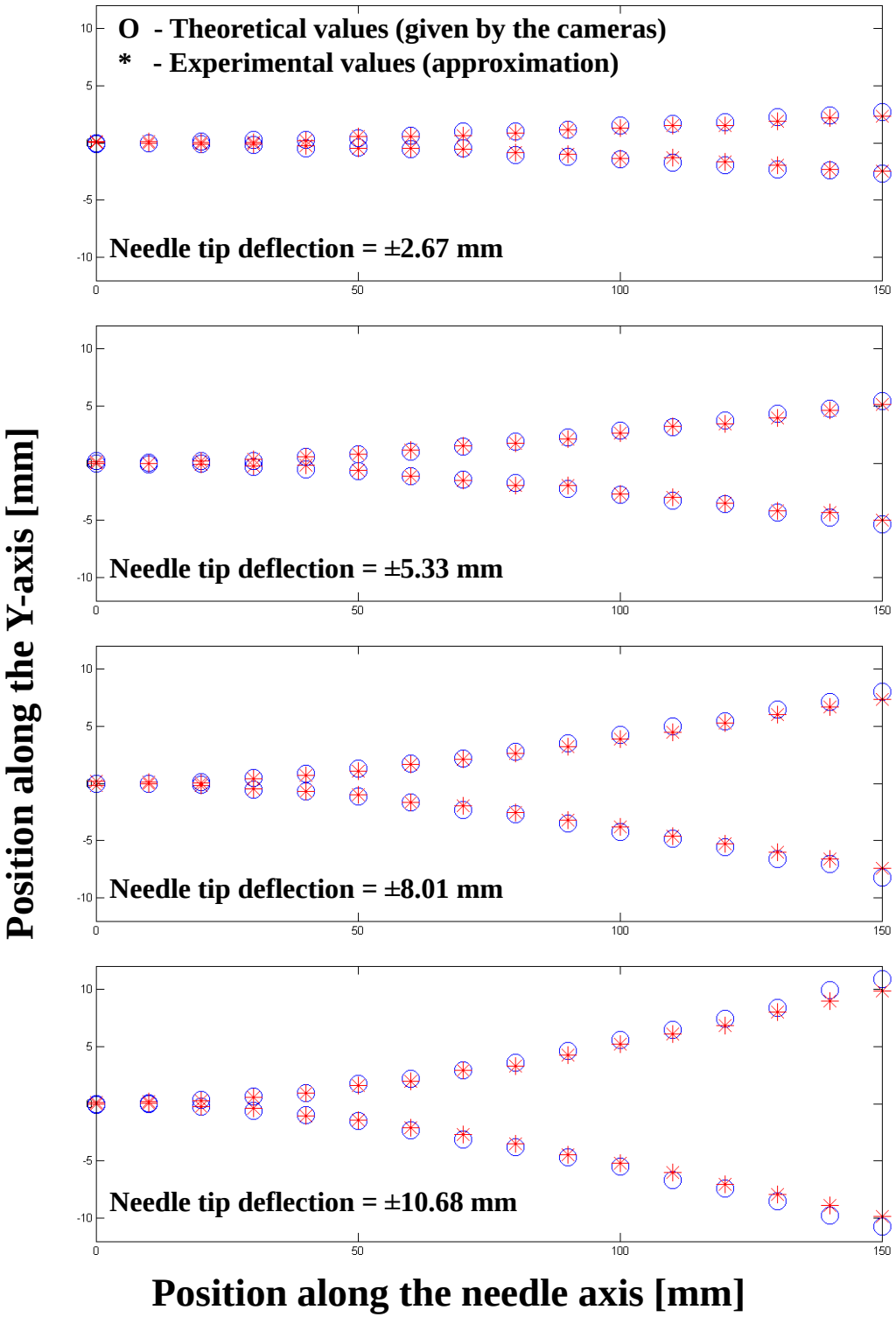

Figure 5.12: Comparison between the physical and approximated needle shape for several amounts of tip deflections in the *xy* plane. The plots show the position of the markers on the needle tip along the y-axis.

5.4 In-vitro experiment with planar phantom-2

We also performed the experiment with a second planar phantom (i.e. phantom-2, see Figure 5.13), which includes 23 holes that allow deflection of the needle tip in both *xy* and *xz* planes simultaneously at various magnitudes. Phantom-1 allowed deflection of the tip either in *xy* or *xz* plane, but phantom-2 ensured the tip deflection in both the *xy* and the *xz* planes at the same time.

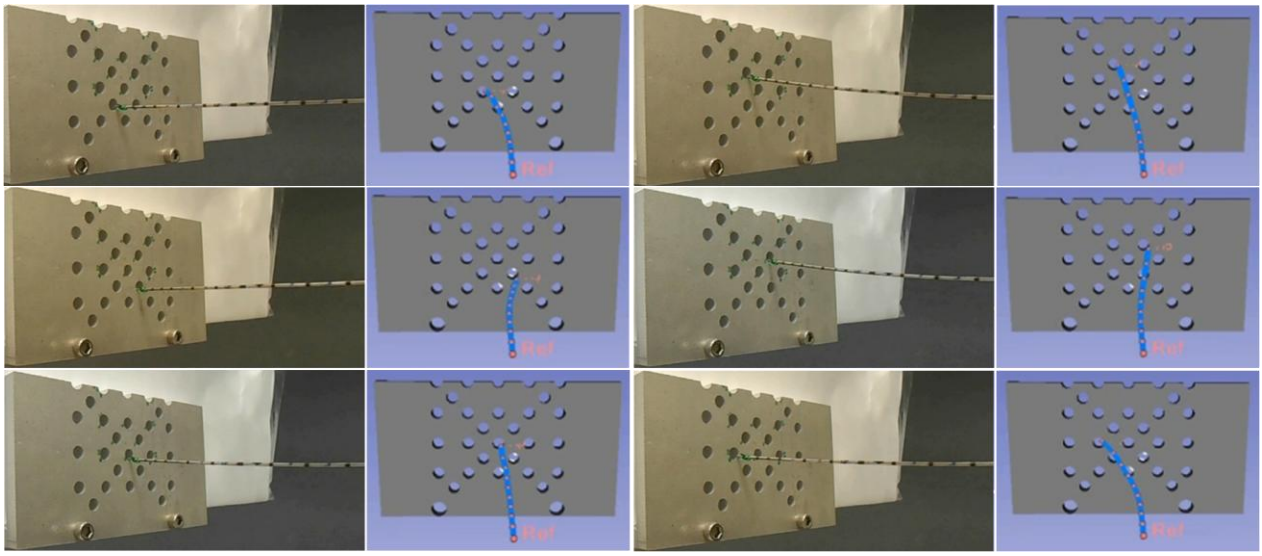

Figure 5.13: Real-time visualization of the reconstructed needle shape with its tip position in Slicer for various amount of tip deflections using planar phantom-2.

We performed the registration process using the different holes (N=6-8) of the phantom as the fiducials. The average FRE was 0.52 ± 0.11 mm. After applying the registration matrix on the reconstructed 3D needle shape, the tip of the needle was placed in different holes and the corresponding positions were observed in Slicer. The entire experiment was captured by video cameras while the needle navigation in Slicer was recorded using a screen capturing software. Figure 5.13 shows several side-by-side screenshots showing a real-time visualization of the reconstructed needle shape in Slicer for various amounts of tip deflections using the planar phantom-2.

The TRE was calculated in the same fashion as it was done previously with phantom-1. For this specific phantom, we deflected the tip of the needle at 2.35, 3.37, 8.05, 8.27, 14.51, 16.67 and 16.83 mm distances from its initial non-bending position (shown as a black star in Figure 5.14b).

Figure 5.14c represents a similar TRE distribution pattern to what was observed in Figure 5.6 for phantom-1. It showed a linearly increasing RMS error with the increase in the amount of tip deflection (i.e. TRE = 0.07*tip_deflection_amount, where 0.07 is the slope). The overall maximum RMS error obtained was approximately 1.05 ± 0.08 mm for a tip deflection maximum of 16.82mm.

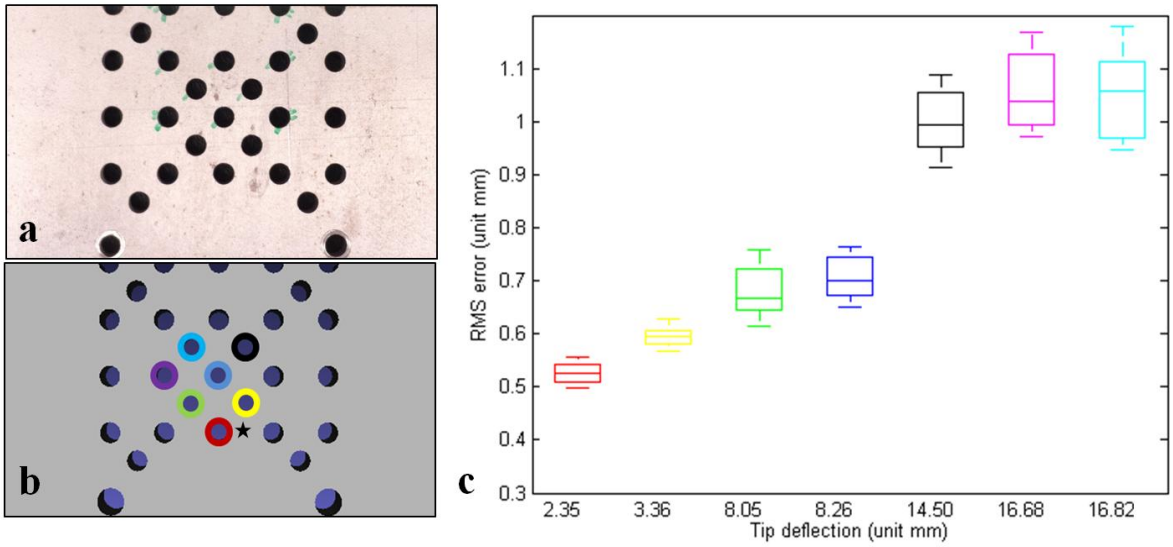

Figure 5.14: (a) Phantom-2 containing a set of holes and (b) its 3D model, the non-deflected needle tip position is shown as a black star, (c) RMS error distribution of the needle tip position at various deflections (shown in individual color) for the FBG-based tracking system.

We calculated the registration accuracy of the Aurora EMTS using phantom-2 in a similar way to what was done with the FBG-based system. As phantom-2 was made of metal, to avoid any metal interference, we prepared an exact replica of phantom-2 in plastic. This plastic phantom was made from a 3D printer. We performed the registration using the similar fiducial points that we used for the FBG-based tracking system. The mean RMS registration was of 0.58 ± 0.09 mm. Figure 5.15 shows the real-time needle navigation in Slicer using NDI Aurora EMTS. However, the model in Slicer only represented the tip of the needle with its orientation and did not describe the needle's shape.

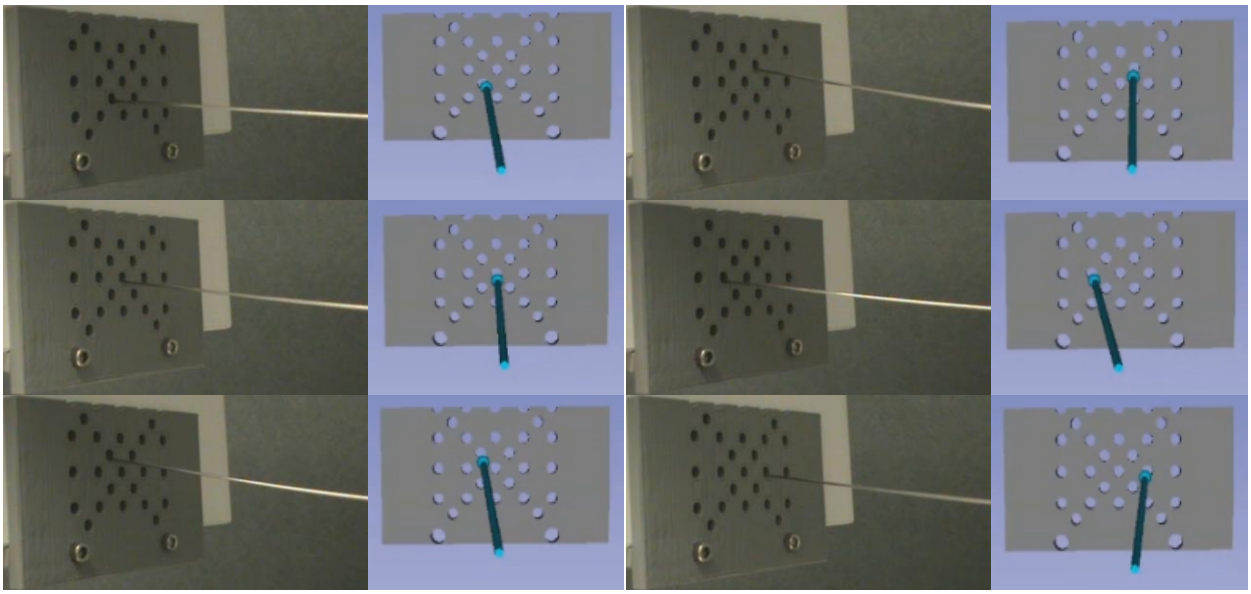

Figure 5.15: Real-time needle navigation with phantom-2 made in plastic in Slicer using NDI Aurora EMTS for various tip deflections.

We also calculated the TRE for the Aurora system using similar target points to those we considered for the FBG-based tracking system. The overall TRE was between 0.59 and 0.89 mm for the maximum tip deflection up to 16.82 mm (see Figure 5.16).

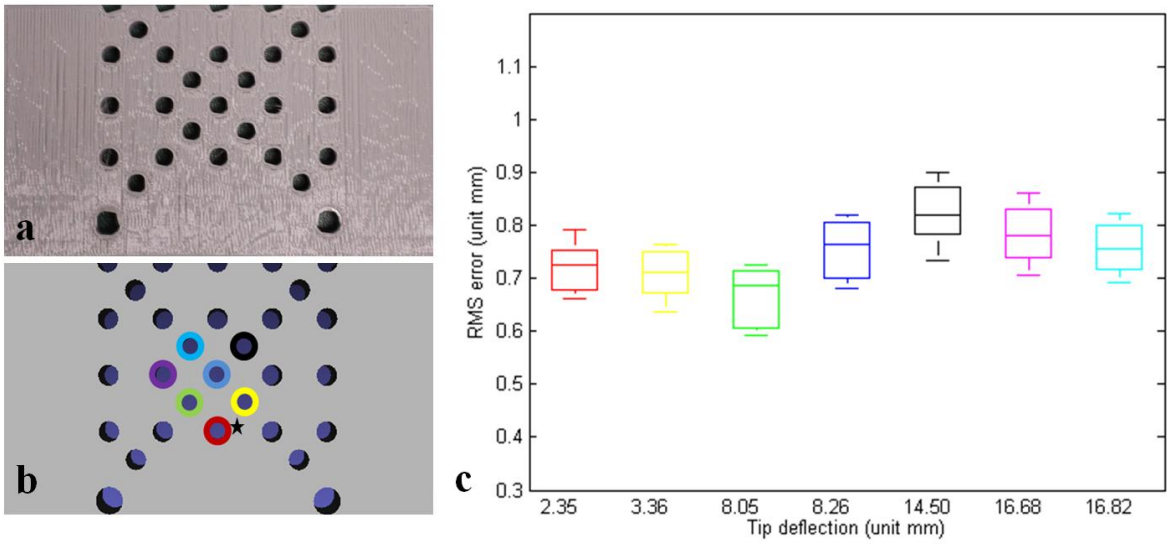

Figure 5.16: (a) Phantom-2 made of plastic containing a set of holes and (b) its 3D model, the non-deflected needle tip position is shown as a black star, (c) RMS error distribution of the needle tip position at various deflections (shown in individual color) for the Aurora EMTS.

The TRE error distribution in Figure 5.16c shows a random orientation. The bending of the needle tip does not have any effect on the needle tip tracking accuracy.

5.5 In-vitro experiment with gel phantom

The last set of in-vitro experiments validating the needle navigation with the shape sensing device was done with a tubular gel phantom, as described in section 4.6.2.2. At first, a point-based registration between the physical space and MRI image space was performed using a set of multi-modality radiology markers (N=6), yielding a mean RMS error of 0.84 ± 0.12 mm. Then, the 3D model of the gel phantom, which was prepared in advance, was loaded in Slicer. Once the registration matrix was applied to the reconstructed needle model, it was possible to navigate the needle through the tubes of the gel phantom. The needle navigation through various tubes is shown in Figure 5.17, where the reconstructed needle shape is visible inside the segmented tubes. However, navigation through one of the tubes was not accomplished, because of an internal blockage of the tube by the PDMS mixture. For the other three tubes, we guided the needle tip to the end position of the tubes and those end positions were used as the targets to measure TRE. The average TRE error calculated for this experiment was 1.19 ± 0.09 mm.

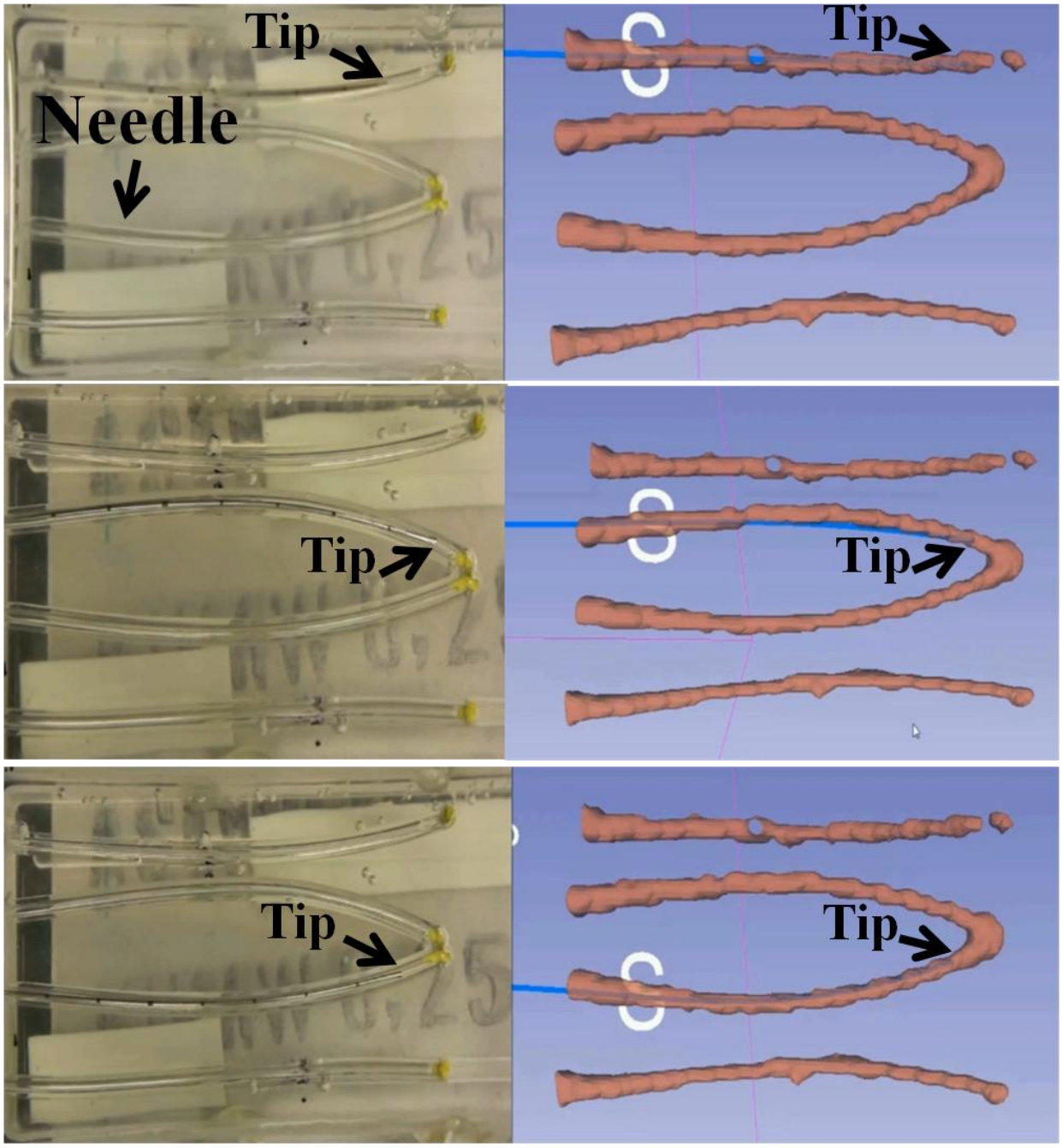

Figure 5.17: Needle navigation through various tubes of a gel phantom. The reconstructed needle shapes (shown in blue color) were well inside the segmented tubes.

An in-vitro experiment with the gel phantom was also performed using the Aurora EMTS system. Similar to all the previous experiments, as a first step we applied point-based registration between the physical space and MRI image space using the same set of multi-modality radiology markers. The calculated mean RMS error was 0.81 ± 0.13 mm. Then we imported the 3D

segmented model of the gel phantom in Slicer. Needle navigation through the tubes of the gel phantom was then performed. Experimental results shown in 5.18 illustrate that the tip of the needle model in Slicer was well inside the segmented tubes during the navigation.

However, navigation through two of the tubes was not accomplished, because of the inside blockage of the tube by the PDMS mixture and also for the larger diameter of the 18G EM needle (compare to 20G FBG needle). Therefore, the end point of the other two tubes was used as the targets. The average TRE error for this experiment was 1.06 ± 0.11 mm.

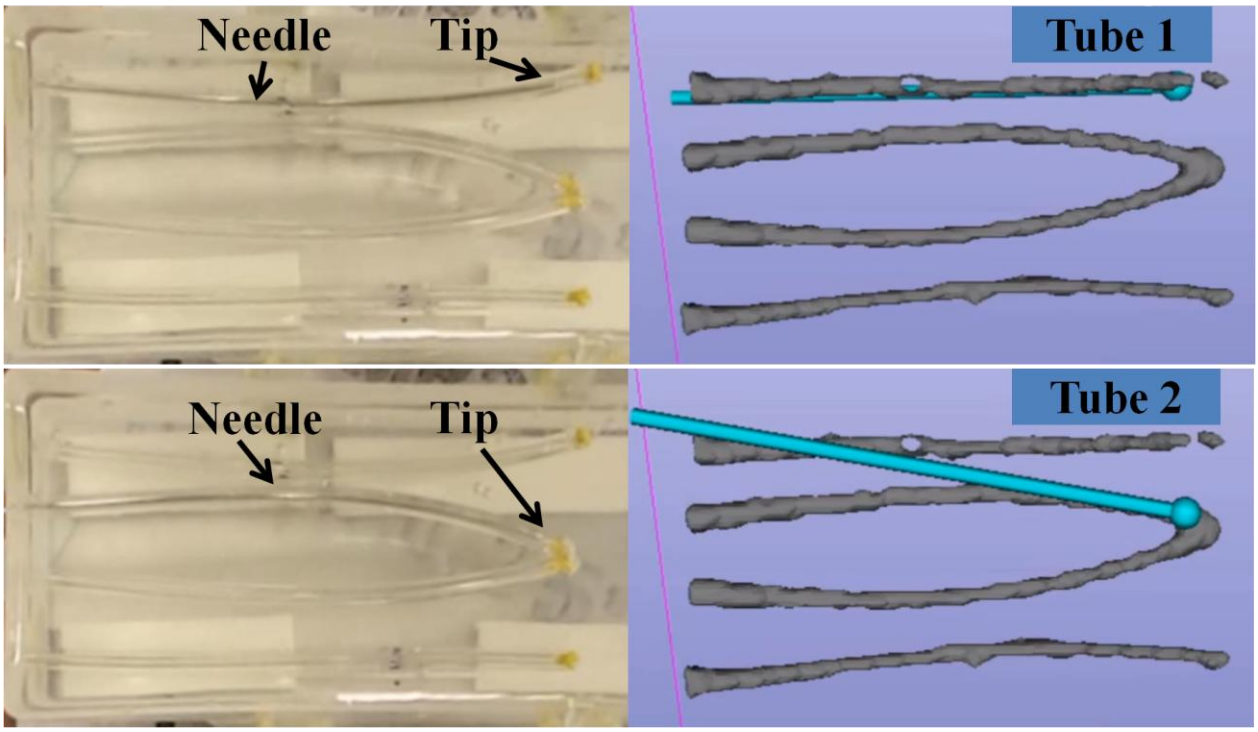

Figure 5.18: Needle navigation using the Aurora EMTS through different tubes of a gel phantom.

5.6 Summary

In this chapter, we first showed the results of the proposed calibration method, followed by a representation of the reconstructed 3D needle shape within the Slicer software interface. We performed a series of in-vitro experiments to validate our FBG-based tracking system. The results obtained from each of the experiments were shown in detail along with the overall registration accuracy. In order to compare the tracking accuracy to the state of the art tracking systems, we integrated an NDI Aurora EMTS with our experimental setup and performed a series of in-vitro experiments. The results obtained from the experiments with the NDI Aurora EMTS were shown

to compare favorably with the results achieved by our FBG-based tracking system. In the next section, we will discuss and analyze these results and evaluate the system's limitations.

CHAPTER 6 DISCUSSION

RFA has proven to be an effective percutaneous treatment modality for unresectable hepatic tumors in a non-transplant candidate. Typically, a needle is directly inserted into the tumor, which in turn delivers radiofrequency energy to cause necrosis of the tumors. Therefore, accurate needle tip placement is essential in RFA of liver tumors. In practice however, it is challenging due to various factors such as inhomogeneity of the tissue, needle insertion depth and asymmetry of the needle tip that cause bending of the needle. As a solution, an intraoperative US image is used to guide the needle tip to the target that is defined in the preoperative CT or MRI diagnostic image. However, visualization of the target and the needle under US image guidance is problematic due to the limited spatial resolution of the US image. Also, thermal ablation generates micro-bubbles and shadows that interfere with the visualization. CT can be used as an alternative, but generates ionizing radiation to the patient as well as to the clinical operators (e.g. the interventional radiologists). On the other hand, needle navigation under MRI guidance is a potential alternative due to its angiographic sequences and the ability to freely select the slice angulations in the needle plane. Moreover, it can also be used to monitor RFA-induced heating and thermal damage of the cancerous tissues. However, the resolution of the image generated from angiographic sequences is low compared to that of the diagnostic image obtained from the regular MRI imaging sequences. Another major challenge is the scarcity of MRI-compatible instruments.

This thesis focuse on the 3D shape reconstruction of an entire needle in real-time using measurement from MR-compatible FBG sensors. The goal was to develop a tracking system that could safely track the needle's and the 3D shape in a high EM field during MRI-guided interventions for liver tumors. We performed a series of in-vitro experiments with our FBG-based tracking system. To compare the tracking accuracy of our system, we performed similar experiments with an Aurora EMTS. In section 6.1, we analyze the in-vitro experimental results presented in chapter 5. In section 6.2, we discuss the results obtained from other research groups who used a similar shape sensing technology to reconstruct the needle shape. Section 6.3 demonstrates the MRI compatibility of our FBG sensors. Then, the measurement of the maximum curvature that is supported by our fiber system is shown in section 6.4. Finally, we state the limitations of our system in section 6.5, followed by the summary in section 6.6.

6.1 Comparing FBG-based tracking with Aurora EMTS

In our first in-vitro experiment, we tested the tip tracking accuracy of our FBG tracking system in two different orthogonal planes of the needle axis where the TRE was 0.96 ± 0.05 mm and 0.95 ± 0.06 mm for tip deflection of up to ±10.68 mm in the xy and xz planes, respectively. The corresponding error for the NDI Aurora system was comparatively lower. The error was between 0.54~0.83 mm and 0.51~0.84 mm for a tip deflection from ±2.67 to ±10.68 mm in the xy and xz planes, respectively. By analyzing the RMS error distribution for different tip deflections, we can see that as the tip deflection decreases the error of FBG tracking also decreases. On the other hand, the error of the Aurora system was similar for different tip deflections.

However, in this experiment, the FRE of the FBG tracking system (i.e. 0.43 ± 0.12 mm) was similar to that of Aurora EMTS (i.e. 0.42 ± 0.10 mm). It is important to mention here that, during the registration procedure for both systems, the needle was not bent to collect the fiducial markers' position. We utilized our robotic system that translated the needle base to position the needle tip at the fiducials' location without inducing any bending. Since fiducial localization error due to the bending of the needle was avoided, we achieved a similar FRE for both systems.

Results obtained from the second in-vitro experiment with phantom-2 showed similar error distributions to the previous experiment for the FBG-based tracking system. In this experiment, we were interested in deflecting the needle tip further up to 16.83 mm from its initial non-bending position. For tip deflections of 2.35, 3.37, 8.05, 8.27, 14.51, 16.67 and 16.83 mm from the initial non-bending position, the corresponding mean tracking errors were 0.52, 0.59, 0.67, 0.70, 1.00, 1.05 and 1.05 mm, respectively (as shown in Figure 5.14). We can interpret that the error increased linearly as the tip deflection increased. On the other hand, the corresponding mean tracking errors for the Aurora system were 0.72, 0.71, 0.67, 0.75, 0.82, 0.78 and 0.76 mm, respectively (as shown in Figure 5.16). The errors were similar for all of the tip deflections and the small differences in the TRE values may be due to random jitter noise in the Aurora system.

However, the FRE of the Aurora system for this experiment with phantom-2 was comparatively higher than that of our FBG-based tracking system, 0.58 ± 0.09 mm and 0.52 ± 0.11 mm, respectively. This is possibly due to the fiducial localization error caused by phantom-2, as the holes created from the 3D printer were not smooth and accurate enough (see Figure 6.1). White arrows indicate the distorted holes in Figure 6.1(a).

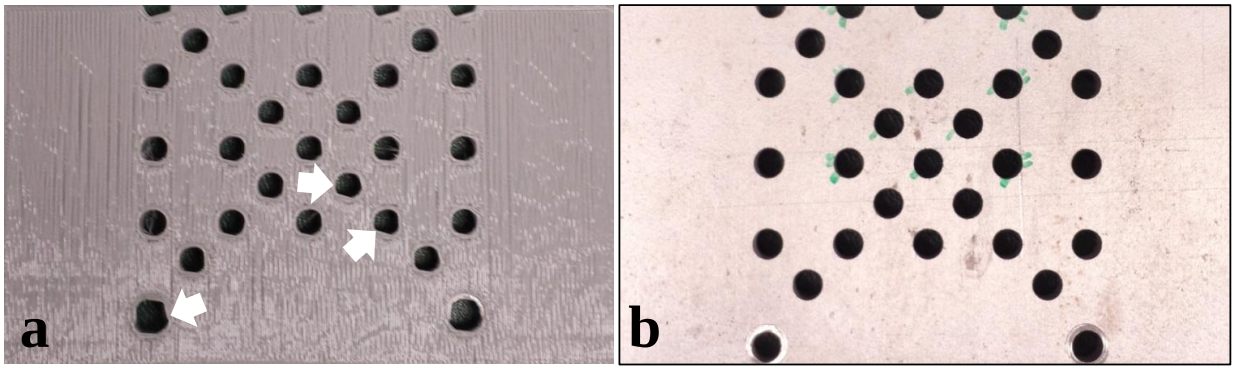

Figure 6.1: (a) The plastic model of the phantom-2 where white arrows show the distorted holes. (b) 3D model of the phantom-2.

Unlike the previous two experiments where the needle tip was deflected in free-space, the last in-vitro experiment was done inside a gel phantom. The tubular structures of the gel phantom forced the needle to bend with defined paths while guiding the needle through them. The experimental results showed that our FBG-based tracking system successfully tracked the needle tip with its 3D reconstructed shape. The computed FRE was similar for the two systems, with an RMS error of 0.81 ± 0.11 mm and 0.84 ± 0.12 mm for the Aurora EMTS and our FBG-based tracking system, respectively. The FRE of both systems in this experiment were relatively higher than that of the previous two experiments. Selecting the fiducial position in the planar phantom model was comparatively easier than choosing the fiducials in the MRI image. The fiducial localization error in the MRI image may have been large, thus degrading the registration accuracy. As a result, the TRE was also larger for both tracking techniques in this experiment.

Both the qualitative and quantitative results obtained from all the in-vitro experiments indicate the potential feasibility of FBG-based tracking to follow the needle during RFA of liver tumors. The overall maximum tip position error was approximately 1 mm for tip deflections of up to 16.82 mm. The measurement obtained from the two camera images also confirmed the high accuracy of our reconstructed needle shape. It would be interesting to compare the shape of the reconstructed needle from both tracking systems; Unfortunately, we could not do this with the needle from NDI as it did not have any sensor along its shaft. The sole EM sensor at the tip of the needle was connected by wire to the system control unit (SCU) of Aurora. In order to reconstruct the shape of the entire needle, a series of EM sensors should be placed along the needle shaft. Cables from all of the sensors have to pass through the needle, which might increase the diameter

of the needle and make the needle unsuitable for percutaneous interventions. Also, we noticed that the tip of the needle was not tracked for some orientations of the needle with respect to the field generator. Figure 6.2(a) shows one of the needle orientations (close to perpendicular to the field generator) for which the Aurora system did not track the tip. Even though the tip was well inside the working volume, the NDI tool could not represent the tip position due to a bad fit, as shown in Figure 6.2(b).

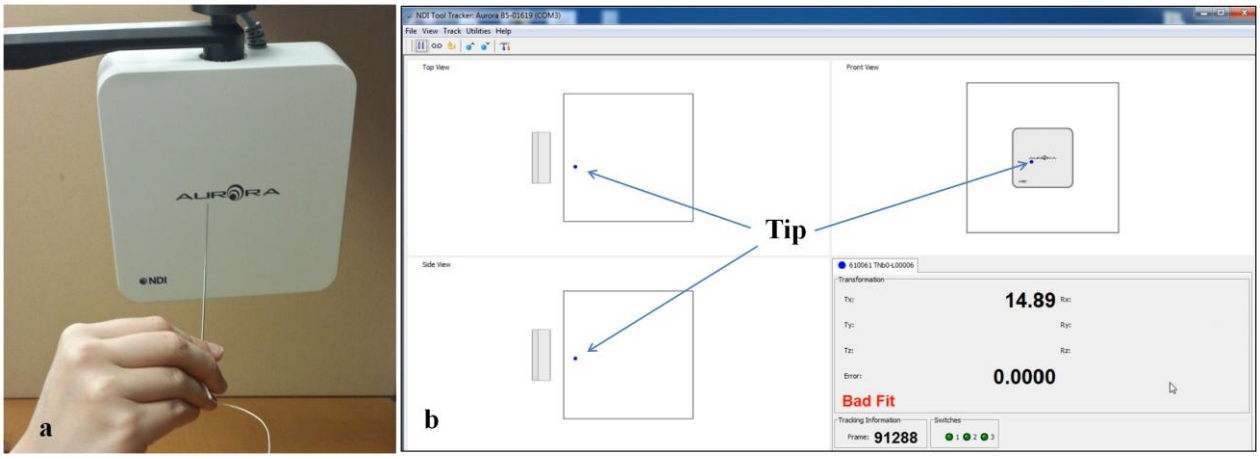

Figure 6.2: (a) A needle orientation for which the tip was not tracked by the Aurora system, (b) the tip position (indicated by arrows) is shown well inside the working volume in NDI tool tracker interface.

Compared to the EM-based tracking system, the FBG-based tracking system is smaller in size (see Figure 6.3). Also, the field generator of an EMTS must be placed close to the target and arranged in such a way that the needle tip can be tracked for any orientation of the needle inside the working volume. The placement of the field generator sometimes limits the choice of orientation for needle insertion.

Figure 6.3: Side-by-side physical dimension comparison between a Deminsys© interrogator and an Aurora field generator with its system control unit.

6.2 Comparison with other shape sensing methods

There are other groups working on the shape sensing methods to reconstruct the needle profile [80-82]. Among them, the most promising results were claimed by Park et al. They reported RMS errors of 0.28 mm and 0.38 mm for tip deflections of ±15 mm. The main reason behind their better result may be because of the choice of the optimal position of the sensors along the needle. For different amounts of tip deflection, they calculated the sensors' optimal position that generated the least amount of error to estimate the tip position.

However, it is important to understand what the tip accuracy means in our work. Similar to Park et al.'s work, all the other research works show the tip accuracy in the needle space only. They did not perform any registration procedure to measure the tip accuracy with respect to the target. To the best of our knowledge, this work is the first to show the errors following the typical image guidance procedural steps. We performed a point-based registration and then applied the

calculated registration matrix on the reconstructed needle shape to overlay it on the targeted phantom. After that, we navigated the needle to place the tip to the target defined on the phantom. Finally, the RMS distance between the actual target and the estimated tip position was defined as the tracking error.

In our needle configuration, we glued the three fibers together with a UV curing glue and then inserted the combined fiber into a 20G needle. The diameter of the combined fiber might not be uniform along the needle shaft. Hence there could be a small gap between the needle's inner body and the fiber at some points. As a result, during the calibration procedure, while the needle shaft was bent by deflecting the tip, the fiber inside might not have bent accordingly. This could have contributed cause some error in our experiments.

Furthermore, it's hard to compare the tip position accuracy for different tip deflections among previous shape sensing studies. This is because the factors considered in prior research works are different in many ways: the number of sensors used per fiber, the length of the needle and the sensor placement along the needle and calibration setup. All previous works are set up in the laboratory and none have demonstrated a comparison study of the tracking technologies. In this thesis work, we experimentally compared the accuracy of our optical shape sensing based tracking system with a state of the art tracking system, the NDI Aurora EMTS.

6.3 MRI compatibility

FBG sensors are immune to electromagnetic interference. We performed an experiment to verify the MRI compatibility of the FBG sensors of our fiber system. The experiment was done inside the bore of a 1.5T MRI scanner (see Figure 6.4). At first, we fixed the fiber on a tray by keeping it straight, so that there was no bending along the fiber. Then we took measurements from all the FBG sensors outside of the MRI scanning room. We recorded the measurements for at least 5 seconds.

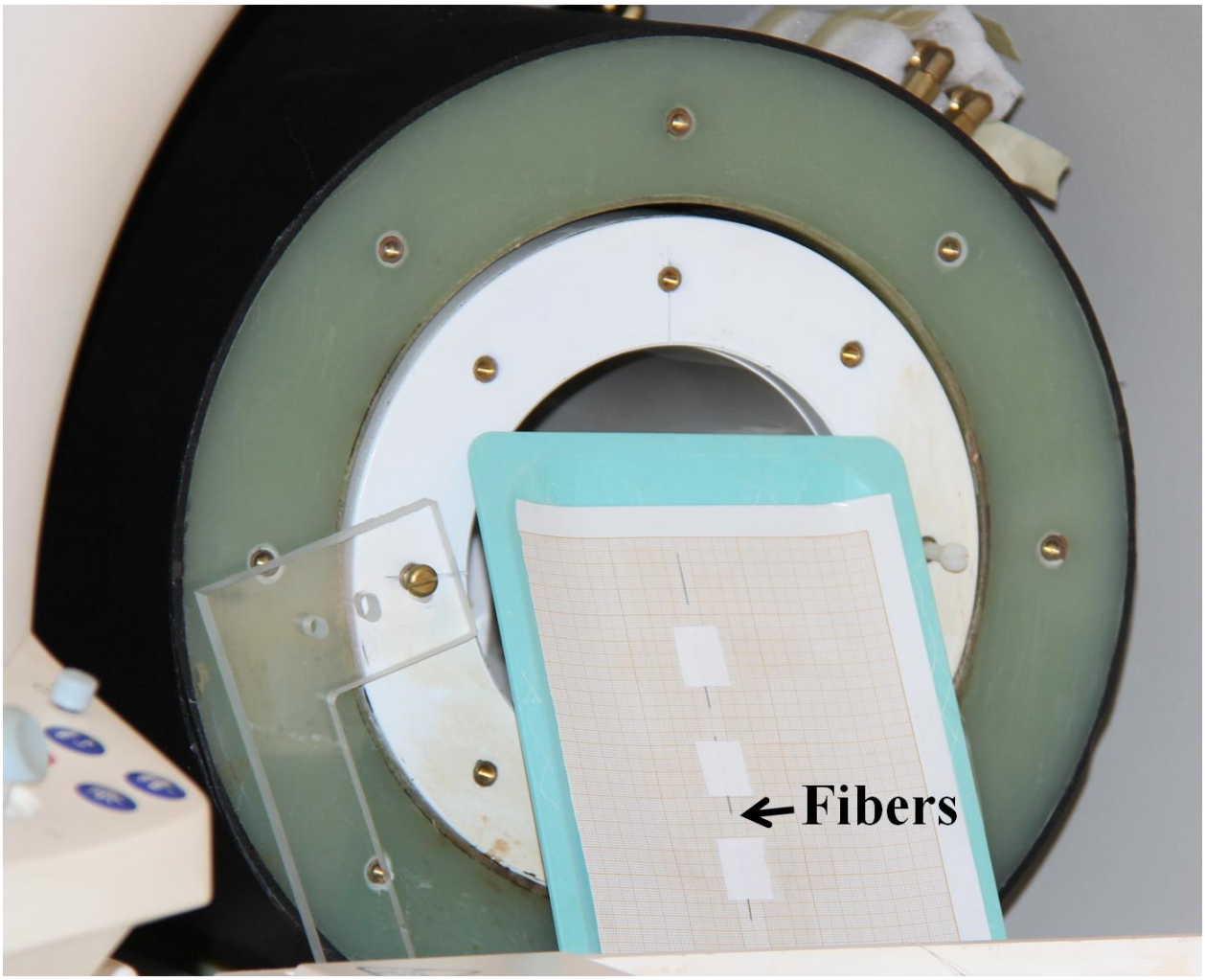

Figure 6.4: Image shows the fibers placed inside the bore of a 1.5T MRI scanner.

After that, only the fiber was placed inside the MRI bore. The interrogator and the laptop were positioned far from the MRI scanner. Then, we recorded the sensor data for another 5 seconds. Figure 6.5 shows the calculated wavelength-shift measurement of all the FBG sensors both inside and outside the MRI scanner. By comparing the results, we can conclude that there were no significant changes in the measured wavelength-shift data generated within the MRI magnetic field. The small amount of wavelength-shift for all the sensors, which was visible in both scenarios, may be due to the air flow generated by the cooling fan of the electronic machinery (e.g. laptop) or any nearby mechanical vibrations. This is because the FBG sensors are very sensitive to strain variations and can sense strain at the micron scale.

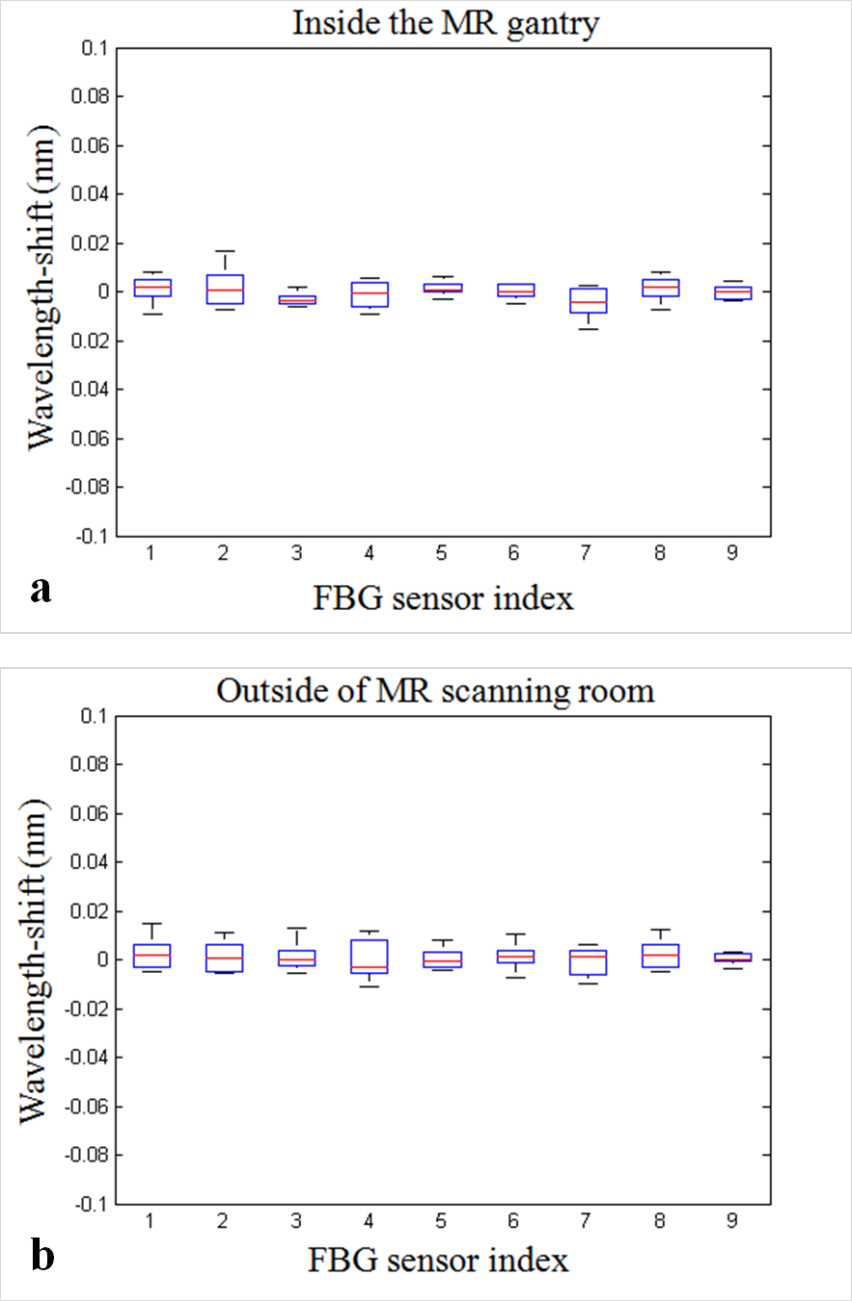

Figure 6.5: The calculated strain of all the FBG sensors both (a) inside and (b) outside the MRI.

6.4 Maximum curvature supported by our fiber system

FBG sensors are usually made of glass and are therefore fairly fragile which limits their its flexibility. For the shape sensing method, which uses three fibers that are glued together (as we did in our work), this further reduces flexibility. We performed an empirical test to verify the maximum curvature (i.e. minimum curvature radius) that our fibers can support. We used a

cylindrical cone shaped plastic object for this experiment (see Figure 6.6). The diameter of this object varies gradually from one end to the other, ranging from 6.2 mm to 30 mm.

Figure 6.6: A cylindrical cone shaped plastic object with an inner diameter ranging from 6.2 mm to 30 mm.

During the experiment, the fibers were bent around the perimeter of the plastic object to make a complete loop and the diameter of cross section was measured (see Figure 6.7). We started from the end of the plastic object that had the higher diameter (30mm). Each time we completed the measurement, we moved the fiber to the next smaller diameter region and repeated these steps until the fibers broke. According to this experiment, our fibers supported a maximum curvature of ~0.125 mm^{-1} (i.e. minimum curvature radius of ~8 mm).

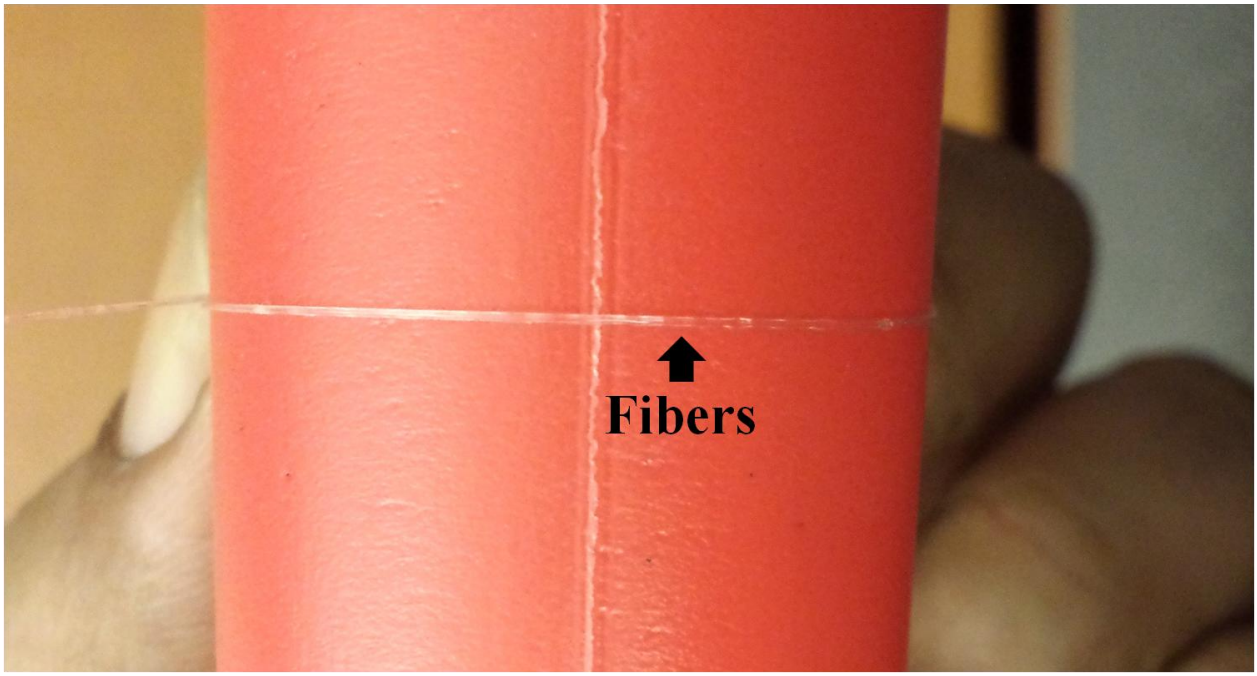

Figure 6.7: Image shows the curvature measuring experiment where the fibers were wrapped around the plastic object.

6.5 Limitations

One of the limitations of our FBG-based tracking system is that we cannot steer the needle tip in a pre-defined direction. We did not implement needle steering as it was considered out of the scope of this thesis work. As a solution, we fabricated a gel phantom having some tubular structures. These structures allowed us to prepare the trajectory plans in advance. Also, our gel phantom, as well as the planar phantoms, ensured allowed the experiments to be performed in a controlled environment and in a repeatable manner.

In contrast to the Aurora EMTS that can track the tip for any needle orientation, in our experimental setup, we cannot change the needle orientation. Since the needle profile is represented with respect to the base of the needle, all movements from the base should be tracked. By using the movement information of the needle base, we can represent the needle profile in a global coordinate space. The robotic translation system in our experimental setup permits 3D translation of the needle base. It does not allow any angular movement of the needle.

Furthermore, even though our fiber system and the gel phantom are MRI compatible, the calibration setup is not supported by the MRI as it is completely made of metal. For this reason, we could not perform the in-vitro experiments inside the MRI scanner.

6.6 Summary

By analyzing and interpreting the results obtained from the in-vitro experiments, we can say that the accuracy of our FBG-based tracking system is suitable for needle tip detection in RFA of liver tumors. The accuracy of our tracking system is comparable to that of an NDI Aurora EMTS. We believe that the error linked to tip bending is mainly caused by the misalignment of the three FBGs in a single axial plane and also the gap between the needle's inner boundary and the fibers inside. In addition, we think that an optimal placement of the sensors along the needle shaft can reduce the error by better approximating the shape of the needle. Finally, the experimental results prove that our fiber system is MRI compatible and flexible enough to support the needle bending required for RFA procedures in the liver.

CHAPTER 7 CONCLUSION

In this thesis, we developed a 3D shape reconstruction technique of needles using FBG sensor measurements that made it feasible for tracking the tip and the shape of a needle inside a high EM field during MRI-guided needle interventions in the liver. Towards this end, three glass fibers equipped with three FBGs were glued together maintaining an angular distance of 120° among the fibers which were then incorporated into a 20G needle. We presented a simple and fast calibration procedure to get the strain at the sensor location from the measured wavelength-shift values. The entire 3D shape of a needle was reconstructed based on polynomial fitting of the calculated strain measurements. For visualization, we built a module in 3D Slicer that represented the 3D shape of the needle in real-time. A point-based registration algorithm was applied to co-align the FBG tracking space with the preoperative MRI image space. We validated our FBG-based needle navigation by doing a series of in-vitro experiments. The measurement information obtained from the camera images ensured the shape accuracy of our reconstructed needle. Results obtained from a series of in-vitro validation experiments demonstrated needle tip tracking errors of 1.05 ± 0.08 mm for a deflection of the needle tip of up to 16.82 mm on a ground-truth model, which is appropriate for applications such as RFA of liver tumors. Furthermore, by performing identical experiments with an NDI Aurora EMTS that compared the tracking results (i.e. FRE and TRE), the feasibility of the FBG-based tracking system for MR guided interventions was verified. Positioning error is attributed to the misalignment of the FBG sensors in a single axial plane and the gap between the needle's inner boundary and the fibers inside.

Finally, even though the shape sensing technology based on FBG sensors shows the ability to track the needle tip in real-time, it still cannot be used solely during intervention without a pre-intervention imaging modality. This is because a soft-tissue organ such as the liver deforms significantly during an intervention due to patient's breathing and due to the patient being under the effect of anesthesia and positioned differently on the surgical table. This deformation is not compensated by the FBG tracking system. Therefore, a fast imaging system is a must to know the exact position of the target. The imaging system also can confirm the position of the needle with respect to the target. MRI is the ideal imaging modality to visualize small tumor as it has high soft-tissue contrast and high spatial resolution. Therefore, a preoperative MRI scan with an imaging sequence can be acquired just before starting the needle insertion. Next, angiographic

MRI image sequences can be used as an intraoperative imaging modality as they have the ability to provide fast image information. Since FBG is immune to electromagnetic interference, it is possible to perform FBG-based needle interventions under MRI guidance. While the low frequency MRI image can accurately visualize the target, the high frequency FBG-based tracking system can localize the needle tip position in real-time. Additionally, FBG-based shape sensing can define the MRI image plane automatically in real-time.

In this project, needle steering was not considered. In future work, we would like to integrate a robotic steering system with our tracking system. This steering system would allow accurate control of the tip placement during insertion. The operator could then adjust the position and orientation of the tip intra-procedurally in case there is any change to be made to the needle's trajectory. Thus, retraction and reinsertion of the needle could be avoided. In addition, it might be possible to reach multiple targeted locations by a single needle insertion.

Unlike existing tracking systems, the proposed FBG-based tracking system is the first tracking technology which is compatible with MRI and therefore, this technique can have a strong impact on a number of MR-compatible procedures including MR-guided hyperthermia, MRI-guided biopsies and therapies (e.g. prostate biopsy) and MR navigation of nanoparticles inside the capillary network. However, application is fairly recent and was performed only in a research setting. Therefore, extensive research and thorough in-vivo experiments are required to demonstrate its viability for clinical adoption.

BIBLIOGRAPHY

[1] J. Ferlay, H. R. Shin, F. Bray, D. Forman, C. Mathers, and D. M. Parkin, "Estimates of worldwide burden of cancer in 2008: GLOBOCAN 2008," *Int J Cancer,* vol. 127, pp. 2893-917, Dec 15 2010.

[2] "Special topic: Predictions of the future burden of cancer in Canada," in *Canadian Cancer Society*, Canadian Cancer Society's Advisory, Committee on Cancer Statistics, and Canadian Cancer Statistics 2015, Eds., ed. Toronto, ON, 2015.

[3] Canadian Cancer Society. (2015, 31 August). *Media backgrounder #1: Predictions of the future burden of cancer in Canada*. Available: http://www.cancer.ca/en/about-us/for-media/media-releases/national/2015/backgrounder-1-cancer-statistics/?region=on

[4] D. J. Bentrem, R. P. Dematteo, and L. H. Blumgart, "Surgical therapy for metastatic disease to the liver," *Annu Rev Med,* vol. 56, pp. 139-56, 2005.

[5] T. J. Vogl, P. Farshid, N. N. Naguib, A. Darvishi, B. Bazrafshan, E. Mbalisike, *et al.*, "Thermal ablation of liver metastases from colorectal cancer: radiofrequency, microwave and laser ablation therapies," *Radiol Med,* vol. 119, pp. 451-61, Jul 2014.

[6] T. H. Chen, C. J. Chen, M. F. Yen, S. N. Lu, C. A. Sun, G. T. Huang, *et al.*, "Ultrasound screening and risk factors for death from hepatocellular carcinoma in a high risk group in Taiwan," *Int J Cancer,* vol. 98, pp. 257-61, Mar 10 2002.

[7] C. K. Kim, J. H. Lim, and W. J. Lee, "Detection of hepatocellular carcinomas and dysplastic nodules in cirrhotic liver: accuracy of ultrasonography in transplant patients," *J Ultrasound Med,* vol. 20, pp. 99-104, Feb 2001.

[8] N. V. Tsekos, A. Khanicheh, E. Christoforou, and C. Mavroidis, "Magnetic resonance-compatible robotic and mechatronics systems for image-guided interventions and rehabilitation: a review study," *Annu Rev Biomed Eng,* vol. 9, pp. 351-87, 2007.

[9] S. J. Phee and K. Yang, "Interventional navigation systems for treatment of unresectable liver tumor," *Med Biol Eng Comput,* vol. 48, pp. 103-11, Feb 2010.

[10] N. Abolhassani, R. P., and M. Mehrdad, "Needle insertion into soft tissue: A survey," *Medical engineering & physics,* vol. 29, pp. 413-431, 2007.

[11] G. J. Tortora and B. H. Derrickson, *Principles of Anatomy and Physiology*, 13 ed., 2011.

[12] A. K. Siriwardena, J. M. Mason, S. Mullamitha, H. C. Hancock, and S. Jegatheeswaran, "Management of colorectal cancer presenting with synchronous liver metastases," *Nat Rev Clin Oncol,* vol. 11, pp. 446-59, Aug 2014.

[13] C. Couinaud, "Liver anatomy: portal (and suprahepatic) or biliary segmentation," *Dig Surg,* vol. 16, pp. 459-67, 1999.

[14] R. Berne and M. Levy, "Special Circulations," *Physiology. 4th ed. St. Louis: Mosby,* 1998.

[15] H. Gray and P. L. Williams, *Grey's Anatomy*, 38 ed. New York, Churchill Livingstone., 1995.

[16] K. Schutte, J. Bornschein, and P. Malfertheiner, "Hepatocellular Carcinoma - Epidemiological Trends and Risk Factors," *Digestive Diseases,* vol. 27, pp. 80-92, 2009.

[17] (2006). *World Health Organization*. Available: http://www.who.int/mediacentre/factsheets/fs297/en/

[18] A. P. Venook, C. Papandreou, J. Furuse, and L. L. de Guevara, "The incidence and epidemiology of hepatocellular carcinoma: a global and regional perspective," *Oncologist,* vol. 15 Suppl 4, pp. 5-13, 2010.

[19] N. F. Vinay Kumar, Abul Abbas, *Robbins and Cotran pathologic basis of disease*, 7 ed.: Elsevier Saunders, 2003.

[20] W.-Y. Lau and E. Lai, "Hepatocellular carcinoma: current management and recent advances," *Hepatobiliary & pancreatic diseases international: HBPD INT,* vol. 7, pp. 237-257, 2008.

[21] S. A. Shah, R. Haddad, W. Al-Sukhni, R. D. Kim, P. D. Greig, D. R. Grant, *et al.*, "Surgical resection of hepatic and pulmonary metastases from colorectal carcinoma," *J Am Coll Surg,* vol. 202, pp. 468-75, Mar 2006.

[22] S. A. Curley, F. Izzo, P. Delrio, L. M. Ellis, J. Granchi, P. Vallone, *et al.*, "Radiofrequency Ablation of Unresectable Primary and Metastatic Hepatic Malignancies," *Annals of Surgery,* vol. 230, p. 1, 1999.

[23] E. K. Abdalla, J.-N. Vauthey, L. M. Ellis, V. Ellis, R. Pollock, K. R. Broglio, *et al.*, "Recurrence and Outcomes Following Hepatic Resection, Radiofrequency Ablation, and Combined Resection/Ablation for Colorectal Liver Metastases," *Annals of Surgery,* vol. 239, pp. 818-827, 2004.

[24] G. Marín-Hargreaves, D. Azoulay, and H. Bismuth, "Hepatocellular carcinoma: surgical indications and results," *Critical Reviews in Oncology/Hematology,* vol. 47, pp. 13-27, 2003.

[25] L. De Carlis, A. Giacomoni, V. Pirotta, A. Lauterio, A. O. Slim, C. Sammartino, *et al.*, "Surgical treatment of hepatocellular cancer in the era of hepatic transplantation," *Journal of the American College of Surgeons,* vol. 196, pp. 887-897, 2003.

[26] R. T. Poon, S. T. Fan, F. H. Tsang, and J. Wong, "Locoregional therapies for hepatocellular carcinoma: a critical review from the surgeon's perspective," *Ann Surg,* vol. 235, pp. 466-86, Apr 2002.

[27] M. Ebara, S. Okabe, K. Kita, N. Sugiura, H. Fukuda, M. Yoshikawa, *et al.*, "Percutaneous ethanol injection for small hepatocellular carcinoma: therapeutic efficacy based on 20-year observation," *J Hepatol,* vol. 43, pp. 458-64, Sep 2005.

[28] C. J. Simon, D. E. Dupuy, and W. W. Mayo-Smith, "Microwave ablation: principles and applications," *Radiographics,* vol. 25 Suppl 1, pp. S69-83, Oct 2005.

[29] S. Shimada, M. Hirota, T. Beppu, T. Matsuda, N. Hayashi, S. Tashima, *et al.*, "Complications and management of microwave coagulation therapy for primary and metastatic liver tumors," *Surg Today,* vol. 28, pp. 1130-7, 1998.

[30] D. A. Iannitti, R. C. Martin, C. J. Simon, W. W. Hope, W. L. Newcomb, K. M. McMasters, *et al.*, "Hepatic tumor ablation with clustered microwave antennae: the US Phase II trial," *HPB (Oxford),* vol. 9, pp. 120-4, 2007.

[31] J. K. Seifert and D. L. Morris, "World Survey on the Complications of Hepatic and Prostate Cryotherapy," *World Journal of Surgery,* vol. 23, pp. 109-114, 1999.

[32] J. K. Seifert and D. L. Morris, "Prognostic factors after cryotherapy for hepatic metastases from colorectal cancer," *Ann Surg,* vol. 228, pp. 201-8, Aug 1998.

[33] J. Seifert, T. Junginger, and D. Morris, "A collective review of the world literature on hepatic cryotherapy," *Journal of the Royal College of Surgeons of Edinburgh,* vol. 43, pp. 141-154, 1998.

[34] G. Rong, W. Bai, Z. Dong, C. Wang, Y. Lu, Z. Zeng, *et al.*, "Long-term outcomes of percutaneous cryoablation for patients with hepatocellular carcinoma within Milan criteria," *PloS one,* vol. 10, p. e0123065, 2015.

[35] L. M. Ellis, S. A. Curley, and K. K. Tanabe, *Radiofrequency Ablation for Cancer: Current indications, techniques, and outcomes*: Springer Science & Business Media, 2003.

[36] S. A. Curley, K. E. Stuart, J. M. Schwartz, and R. Carithers, "Nonsurgical therapies for localized hepatocellular carcinoma: Radiofrequency ablation, percutaneous ethanol injection, thermal ablation, and cryoablation," *UpToDate, Basow, DS (Ed), UpToDate, Waltham, MA,* 2015.

[37] R. Tateishi, S. Shiina, T. Teratani, S. Obi, S. Sato, Y. Koike, *et al.*, "Percutaneous radiofrequency ablation for hepatocellular carcinoma," *Cancer,* vol. 103, pp. 1201-1209, 2005.

[38] D. Choi, H. K. Lim, H. Rhim, Y.-s. Kim, W. J. Lee, S. W. Paik, *et al.*, "Percutaneous radiofrequency ablation for early-stage hepatocellular carcinoma as a first-line treatment: long-term results and prognostic factors in a large single-institution series," *European radiology,* vol. 17, pp. 684-692, 2007.

[39] S. Arii, Y. Yamaoka, S. Futagawa, K. Inoue, K. Kobayashi, M. Kojiro, *et al.*, "Results of surgical and nonsurgical treatment for small-sized hepatocellular carcinomas: A retrospective and nationwide survey in Japan," *Hepatology,* vol. 32, pp. 1224-1229, 2000.

[40] P. Liang, B. Dong, X. Yu, D. Yu, Y. Wang, L. Feng, *et al.*, "Prognostic Factors for Survival in Patients with Hepatocellular Carcinoma after Percutaneous Microwave Ablation 1," *Radiology,* vol. 235, pp. 299-307, 2005.

[41] M. P. S. Boeti, I. Popescu, and R. Grigorie, *Laparoscopic radiofrequency ablation of liver tumors*: INTECH Open Access Publisher, 2013.

[42] T. Reichl, "Advanced Hybrid Tracking and Navigation for Computer-Assisted Interventions," Technische Universität München, 2013.

[43] A. J. Herline, J. D. Stefansic, J. P. Debelak, S. L. Hartmann, C. W. Pinson, R. L. Galloway, *et al.*, "Image-guided surgery: preliminary feasibility studies of frameless stereotactic liver surgery," *Arch Surg,* vol. 134, pp. 644-9; discussion 649-50, Jun 1999.

[44] D. M. Cash, T. K. Sinha, W. C. Chapman, T. H., B. M. Dawant, R. L. Galloway, *et al.*, "Incorporation of a laser range scanner into image-guided liver surgery: Surface acquisition, registration, and tracking," *Medical Physics,* vol. 30, p. 1671, 2003.

[45] D. M. Cash, M. I. Miga, S. C. Glasgow, B. M. Dawant, L. W. Clements, Z. Cao, *et al.*, "Concepts and preliminary data toward the realization of image-guided liver surgery," *J Gastrointest Surg,* vol. 11, pp. 844-59, Jul 2007.

[46] T. Lange, N. Papenberg, S. Heldmann, J. Modersitzki, B. Fischer, H. Lamecker, *et al.*, "3D ultrasound-CT registration of the liver using combined landmark-intensity information," *International journal of computer assisted radiology and surgery,* vol. 4, pp. 79-88, 2009.

[47] M. Peterhans, A. vom Berg, B. Dagon, D. Inderbitzin, C. Baur, D. Candinas, *et al.*, "A navigation system for open liver surgery: design, workflow and first clinical applications," *Int J Med Robot,* vol. 7, pp. 7-16, Mar 2011.

[48] M. Markert, S. Weber, and T. C. Lueth, "Manual registration of ultrasound with CT/planning data for hepatic surgery," *Stud Health Technol Inform,* vol. 125, pp. 319-21, 2007.

[49] T. Lango, G. A. Tangen, R. Marvik, B. Ystgaard, Y. Yavuz, J. H. Kaspersen, *et al.*, "Navigation in laparoscopy--prototype research platform for improved image-guided surgery," *Minim Invasive Ther Allied Technol,* vol. 17, pp. 17-33, 2008.

[50] T. Lango, S. Vijayan, A. Rethy, C. Vapenstad, O. V. Solberg, R. Marvik, *et al.*, "Navigated laparoscopic ultrasound in abdominal soft tissue surgery: technological overview and perspectives," *Int J Comput Assist Radiol Surg,* vol. 7, pp. 585-99, Jul 2012.

[51] F. M., M. T., H. S. M., and N. N., "Registration-free laparoscope augmentation for intra-operative liver resection planning," *International Society for Optics and Photonics in Medical Imaging,* pp. 650 915–650 915, 2007.

[52] *NDI*. Available: http://www.ndigital.com/medical/polarisfamily-techspecs.php

[53] S. R. Kirsch, H. R. Schild, and C. J. Schilling, "Gain factor and position determination system," ed: Google Patents, 2003.

[54] T. Peters and K. Cleary, *Image-guided interventions: technology and applications*: Springer Science & Business Media, 2008.

[55] A. M. Franz, T. Haidegger, W. Birkfellner, K. Cleary, T. M. Peters, and L. Maier-Hein, "Electromagnetic tracking in medicine--a review of technology, validation, and applications," *IEEE Trans Med Imaging,* vol. 33, pp. 1702-25, Aug 2014.

[56] T. Penzkofer, P. Bruners, P. Isfort, F. Schoth, R. W. Gunther, T. Schmitz-Rode, *et al.*, "Free-hand CT-based electromagnetically guided interventions: accuracy, efficiency and dose usage," *Minim Invasive Ther Allied Technol,* vol. 20, pp. 226-33, Jul 2011.

[57] J. Krucker, S. Xu, A. Venkatesan, J. K. Locklin, H. Amalou, N. Glossop, *et al.*, "Clinical utility of real-time fusion guidance for biopsy and ablation," *J Vasc Interv Radiol,* vol. 22, pp. 515-24, Apr 2011.

[58] A. M. Venkatesan, S. Kadoury, N. Abi-Jaoudeh, E. B. Levy, R. Maass-Moreno, J. Krucker, *et al.*, "Real-time FDG PET Guidance during Biopsies and Radiofrequency

Ablation Using Multimodality Fusion with Electromagnetic Navigation," *Radiology,* vol. 260, pp. 848-856, Sep 2011.

[59] D. Sindram, R. Z. Swan, K. N. Lau, I. H. McKillop, D. A. Iannitti, and J. B. Martinie, "Real-time three-dimensional guided ultrasound targeting system for microwave ablation of liver tumours: a human pilot study," *HPB (Oxford),* vol. 13, pp. 185-91, Mar 2011.

[60] M. J. Wallace, S. Gupta, and M. E. Hicks, "Out-of-plane computed-tomography-guided biopsy using a magnetic-field-based navigation system," *Cardiovasc Intervent Radiol,* vol. 29, pp. 108-13, Jan-Feb 2006.

[61] N. Abi-Jaoudeh, J. Kruecker, S. Kadoury, H. Kobeiter, A. M. Venkatesan, E. Levy, *et al.*, "Multimodality image fusion-guided procedures: technique, accuracy, and applications," *Cardiovasc Intervent Radiol,* vol. 35, pp. 986-98, Oct 2012.

[62] F. Banovac, J. Tang, S. Xu, D. Lindisch, H. Y. Chung, E. B. Levy, *et al.*, "Precision targeting of liver lesions using a novel electromagnetic navigation device in physiologic phantom and swine," *Med Phys,* vol. 32, 2005.

[63] H. Zhang, F. Banovac, R. Lin, N. Glossop, B. J. Wood, D. Lindisch, *et al.*, "Electromagnetic tracking for abdominal interventions in computer aided surgery," *Comput Aided Surg,* vol. 11, pp. 127-36, May 2006.

[64] C. W. Fristrup, T. Pless, J. Durup, M. B. Mortensen, H. O. Nielsen, and C. P. Hovendal, "A new method for three-dimensional laparoscopic ultrasound model reconstruction," *Surg Endosc,* vol. 18, pp. 1601-4, Nov 2004.

[65] D. Wilheim, H. Feussner, A. Schneider, and J. Harms, "Electromagnetically navigated laparoscopic ultrasound," *Surg Technol Int,* vol. 11, pp. 50-4, 2003.

[66] F. Liu, P. Liang, X. Yu, T. Lu, Z. Cheng, C. Lei, *et al.*, "A three-dimensional visualisation preoperative treatment planning system in microwave ablation for liver cancer: a preliminary clinical application," *Int J Hyperthermia,* vol. 29, pp. 671-7, Nov 2013.

[67] D. Sindram, K. A. Simo, R. Z. Swan, S. Razzaque, D. J. Niemeyer, R. M. Seshadri, *et al.*, "Laparoscopic microwave ablation of human liver tumours using a novel three-dimensional magnetic guidance system," *HPB (Oxford),* vol. 17, pp. 87-93, Jan 2015.

[68] M. Birth, P. Iblher, P. Hildebrand, J. Nolde, and H. P. Bruch, "Ultrasound-guided interventions using magnetic field navigation. First experiences with ultra-guide 2000 (TM) under operative conditions," *Ultraschall in Der Medizin,* vol. 24, pp. 90-95, Apr 2003.

[69] M. Nagel, M. Hoheisel, R. Petzold, W. A. Kalender, and U. H. W. Krause, "Needle and catheter navigation using electromagnetic tracking for computer-assisted C-arm CT interventions," in *Medical Imaging*, 2007, pp. 65090J-65090J-9.

[70] Z. Yaniv, E. Wilson, D. Lindisch, and K. Cleary, "Electromagnetic tracking in the clinical environment," *Medical Physics,* vol. 36, p. 876, 2009.

[71] E. Wilson, Z. Yaniv, H. Zhang, C. Nafis, E. Shen, G. Shechter, *et al.*, "A hardware and software protocol for the evaluation of electromagnetic tracker accuracy in the clinical environment: a multi-center study," in *Medical Imaging*, 2007, pp. 65092T-65092T-11.

[72] A. D. Wiles, D. G. Thompson, and D. D. Frantz, "Accuracy assessment and interpretation for optical tracking systems," in *Medical Imaging*, 2004, pp. 421-432.

[73] A. M. Franz, M. Servatius, A. Seitel, B. Radeleff, H. U. Kauczor, H. P. Meinzer, *et al.*, "Navigated targeting of liver lesions: pitfalls of electromagnetic tracking," *Biomedical Engineering / Biomedizinische Technik*, vol. 57, 2012.

[74] R. Kashyap, *Fiber Bragg Gratings*: Academic Press, 2010.

[75] K. O. Hill and G. Meltz, "Fiber Bragg grating technology fundamentals and overview," *Journal of Lightwave Technology*, vol. 15, 1997.

[76] E. Al-Fakih, N. A. Abu Osman, and F. R. Mahamd Adikan, "The use of fiber Bragg grating sensors in biomechanics and rehabilitation applications: the state-of-the-art and ongoing research topics," *Sensors (Basel)*, vol. 12, pp. 12890-926, 2012.

[77] F. Taffoni, D. Formica, P. Saccomandi, G. Di Pino, and E. Schena, "Optical fiber-based MR-compatible sensors for medical applications: an overview," *Sensors (Basel)*, vol. 13, pp. 14105-20, 2013.

[78] V. Mishra, N. Singh, U. Tiwari, and P. Kapur, "Fiber grating sensors in medicine: Current and emerging applications," *Sensors and Actuators A: Physical*, vol. 167, pp. 279-290, 2011.

[79] I. Iordachita, Z. Sun, M. Balicki, J. U. Kang, S. J. Phee, J. Handa, *et al.*, "A sub-millimetric, 0.25 mN resolution fully integrated fiber-optic force-sensing tool for retinal microsurgery," *Int J Comput Assist Radiol Surg*, vol. 4, pp. 383-90, Jun 2009.

[80] M. Abayazid, M. Kemp, and S. Misra, "3D flexible needle steering in soft-tissue phantoms using Fiber Bragg Grating sensors," in *Robotics and Automation (ICRA), 2013 IEEE International Conference on*, 2013, pp. 5843-5849.

[81] Y.-L. Park, S. Elayaperumal, B. Daniel, S. C. Ryu, M. Shin, J. Savall, *et al.*, "Real-Time Estimation of 3-D Needle Shape and Deflection for MRI-Guided Interventions," *IEEE/ASME Transactions on Mechatronics*, 2010.

[82] K. Henken, D. Van Gerwen, J. Dankelman, and J. Van Den Dobbelsteen, "Accuracy of needle position measurements using fiber Bragg gratings," *Minim Invasive Ther Allied Technol*, vol. 21, pp. 408-14, Nov 2012.

[83] K. Henken, J. Dankelman, J. Van Den Dobbelsteen, D. Van Gerwen, L. K. Cheng, and H. M. S., "Error Analysis of FBG-Based Shape Sensors for Medical Needle Tracking," *IEEE/ASME Transactions on Mechatronics*, vol. 19, pp. 1523-1531, 2014.

[84] R. Seifabadi, E. E. Gomez, F. Aalamifar, G. Fichtinger, and I. Iordachita, "Real-time tracking of a bevel-tip needle with varying insertion depth: Toward teleoperated MRI-guided needle steering," in *Intelligent Robots and Systems (IROS), 2013 IEEE/RSJ International Conference on*, 2013, pp. 469-476.

[85] J. P. Moore and M. D. Rogge, "Shape sensing using multi-core fiber optic cable and parametric curve solutions," *Opt Express*, vol. 20, pp. 2967-73, Jan 30 2012.

[86] K. K. C. Lee, A. Mariampillai, M. Haque, B. A. Standish, V. X. D. Yang, and P. R. Herman, "Temperature-compensated fiber optic 3D shape sensor using femtosecond laser direct-written Bragg grating waveguides," in *SPIE LASE*, 2014, p. 897210.

[87] C. Ledermann, H. Pauer, O. Weede, and H. Woern, "Simulation tool for 3D shape sensors based on Fiber Bragg gratings and optimization of measurement points," in *Robotics, Automation and Mechatronics (RAM), 2013 6th IEEE Conference on*, 2013, pp. 195-200.

[88] K. K. Mandal, F. Parent, S. Martel, R. Kashyap, and S. Kadoury, "Calibration of a needle tracking device with fiber Bragg grating sensors," in *SPIE Medical Imaging*, 2015, pp. 94150X-94150X-8.

[89] W. E. Lorensen and H. E. Cline, "Marching cubes: A high resolution 3D surface construction algorithm," *ACM SIGGRAPH Computer Graphics*, vol. 21, pp. 163-169, 1987.

[90] *Newport*. Available: https://www.newport.com/images/webDocuments-EN/images/12617.PDF

[91] A. Seginer, "Rigid-body point-based registration: The distribution of the target registration error when the fiducial registration errors are given," *Med Image Anal*, vol. 15, pp. 397-413, Aug 2011.

[92] J. M. Fitzpatrick, M. I. Miga, and K. H. Wong, "Fiducial registration error and target registration error are uncorrelated," in *SPIE Medical Imaging*, 2009, p. 726102.

[93] *Plus (Public software Library for UltraSound imaging research)*. Available: https://www.assembla.com/spaces/plus/wiki